GRAPHENE BASED PLASMONIC INTEGRATED CIRCUITS FOR TERAHERTZ APPLICATIONS

Ph.D. THESIS

by

NEETU JOSHI

DEPARTMENT OF ELECTRONICS & COMMUNICATION ENGINEERING
INDIAN INSTITUTE OF TECHNOLOGY ROORKEE
ROORKEE - 247 667 (INDIA)
OCTOBER, 2018

GRAPHENE BASED PLASMONIC INTEGRATED CIRCUITS FOR TERAHERTZ APPLICATIONS

A THESIS

Submitted in partial fulfilment of the requirements for the award of the degree

of

DOCTOR OF PHILOSOPHY

in

ELECTRONICS & COMMUNICATION

by

NEETU JOSHI

DEPARTMENT OF ELECTRONICS & COMMUNICATION ENGINEERING
INDIAN INSTITUTE OF TECHNOLOGY ROORKEE
ROORKEE - 247 667 (INDIA)
OCTOBER, 2018

INDIAN INSTITUTE OF TECHNOLOGY ROORKEE
ROORKEE

CANDIDATE'S DECLARATION

I hereby certify that the work which is being presented in the thesis entitled **"GRAPHENE BASED PLASMONIC INTEGRATED CIRCUITS FOR TERAHERTZ APPLICATIONS"** in partial fulfilment of the requirement for the award of the Degree of Doctor of Philosophy and submitted in the Department of Electronics and Communication Engineering of the Indian Institute of Technology Roorkee, Roorkee is an authentic record of my own work carried out during a period from July, 2013 to October, 2018 under the supervision of Dr. Nagendra Prasad Pathak, Associate Professor, Department of Electronics and Communication Engineering, Indian Institute of Technology Roorkee, Roorkee, India.

The matter presented in this thesis has not been submitted by me for the award of any other degree of this or any other Institute.

(NEETU JOSHI)

This is to certify that the above statement made by the candidate is correct to the best of my knowledge.

(Nagendra Prasad Pathak)
Supervisor

The Ph.D Viva Voce Exmaination of **Ms. NEETU JOSHI**, Research Scholar, has been held on ……..

Chairperson, SRC **Signature of External Examiner**

This is to certify that the student has made all the corrections in the thesis.

Signature of Supervisor(s) **Head of the Department**

Date:

Abstract

Graphene has enticed a wide number of researchers due to its remarkable optical and electronic properties, which have been exploited rapidly in the field of nano-photonics and plasmonics. It has unique magnetic properties due to its unusual band structure and large number of charge carriers behaving as Dirac Fermions equivalent to 2D gases in metals, leading to Berry's phase and quantum Hall effect in graphene supporting TE, TM and Q-TEM modes. It needs excitation of graphene plasmon polaritons, demanding sophisticated technology and instrumentation. As compared to the plasmon polaritons in inert metals, graphene has many distinguishably valuable features like high field confinement, lower losses and longer propagation lengths. The potential applications of graphene lie in the area of modulators, phase-shifters, surface cloaking, filters, antennas, etc. in the terahertz frequency regime. This thesis mainly focuses on the process of developing graphene plasmonic devices from the concept of nanoscale wireless links, with specific emphasis on synthesizing data from numerical simulation into an accurate, predictive understanding of nanoscale THz (0.1 to 10 THz) phenomena.

The wireless communications demand ultra-high bandwidth at high data rates in the order of Tbps. The optical communications allow transmission of high bandwidths, but wireless communication technology is not advanced enough to provide transmitter and receiver integrated circuits in THz regime. The transmission of data rates upto 100 Gbps has been achieved until now. But, in order to achieve higher data rates with ultrafast communication speeds, we require high-speed communication links. Therefore, we move forward to the graphene based terahertz integrated circuits, which provide high data rates with additional features of compactness, tunability and easy-to-synthesize methods. This will accomplish the need of miniaturized transmitter and receivers working at the nanoscale. It provides single-band or multi-band operations sustaining the increased demand of multiple functions using the same system. Multi-band systems can be implemented by parallel, switchable, or concurrent configurations. The concurrent multiband front end provides different standard compatibility with a single circuitry only; hence reduce the circuit size and the power consumption. An attempt is made to an extent to implement this concept in photonic integrated circuits. Probably due to the fact that most of the photonic integrated circuits are developed by using optical waveguides. These optical waveguides operate in TE or TM modes

and have a limited single mode operational bandwidth. In order to obtain multiband operation, we require large single mode operational bandwidth of the waveguide so that no higher order mode can start propagating in the desired two or more than two frequency bands. This can easily be achieved, if waveguide operates in TEM or Quasi TEM mode. Here, quasi-TEM nature of modes is supported by the graphene based plasmonic waveguides. This waveguide can be modeled with the help of a two-wire transmission line operating in quasi TEM mode.

The graphene plasmonic THz link concept is still in its infancy. The design of individual building blocks is missing in the literature. Small efforts have been made to design these devices; therefore, there is a strong need to address this issue, i.e. design of building blocks for nanoscale wireless links so that the concept can be realized in future. The research work reported in this dissertation deals with the design and analysis of graphene plasmonic waveguide based integrated circuits for future photonic transceiver links. The constituents of this link such as antennas, diplexers, filters, couplers and waveguide sections have been investigated and reported in this dissertation work.

This thesis consists of six chapters.

Chapter 1 deals with the motivation for carrying out this research work along with detailed literature review for identifying research gaps. On the basis of identified research gaps, the research problem to be solved during the course of PhD dissertation has been defined.

Chapter 2 of this thesis is devoted for the electromagnetic analysis of graphene plasmonic waveguide and its variants. The transmission line characteristics such as characteristic impedance, propagation constant, effective dielectric constant, etc. have been obtained using full wave electromagnetic simulation tool CST microwave studio 2012 version. In all simulations, graphene has been modeled using its surface impedance model with the help of Kubo's formula.

Chapter 3 of this dissertation describes the graphene plasmonic waveguide based resonators such as ring resonator, and modified complementary split ring resonators. Further, dual pass band photonic circuits have been designed using band pass filters. The full wave simulations have been carried out using commercial software tool CST microwave studio.

Chapter 4 of this thesis deals with the design and analysis of filter based diplexer and directional coupler. The diplexer design involves two band-pass filters (BPFs) designed using graphene

plasmonic SWR. The incident power is split into two parts with a broadband power splitter. This diplexer can simultaneously act as a wavelength-division-multiplexer/demultiplexer.

Chapter 5 explains the design and analysis of an antenna at terahertz frequencies. The antenna is designed with two graphene plasmonic stepped width resonator (GPSWR) connected with a gap. The simulated return loss and radiation pattern of the antenna is also provided in the chapter.

Finally, the conclusions and future scope for further research work have been presented in Chapter 6 of this dissertation.

Acknowledgment

An African proverb rightly says "If you want to go fast, go alone, but if you want to go far, go together". This thesis is indeed a part of my long journey in obtaining the PhD degree. It is the result of five years of work whereby many people generously contributed to this thesis and supported in one way or the other during this amazing journey. I would like to express my sincere gratitude to all of them. First of all, I would like to thank God for his blessings without which nothing is possible in this material world.

I am deeply indebted to my supervisor Dr. Nagendra Prasad Pathak (Associate Professor, Dept. of ECE, IITR) for his valuable guidance, scholarly inputs and consistent encouragement, which helped a lot in the fulfilment of the research work. His guidance helped me throughout the research work. I could not have imagined having a better advisor and mentor for my Ph.D study. For his easy-going attitude yet thorough professionalism, I thank Dr. Pathak, not only for his supervision and scientific expertise provided during this period, but also for imparting wisdom that has inspired me to be a lifelong learner. I appreciate his many useful comments on this work, but even more so, I appreciate his advice, comments, and willingness to discuss any questions or ideas that I have had. I am also very much thankful to his wife Dr. (Mrs.) Pragati Tiwari for her blessings and support.

Besides my advisor, I would like to thank the rest of my thesis committee: Prof. M. V. Kartikeyan, Dr. S. Manhas, and Dr. G. D. Verma, for their encouragement, insightful comments, and hard questions and continuous support. I am also deeply indebted to Dr. T. Mandal (Assistant Professor, Dept. of Chemistry, IITR) for his advice, fruitful discussions, numerous suggestions, constructive criticism, and constant support throughout the period of my research. I thoroughly enjoyed working under his guidance, as he created a very congenial environment conducive to research.

I take this opportunity to express my profound respect to Prof. D. Ghosh, Head, Department of Electronics and Communication, I.I.T. Roorkee, Roorkee. I am also thankful to all other faculty members of the Department for their keen interest in this work. I am highly obliged and express my sincere thanks to the official & technical staff of the Department of Electronics and Communication Engineering, IIT Roorkee.

I greatly enjoyed working with all my colleagues Mrs. Sneha Latha, Mr. Shivesh Tripathi, Mr. Amarjit Kumar, Mr. T. Kola, Mr. Rahul Jaiswal, Ms. Nidhi Pandit, Mr. Arun Warshney and Mrs. Sushmita Dash and all the PG students who have completed their project work in RFIC Lab, IITR and have contributed for this lab. I thank them all for their full cooperation and ever needed help to carry throughout this work and for being around all the time. I also express my thanks to all the research scholars of the department for their support and understanding.

I have no words to express appreciation to my family without their love, inspiration and support I would not have been able to complete this work. I am grateful for my mother-in-law, my father-in-law, my mother, my father, and all my relatives for their love, support and encouragement. Special thanks to my loving daughters, Aaramya and Shridha. And Gaurav Bhatiwada, my husband, without your love, support and understanding, this work would not be possible. I am so thankful that I have you with me, pushing and encouraging me, when I was ready to give up.

Neetu Joshi

Contents

LIST OF FIGURES

LIST OF TABLES

LIST OF PUBLICATIONS

Publications Related to the Thesis

A part of the studies presented and referred in this thesis has also resulted in the ***following research publications***:

1. **N. Joshi** and N. P. Pathak, "Modeling of graphene coplanar waveguide and its discontinuities for THz integrated circuit applications," *Plasmonics*, vol.12, no. 5, pp 1-10, Nov, 2016.

2. **N. Joshi** and N. P. Pathak, "Tunable wavelength demultiplexer using modified graphene plasmonic split ring resonators for terahertz communication," *Photonics and nanostructures-fundamentals and applications*, vol. 28. pp. 1-5, Feb 2018.

3. **N. Joshi** and N. P. Pathak, "Modeling of graphene plasmonic based suspended nanostrip waveguide for THz integrated circuit applications," *Journal of nanophotonics, SPIE,* **12**(2), 026004 (2018), doi: 10.1117/1.JNP.12.026004.

4. **N. Joshi** and N. P. Pathak, "Modeling of Graphene plasmonic Terahertz devices," *Nanoscale devices: Physics, Modeling and Their application*, CRC Press, T&F Group, 2018.

5. **N. Joshi** and N. P. Pathak, "Modeling and design of graphene-based nano-dipatch antenna," ISSS Journal of Micro and Smart Systems, doi: 10.1007/s41683-018-0027-1, Sept, 2018.

PAPER PRESENTED IN CONFERENCES

1. **N. Joshi** and N. P. Pathak, "Graphene Backed Graphene Plasmonic Coplanar Waveguide (GB- GPCPW) for Terahertz Integrated Circuit Applications ," *Proceedings of Applied Electromagnetics Conference IEEE*, Dec. 2015.

2. **N. Joshi** and N. P. Pathak, "Concurrent dual-band tunable graphene based band-pass filter," *IEEE ICIIS*, Roorkee, India, Dec., 2016.

3. **N. Joshi** and N. P. Pathak, "Modeling and design of graphene based power splitter," *ISSS*, Bangalore, India, July, 2017.

4. **N. Joshi** and N. P. Pathak, "Compact ultra-wide-band graphene based tunable band-pass filter," *Second international conference on Advanced Functional Materials*, Los Angeles, U.S.A. Aug. 4-6, 2017.

5. **N. Joshi** and N. P. Pathak, "Design and characterization of graphene*," Proceedings of 3rd international conference on nanotechnology for better living*, NIT Srinagar, India, May 2016.

Chapter 1

Motivation and Literature Review

1.1 Motivation

The demand for the faster data routing and processing is one of the major challenges, which is quintessential for the existing wireless communication systems. The Silicon electronics industry has made enormous progress and continuously rising towards smaller, faster and more efficient electronic devices over the last many decades. However, scaling of these devices causes many challenges like thermal dissipation and signal delay issues associated with electronic metallic interconnection and thus prevents significant increase in processor speed. Since, from past several decades, copper has been used as an interconnect medium in the integrated circuits. It has been seen that below 100 nm regime, copper interconnection suffers many problems like signal and clock distortion, attenuation, impedance matching, crosstalk, power dissipation, reflection of the waves and limitations of interconnection density [1].

Optical waveguides, on the other hand, shows the capacity of carrying extremely large amount of data and considered as a low power-dissipating medium. Thus, it may offer new solutions for avoiding these problems. These optical alternatives support higher order modes like transverse-electric (TE) or transverse-magnetic (TM) modes, each mode has a cut-off frequency below which no electromagnetic (EM) wave can be transmitted. Since these cut-off frequencies depend upon the physical size of the optical waveguides, hence the dimension of the waveguide cannot be reduced beyond a certain limit. Thus, it also restricts and limits the integration of nano-scale electronic devices with these high speed links. The size difference between electronic devices and photonic components is a major reason that hampers their inter-coupling. Further, reduction of size of optical waveguides are possible if any mode other than these higher order modes TE or TM, can exist and propagate through waveguide below the cut-off frequency. The solution is found in the development of new chip-scale technology, which transmits the information between nano-scale devices at optical frequencies and bridges the gap between the world of nano-scale electronics and micro-scale photonics which is termed as Plasmonics. Plasmonic waveguides can transmit the EM wave even when operating below cut-off conditions of dominant mode [2-3].

Since demand for wireless data rates are increasing exponentially, thus the terahertz (THz) links provide a possibility for realization of THz integrated circuits. At microwave frequency, the available bandwidth for communication systems is limited. Thus, it motivates the exploration of higher frequency bands for communication. In this direction, THz band communication is being explored now-a-days, as it is supposed to satisfy the need for much higher wireless data rates due to large available bandwidth in short distance communication. Despite of absorption from water vapour molecules, the THz band support very large bandwidths upto 10 THz for communication distances below 1 meter [4].

Recently, the use of graphene to develop THz integrated circuits has come into existence. Graphene offers excellent electrical conductivity, which make it very well suited for propagating extremely high frequency electrical signals that is desired to setup THz band wireless links. Graphene intrinsically possess high carrier mobility and saturation speeds, as well as strong carrier density modulation by electric field and therefore, potentially, provides a viable post-silicon solution for high-speed, high-throughput THz and analog circuits and communication systems. Therefore, it has numerous possibilities with its excellent properties being light, flexible, fire-proof as well as extremely good conductor [5-6].

1.1.1 Graphene Plasmonic Waveguides as Interconnect

Interconnects have been a growing challenge from the last few decades. Grain boundary scattering and roughness of surface creates even more challenges to electro-migration. The stasis in the intrinsic delay of interconnects with the intrinsic delay in transistor is the major reason behind the growing gap between interconnect and device performance. Copper was introduced as an interconnect for the first time, by IBM in 1997. Since then copper is used as a dominant material for interconnection in integrated circuits. Copper wires are long lasting relatively cheaper and can be shrunk to smaller size than aluminium. However, copper as an interconnect material cannot meet the requirement of today's fast emerging technology because of some unavoidable limitations [7]. These limitations are high power dissipation in narrower interconnects, limitation in bandwidth, heating of devices particularly in terahertz range. This means one cannot go on reducing size of the copper interconnect to some tens of nm without creating above mentioned problems and meet the expectation of Moore's law. Thus, an alternative is needed to replace

copper. Graphene plasmonics based interconnect is a suitable candidate to provide solution to these problems [8].

Most semiconductor devices cannot work properly in THz range for CMOS technology. Fortunately, graphene has high carrier mobility and saturation speed and can be tuned electrically and thus provides a solution for communication system. Copper interconnect cannot get rid of losses and power leakage so, graphene based plasmonic waveguides with longer mean free path of carriers and significantly shorter guiding wavelength may be the effective solution to efficiently transfer THz signal. In addition to above, graphene monolayer has the electronic tunability of propagation constant, characteristic impedance and phase velocity.

In 2012, graphene nanoribbons with very high current density were produced by researchers [9]. The current density was 1000 times higher than those of copper wire. The whole experiment was done by a 100 nm wide and only a fraction of nanometer high nanoribbons. One more advantage of chemical-vapor-deposition (CVD) graphene nanoribbons is that they can be grown uniformly over large area. Scientists at Korea's Advanced Industrial Science and Technology institute (AIST) have used multilayer graphene intercalated with iron chloride powder [10]. The research results in resistivity are comparable to that of copper interconnects. But then the experiment is repeated multiple times in order to check the reproducibility. The iron chloride molecules were embedded between sheets of graphene to lessen its resistivity. Use of graphene interconnects boosts with the finding of ballistic transport in epitaxially grown graphene nanoribbons. Ribbons of graphene of only 40 nm wide were shown to transport electrons ballistically at room temperature over distances large than 10 micrometer. Ballistic transport is mode of transport of electrons without loss of energy as electrons do not collide with other electrons as well as the material crystal lattice. The predicted conductance values for graphene are very high. So, the graphene based technology has recently emerged out of the shadows to have an impact on the circuit delay and power consumption [11-12].

1.1.2 Graphene based THz band intra-chip communications

Fig. 1.1.2.1 shows the conceptual architecture for the transmission of information from one chip to another chip. The connection between the two chips either can be through wired interconnect or can be transmitted wirelessly [13].

The data and information processing on chip-level decides the speed of data transfer in various wireless communication systems. The standard on-chip communication depends on multi-conductor interconnects which behave as parallel processed interconnect bus lines. These wired connects require a fixed clock frequency. But, in case of global interconnects, the clock frequency is reduced four times, when the size becomes half of the original. These multi-conductor interconnects are not suitable for chip-to-chip communication. Due to large interchip distances, the clock frequencies reduce for the chip-to-chip interconnects as compared to on-chip circuits. The wire separation between large number of parallel wires causes mutual coupling or crosstalk between interconnects [14]. These high clock frequencies and the large information rates of chip-to-chip communication provide added interests towards the THz technology.

The wireless THz communication acts as an alternative in order to provide short-distance communication at high speeds. Therefore, high efficiency chip-to-chip communication can be made possible by replacement of multi-conductor interconnects with wireless THz graphene plasmonic multi-antenna interconnects [15-16].

The dispersion gets lower as the signal propagates along the interconnect length. The ultra-high bandwidth at very short distances with the propagating characteristic provide high-performance channel for chip-to-chip communications. The use of graphene plasmonic nano-antennas at the transmitter side as well as the receiver side results in high data rates with the reliability of THz graphene plasmonic systems at the cost of certain computational complexity. Thus wireless chip-to-chip and intra-chip communication through graphene plasmonic nano-antenna at THz frequency has the potential to overcome the limitation of ultra-wideband signal transmission within a monolithic microwave integrated circuit (MMIC) or among MMIC’s [17-18].

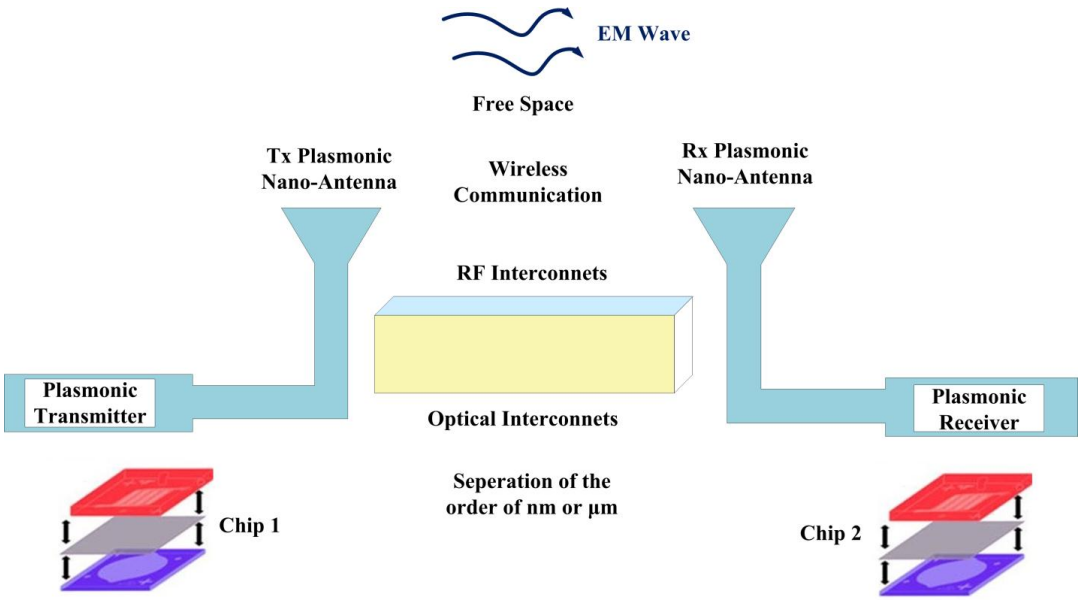

Fig.1.1.2.1 Conceptual chip-to-chip transmission and reception architecture.

1.1.3 Graphene based transmission lines

Araneo et. al. have studied the propagation and attenuation characteristics of graphene nanostrip lines with the help of Method-of-Moments approach [19]. It shows that above 100 GHz, graphene nanostrip lines suffer lower losses as compared to metallic lines enabling its use in THz interconnects and integrated circuits. Graphene-based-conductor transmission lines have also been designed and experimentally studied on conformal surfaces [20]. Their wave propagation characteristics have been found to be similar with copper transmission lines over the frequency range 100 kHz to 8.5 GHz. Coplanar waveguides on graphene have been fabricated and showed that it can be used for designing tunable matching circuits using graphene with 50 Ω impedance and moderate losses in the frequency range 40 MHz to 110 GHz [21-22]. The graphene plasmonic waveguide fabricated prototypes also support TM modes with extinction ratio of 19 dB in optical frequencies [23]. Various transmission lines based on graphene like microstrip, double-side parallel stripline, and uniplanar coplanar waveguide have been designed and analyzed with lossy transmission model [24]. Negligible efforts have been attempted to use the designed structures in THz interconnects and integrated circuits [25]. So, the thesis is aimed towards the need and scope of graphene in THz integrated circuits.

1.2 Characteristics of Graphene plasmonic parallel plate waveguide and its variants

The collective oscillations of non-bound, vacant electrons in conducting metals in combination with the electromagnetic surface waves in dielectric gives rise to the surface plasmon polaritons. The graphene-based plasmonic waveguides with their variants like nanostrip guide, and plasmonic coplanar and conductor-backed coplanar waveguide, have been studied in the next chapter. In the subsequent sections, these graphene waveguides have been presented with their field plots and configurations.

1.2.1 Graphene plasmonic nanostrip waveguide (GPNSW)

The structure of graphene plasmonic nanostrip waveguide is shown in Fig. 1.2.1.1. The quasi-TEM mode propagates as shown in Fig. (1.2.1.2-3). The graphene nanostrip with width, w and thickness, t lies over the dielectric substrate comprising of silica over silicon layer just above the ground plane. Equivalent circuit representation requires knowledge of propagation constant, γ ($\gamma=\alpha+j\beta$) and the characteristic impedance, Z_0 of the nanostrip waveguide geometry. The transmission line equivalent circuit has been obtained using full wave e. m. solver CST Microwave studio (Appendix).

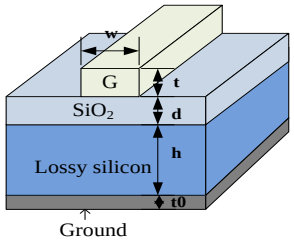

Fig. 1.2.1.1 Structure of GPNSW.

(i)

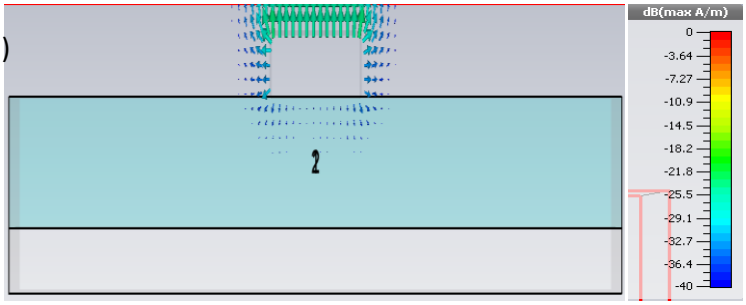

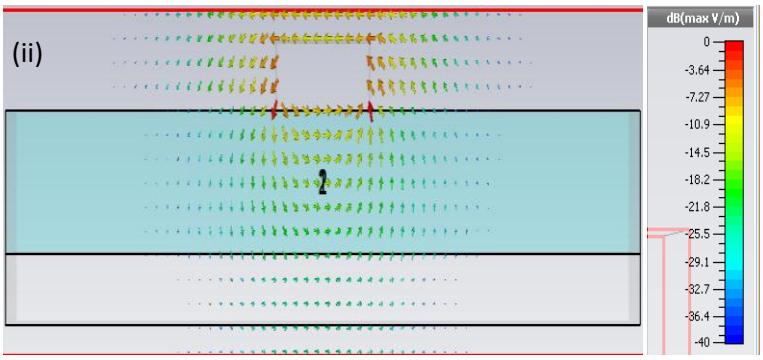

Fig. 1.2.1.2 (i) E-field pattern and (ii) H-field pattern of GPNSW.

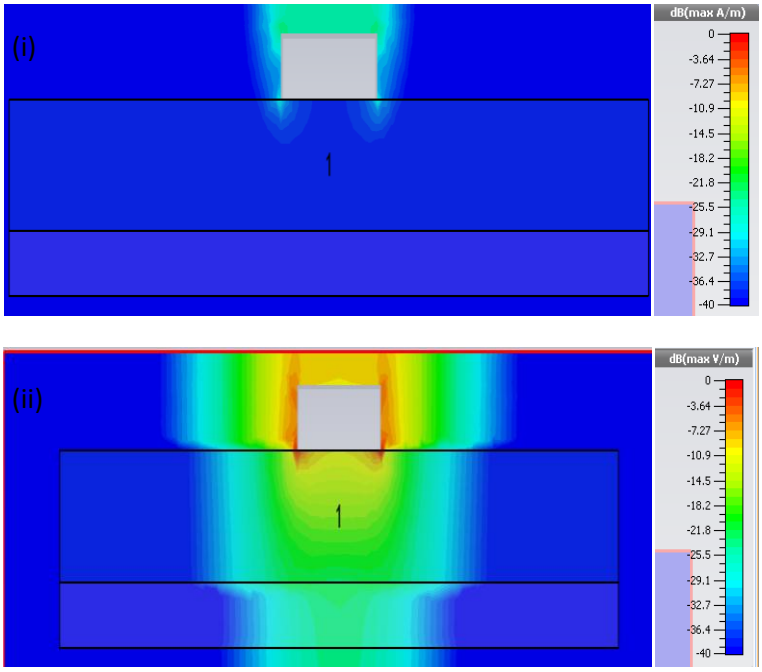

Fig. 1.2.1.3 (i) Abs-E-Field pattern (ii) Abs-H-field pattern of GPNSW.

1.2.2 Graphene plasmonic coplanar waveguide (GPCPW)

Both graphene plasmonics nanostrip waveguide and graphene plasmonics suspended nanostrip waveguide have their guiding strip and ground plane on the opposite side of the substrate. Graphene plasmonic coplanar waveguide shown in Fig. 1.2.2.1 represents another variant of GPPW in which guiding strip and ground plane are present on the same side of the substrate; hence it is uniplanar waveguide structure. This plasmonic waveguide supports two modes viz. even mode and odd mode. Even mode has characteristics similar to quasi TEM mode and it is desired. Odd mode is undesired and it can be suppressed by properly selecting waveguide geometry. Their mode patterns have been shown in Fig. 1.2.2.2-5.

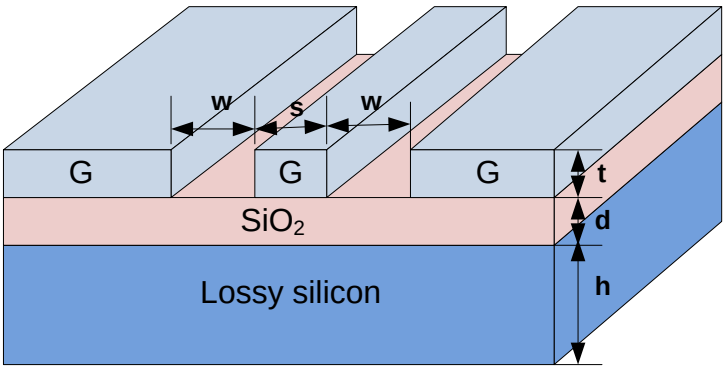

Fig. 1.2.2.1 Structure of GPCPW.

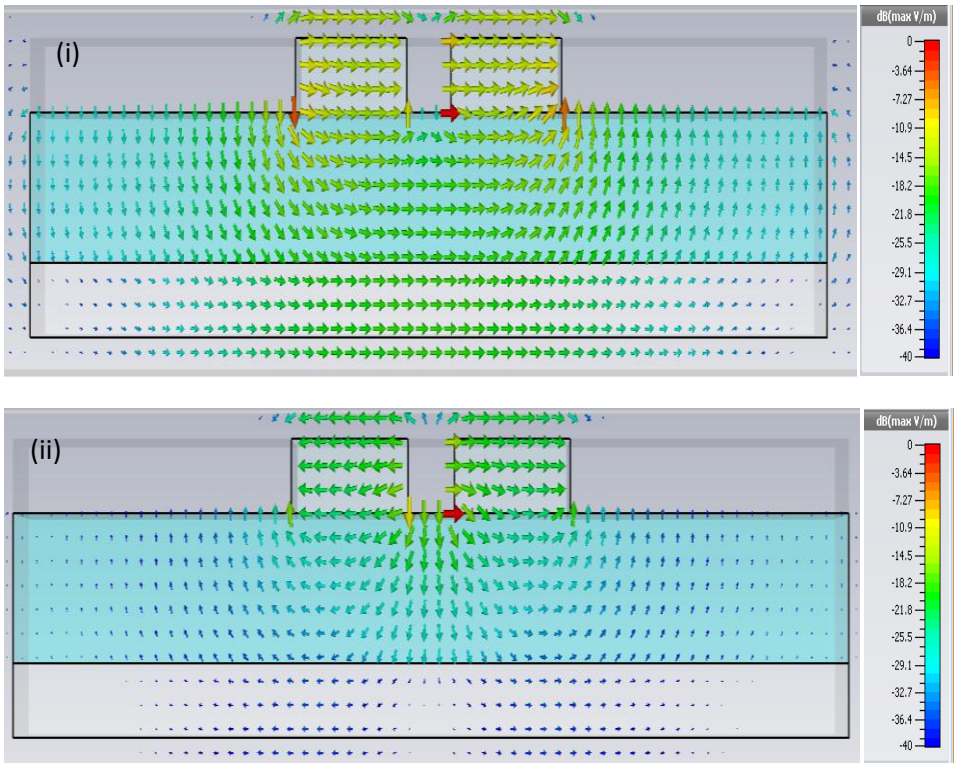

Fig. 1.2.2.2 E-field pattern of (i) mode 1 (ii) mode 2 of Graphene coplanar waveguide.

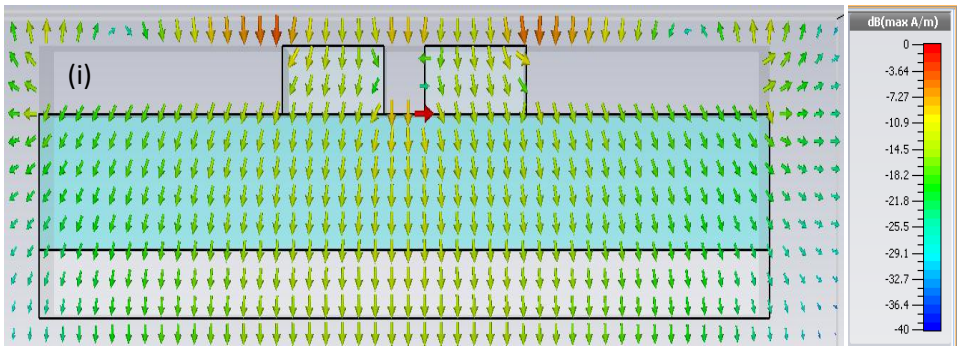

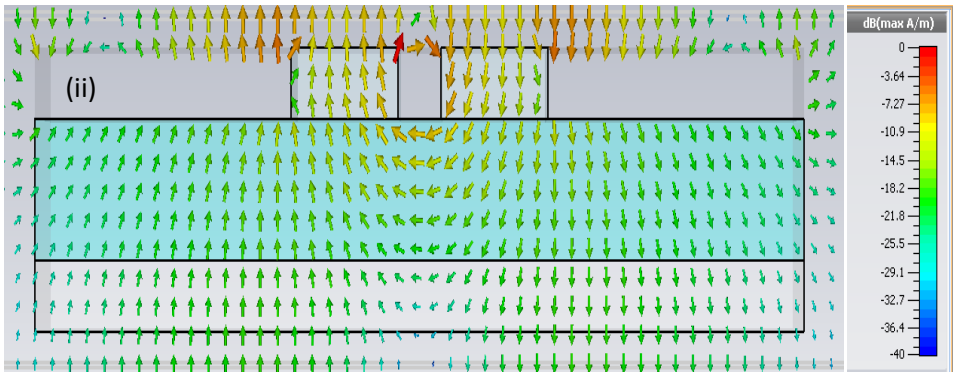

Fig. 1.2.2.3 H-field pattern of (i) mode 1 and (ii) mode 2 of Graphene coplanar waveguide.

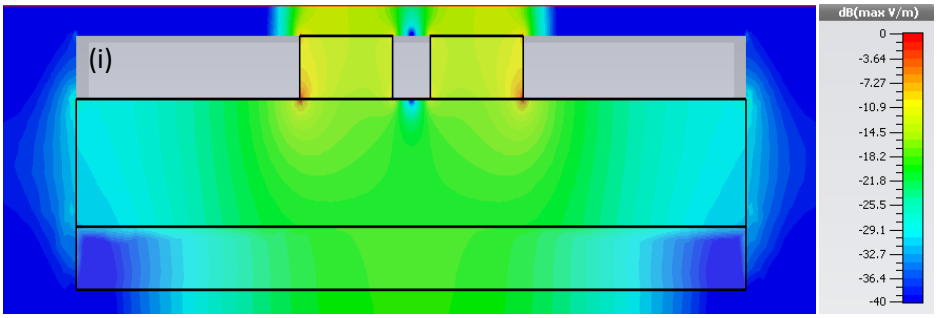

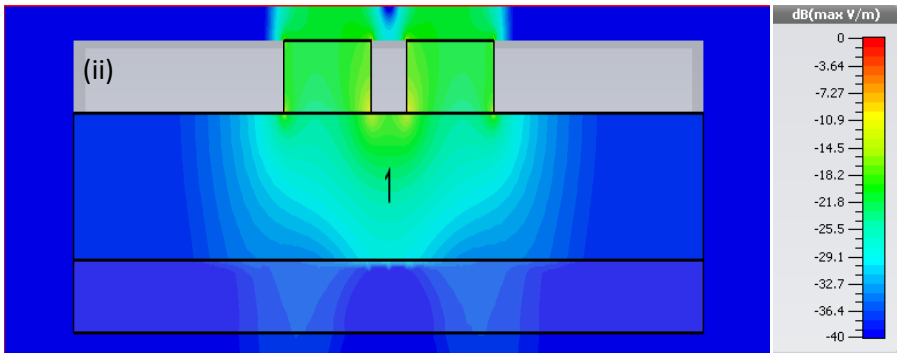

Fig. 1.2.2.4 Abs-E-field pattern of (i) mode 1 (ii) mode 2 of Graphene coplanar waveguide.

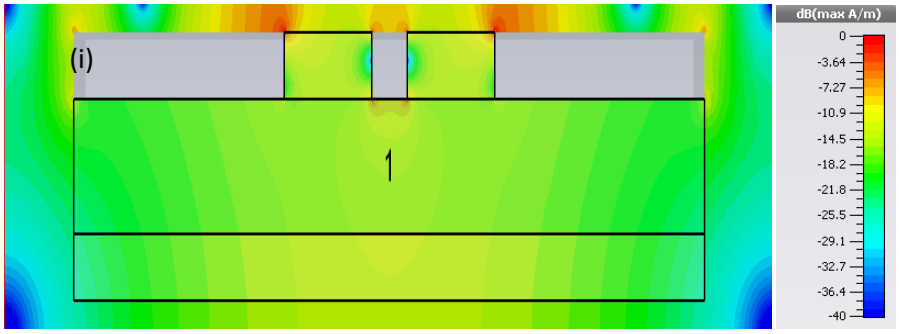

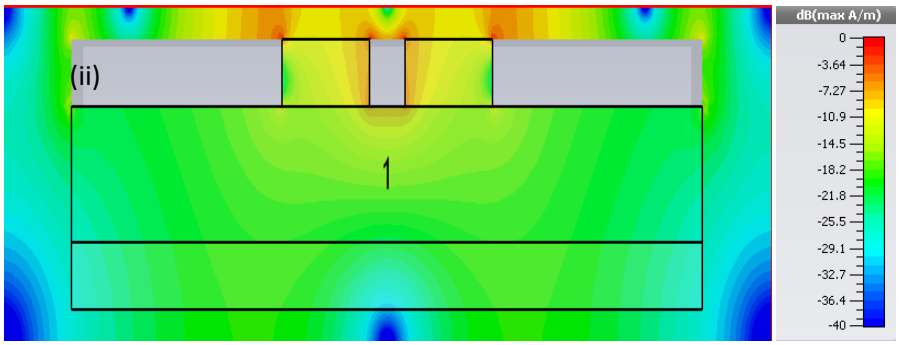

Fig. 1.2.2.5 Abs-H-field pattern of (i) mode 1 and (ii) mode 2 of Graphene coplanar waveguide.

1.3 Review of Graphene Plasmonic Waveguide Based THz Integrated Circuits

Several researchers have investigated the characteristics of Graphene parallel plate waveguides (GPPWs) in the last few years [26-30]. Hanson has predicted that GPPW also supports propagation of quasi-TEM mode [31]. As the graphene layer has a complex surface conductivity dependent on the chemical potential; it may be tuned with the help of the doping concentration or by externally applied electric or magnetic field via Hall effects, which can provide the isotropic and anisotropic values of the conductivity. The semi-classical model and relaxation time approximation (RTA) formulation of conductivity describes the effect of spatial dispersion in decreasing the confinement and losses of slow surface plasmons in the parallel plate waveguides [32]. To increase the confinement, a dielectric layer has been inserted between the anisotropic graphene plates and the value of static electric field is increased by enhancing the graphene conductivity [29]. Recent developments show that the characteristics of terahertz surface plasmons like propagation length and localization length can be improved by the use of Kerr type non-linear media [27] and one dimensional photonic crystal [30]. These waveguide geometries can be fabricated using exfoliation, spin-coating, and CVD process [33]. Various communication technologies have been compared in Table 1.3.1.

Table 1.3.1. Comparison of various communication technologies.

Medium	Z (Ω)	Thickness of dielectric	Frequency	α (/m)	β (/m)	References
RG58/U Coaxial Cable	54	mm	< 1kHz	1	--	[34]
CAT-5 Twisted pair (solid)	100	mm	<1 kHz	--	--	[34]
Vacuum	377	mm	<1 kHz	--	--	[34]

Photonic crystal waveguide	526 Ω	µm	GHz and THz	1.011	--	[35]
MSM (Metal-semiconductor-metal) waveguide	50	µm	Hundreds of THz	0.598	42.88	[36]
Gold-air-gold waveguide	kΩ	µm	1 THz	0.0341	1.0405	[37]
			10 THz	0.0066	1.0226	
Graphene plasmonic waveguide	kΩ	nm	1 THz	0.377	25	[38]
			10 THz	0.395	275	

1.3.1 Graphene parallel plate waveguide (GPPW): Graphene based parallel plate waveguides have been designed using dielectric substrate sandwiched between the two layers of graphene [Fig. 1.3.1.1 (b)]. It propagates a quasi-TEM mode [39], as shown in Fig. 1.4.1.1 (a), and can be used for several applications [40-42].

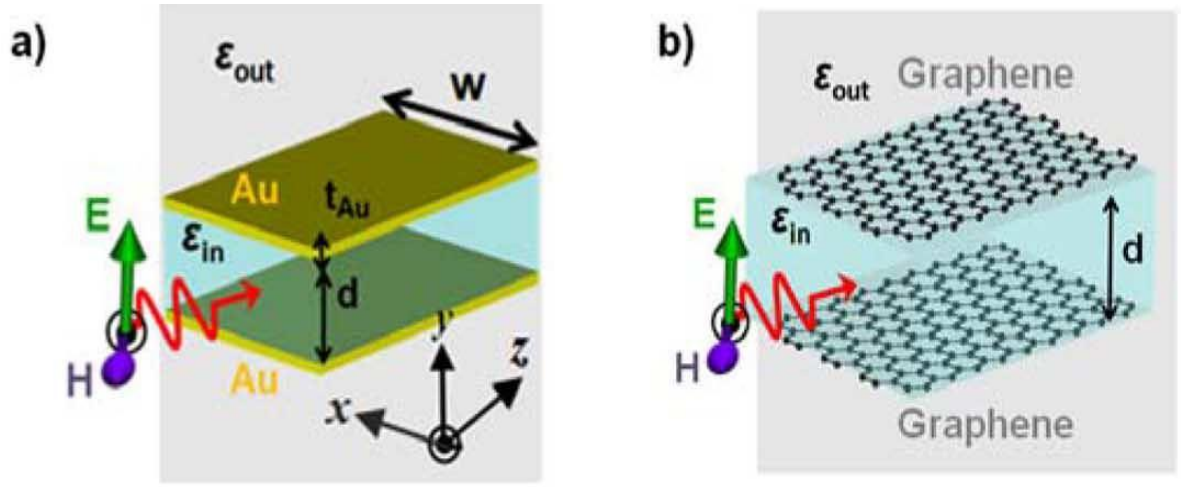

Fig. 1.3.1.1 Schematic diagram of (a) a plasmonic PPWG consisting of a MIM heterostructure (gold-air-gold) and (b) a GPPW [39].

Modal properties of Graphene plasmonic parallel plate waveguide:

The geometry of graphene based plasmonic parallel plate waveguide has been shown in Fig. 1.3.1.1 (a). It consists of a dielectric material layer sandwiched between two large graphene layers. This guiding structure supports TM, TE and quasi-TEM modes. Applying boundary conditions for tangential components of electric and magnetic fields, we can write:

$$\left.\begin{aligned}(E_1 - E_2)\times n_{1-2} &= 0\\ (H_1 - H_2)\times n_{1-2} &= \frac{4\pi}{c}\sigma(\omega,\mu,\gamma,T)E_{\|}\end{aligned}\right\} \qquad \ldots\ldots(1.3.1.1)$$

where n_{1-2} is the unit vector along the normal oriented from region 1 to region 2 and $E_{\|}$ is the electric field of the wave in the xz plane, which induces current in the graphene layers. We obtain the equations for TM polarized waves as

$$\begin{bmatrix} 1 & -1 & -e^{q'd'} & 0 \\ i\frac{4\pi}{c}\frac{q}{k_0}\sigma+1 & -\varepsilon\frac{q}{q'} & \varepsilon\frac{q}{q'}e^{q'd} & 0 \\ 0 & \varepsilon\frac{q}{q'}e^{q'd} & -\varepsilon\frac{q}{q'} & i\frac{4\pi}{c}\frac{q}{k_0}\sigma+1 \\ 0 & -e^{q'd'} & -1 & 1 \end{bmatrix} \times \begin{bmatrix} E_1 \\ E_2^+ \\ E_2^- \\ E_3 \end{bmatrix} = 0 \qquad \ldots\ldots(1.3.1.2)$$

and TE polarized waves as

$$\begin{pmatrix} 1 & -\varepsilon\frac{q}{q'} & \varepsilon\frac{q}{q'}e^{q'd} & 0 \\ i\frac{4\pi}{c}\frac{k_0}{q}\sigma-1 & 1 & e^{q'd} & 0 \\ 0 & e^{q'd} & 1 & i\frac{4\pi}{c}\frac{k_0}{q}\sigma-1 \\ 0 & \varepsilon\frac{q}{q'}e^{q'd} & -\varepsilon\frac{q}{q'} & 1 \end{pmatrix} \times \begin{pmatrix} H_1 \\ H_2^+ \\ H_2^- \\ H_3 \end{pmatrix} = 0 \qquad \ldots..(1.3.1.3)$$

Setting the determinants of the matrices to zero, we obtain the dispersion relations as

$$\begin{cases} 1+i\frac{4\pi}{c}\frac{q}{k_0}\sigma(\omega) = -\varepsilon\frac{q}{q'}\frac{e^{q'd}+1}{e^{q'd}-1} \\ 1+i\frac{4\pi}{c}\frac{q}{k_0}\sigma(\omega) = -\varepsilon\frac{q}{q'}\frac{e^{q'd}-1}{e^{q'd}+1} \end{cases}$$ For TM_1 and TM_2

$\ldots.(1.3.1.4)$

$$\begin{cases} i\frac{4\pi}{c}\frac{k_0}{q}\sigma(\omega)-1 = \frac{q'}{q}\frac{e^{q'd}-1}{e^{q'd}+1} \\ i\frac{4\pi}{c}\frac{k_0}{q}\sigma(\omega)-1 = \frac{q'}{q}\frac{e^{q'd}+1}{e^{q'd}-1} \end{cases}$$ For TE_1 and TE_2

$\ldots.(1.3.1.5)$

Here, $k_0 = \omega/c$, c is the speed of light, $q = \sqrt{(\beta^2 - k_0^2)}$, $q' = \sqrt{(\beta^2 - \varepsilon_{k0}^2)}$, and $\beta = k_z$ is the magnitude of the wavevector component along the propagation direction. The propagating modes in graphene SPPs are even and odd modes. The TM mode has an evanescent decay in the case of metals with hyperbolic sine and cosine fields. The even mode provides low-loss THz propagation, so the preferred mode. The quasi-TEM mode can be evaluated by assuming that the graphene PPW is having slight perturbations from the perfect PPW.

1.3.2 Graphene plasmonic resonators, filters and sensors

Graphene based active devices have been studied [43-45]. Wang et. al. proposed surface plasmon polaritons (SPPs) based refractive index sensor consisting of two metal-insulator-metal (MIM) waveguides coupled to each other by a ring resonator [46]. The analysis of transmission characteristics has been performed to analyze the sensing characteristics. The tuning range of SRR can be increased by optimizing the SRR modal characteristics [47]. A nano-optomechanical system based on a doubly-clamped Z-shaped graphene nanoribbon (GNR) with an optical pump-probe scheme has been presented with the demonstration of the phonon-induced transparency by Chen et. al. [48]. The graphene based SRRs have been studied [49-50], which can be used for sensing [51] and hybrid tunable metamaterials [52], etc. SRRs sustain the resonance peaks at nanometer scale wavelengths lesser than their physical dimensions. They show the capability of concentrating the electric field in smaller volumes and their further enhancement. Multiple resonances allow designing the desired frequencies of operation and responses of SRRs for the purpose of localization and enhancement of incident electromagnetic field. A variety of graphene-based devices like tunable filter [53], low-pass filters [54] and band-pass filters [55] have been studied till date. Also, the graphene based plasmonic resonators have been studied, which provide lower attenuation values (0.3 dB) as compared to metallic resonators (0.43-0.6 dB) [56].

1.3.3 Graphene based demultiplexer and coupler

The plasmonic demultiplexers for SPPs have been demonstrated for realization of light to show coupling, dispersion and guiding characteristics of SPPs, which can be used for demultiplexing and filtering operations [57]. WDM using MIM plasmonic nanodisk resonators have been proposed and simulated with the help of FDTD based electromagnetic simulations [58]. Coupled-mode theory has been studied in plasmonic waveguides [59]. The unique properties of optical

waveguides electrically controlled by means of graphene layers are investigated [60]. Non-linear graphene based couplers have been studied between two closely spaced graphene layers [61].The tuning of SPPs in graphene directional couplers for switching has been studied [62]. The double-layer graphene sheets and three-layer graphene sheets based coupler has been designed [63]. An asymmetric directional coupler has been designed using silicon waveguide (SW) and a graphene multilayer embedded silicon waveguide (GMESW) [64]. Graphene based tunable plasmonic directional coupler has also been studied in the THz frequency regime [65]. Coupled-mode theory (CMT) has been used to analyze the coupling between three graphene sheets with curved configuration [66]. A compact directional coupler with high-index dielectric ridges for planar integration has been studied [67]. THz wireless communications can be used for transmitting high data rates [68-69].

1.3.4 Graphene based antenna

Graphene, being an epsilon-near-zero (ENZ) material, can be used as a multiple beam splitter due to its tunability with applied electric bias or chemical doping [70]. Moreover, the beam valley splitting has been controlled in graphene by gating and strain [71]. Also, the plasmonic splitter has been designed using dielectric loaded graphene plasmonic waveguide [72]. Recently, the graphene based tunable power splitters have been proposed [73-75]. The nano-patch antenna [76-79] arrays can be designed with the help of the power-splitter. The graphene based nano-patch antenna provide a promising performance with finite conductivity, slower propagation of current waves, smaller size and excellent radiation characteristics as compared to its metallic counterparts [80].

1.4. Research gaps and Problem definition

There is a continually increasing demand of higher data rates and enhanced bandwidths for communication, which can be achieved by increasing the carrier frequencies up to sub-THz and THz frequency regimes. Graphene plasmonic THz link is an alternative to fulfill the demand. But the concept is still in its infancy. The communication links have been explored in the region of microwave and X-ray frequencies but it has been lesser explored in the THz range. Most of the equipments used in THz research are large and heavy, and require special operating conditions such as controlled temperature and humidity and use of liquefied gases which make it hard to implement in real-life applications. The plasmonic designs in THz frequency range using inert metals like MIM and IMI waveguides developed earlier are limited, lacking higher confinement

and tunability features. Graphene based plasmonic structures provide advantages in design performance, flexibility, fabrication, integration and tunability as compared to existing structures. The design of individual building blocks for graphene plasmonic THz link is missing in the literature. Small efforts have been made to design these devices; therefore, there is a strong need to address this issue, i.e. design of building blocks for nanoscale wireless links so that the concept can be realized in future. The research work reported in this dissertation deals with the design and analysis of graphene plasmonic waveguide based integrated circuits for future photonic transceiver links. Some of the constituents of this link such as antennas, diplexers, filters, couplers and waveguide sections have been investigated and reported in this dissertation work. The simulation results have been validated against results of similar components from the literature.

Concept of hybrid integrated THz circuits : We propose to develop graphene based THz integrated circuits, suitable for integration with 3D dielectric waveguide technology such as NRD guide as shown in Fig. 1.4.1. The NRD guide operates in LSM11 mode, while dominant mode of graphene plasmonic nanostrip waveguide is similar to quasi TEM mode. In the proposed scheme, GPNSW is mounted over the top plate of NRD guide; making upper ground plane of NRD guide and GPNSW common. A rectangular slot etched in the common ground plane of GPNSW and NRD guide will allow the magnetic field lines of NRD guide to excite the relevant mode of GPNSW. The similar scheme is available at millimeter wave frequencies as well. The difficulties associated with planar transmission lines are now overcomed by the use of GPNSW; hence the concept can be used even at THz frequencies.

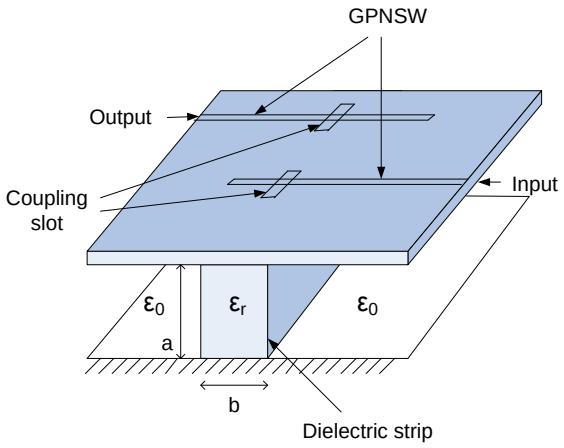

Fig. 1.4.1 NRD waveguide coupled with GPNSW.

1.5 Organization of thesis:

This PhD thesis describes design and full wave analysis of terahertz integrated circuits using graphene plasmonic waveguides. First, we consider the material properties of graphene at optical and THz frequencies and later the propagation of electromagnetic waves through graphene plasmonic waveguide structures have been considered. Detailed modelling of graphene plasmonic parallel plate waveguide and it's variants such as nano strip, suspended nano strip, coplanar and graphene backed coplanar waveguides have been carried out to determine phase constant, attenuation constant, characteristic impedance and propagation length of the guiding media. The modelling of physical discontinuities and their lumped element electrical equivalents have also been described so that it can be used in the design of integrated circuits at THz frequencies. Some design examples of graphene plasmonics based THz integrated circuits such as resonator, band pass filter, power splitter; coupler and antenna have also been provided. The entire research work has been divided into six chapters. The details of individual chapters have been given below:

Chapter 1 of the thesis provides brief review of the existing technology, which can be used for THz wireless links along with the motivation for the incorporation of the concept of graphene plasmonics in THz frequency applications. A detailed literature review has been given to emphasize the research gap and providing problem definition along with the thesis composition.

Chapter 2 describes full wave simulation and modelling of graphene plasmonic waveguide to obtain it's characteristics such as normalized propagation constant, characteristic impedance and propagation length. Full wave simulation software (CST-Microwave Studio) has been used in this study which is used to analyze the characteristics of variants of graphene plasmonic parallel plate waveguide such as graphene plasmonic nanostrip waveguide, graphene plasmonic suspended nanostrip waveguide, graphene plasmonic coplanar waveguide, graphene plasmonic graphene backed coplanar waveguide. Also, the graphene plasmonic waveguide based discontinuities such as open-end, step and short discontinuities have been studied.

Chapter 3 describes design and analysis of graphene plasmonic waveguide based resonators and filters to obtain single-band and dual-band frequency response alongwith low-insertion loss and tunability. Tunning has been achieved with the help of change in chemical potential of graphene.

Chapter 4 describes the design of graphene plasmonic wavelength-division-demultiplexer (WDM), diplexer and directional coupler for THz communications. The graphene based WDM has been designed with the help of a split-ring resonator which works on the principle of change in resonance peaks of the transmission spectrum with the material dielectric constant. The diplexer design involves two band pass filters (BPF) and a broadband power splitter. This diplexer can work as multiplexer/demultiplexer. The design of the graphene based directional coupler has also been studied.

Chapter 5 presents the design and analysis of a graphene based patch antenna at THz frequencies. Based on the patch antenna, a di-patch antenna has also been analyzed. The concept can be extended to design several other components such as series and parallel multi-patch antennas. These graphene-based nanoantennas radiate electromagnetic waves in the terahertz frequency band. These results will enable and promote ongoing research in the realm of nanoscale terahertz wireless communications.

Chapter 6 of this dissertation has been devoted to describe the conclusions and scope for further research work using graphene based THz integrated circuits.

1.6 CONCLUSIONS

This chapter describes the motivation to initiate the present thesis work along with the literature review and problem definition. The present work is motivated from the fact that there is negligible reported effort to implement the concept of nanoscale wireless link using graphene plasmonic integrated circuits in the THz regime. The detailed information regarding the design of individual building block of wireless links is followed in subsequent chapters.

REFERENCES:

[1] D. A. B. Miller, "Physical reasons for optical interconnections", *Int. J. Optoelectron.*, vol. 11, pp. 155-168, 1997.

[2] W. L. Barnes, A. Dereux, and T. W. Ebbesen, "Surface plasmon subwavelength optics," *Nat. Photonics,* vol. 424, no.14, pp. 824-830, Aug. 2003.

[3] D. K. Gramotnev and S. I. Bozhevolnyi, "Plasmonics beyond the diffraction limit", *Nat. Photonics*, pp. 83-91, Jan. 2010.

[4] J. F. Federici and L. Moeller, "Review of terahertz and subterahertz wireless communications," *J. Appl. Phys.,* vol. 107, no. 11, pp. 111101 1-22, July 2010.

[5] T. Low and P. Avouris, "Graphene plasmonics for terahertz to mid-infrared applications," *ACS*, vol. 8, no. 2, pp. 1086-1101, Jan. 2014.

[6] J. S. Gómez-Díaz and J. Perruisseau-Carrier, "Microwave to THz properties of graphene and potential antenna applications," *Proceedings of ISAP2012*, pp. 239-242, 2012.

[7] J. A. Conway, S. Sahni, and T. Szkopek, "Plasmonic interconnects versus conventional interconnects: a comparison of latency, crosstalk and energy costs", *Opt. Express*, vol. 15, no. 8, pp. 4474-84, Apr. 2007.

[8] A. Naeemi and J. D. Meindl, "Performance benchmarking for graphene nano-ribbon, carbon-nanotube and copper interconnects", *International interconnect technology conference*, June 2008.

[9] A. Behnam, A. S. Lynos, M. H. Bae, E. K. Chow, S. Islam, C. M. Neumann and E. Pop, "Transport in Nanoribbon interconnects obtained from graphene grown by chemical vapour deposition", *Nano Lett.*, vol. 12, pp. 4424-4430, Aug. 2012.

[10] "Development of technology for producing micro-scale inter-connect from multi-layer graphene", *AIST*, Sept. 2013.

[11] S. Rakheja, V. Kumar and A. Naeemi, "Evaluation of the potential performance of graphene nano-ribbons as on-chip interconnects", *Proceedings of IEEE*, vol. 101, no.7, pp. 1740-1765, July 2013.

[12] S. Bhattacharya, S. Das, D. Das and H. Rahaman, "Electrical transport in graphene nano-ribbon interconnect", *International conference on Devices, circuits and systems*, Oct. 2014.

[13] H. Yordanov and P. Russer, "Wireless inter-chip and intra-chip communication," *Proceedings of the 39th European Microwave Conference*, Italy, 2009.

[14] V. Petrov, D. Moltchanov, M. Komar, A. Antonov, P. Kustarev, S. Rakheja, and Y. Koucheryavy, "Terahertz Band Intra-Chip Communications: Can Wireless Links Scale Modern x86 CPUs?" *IEEE Access*, vol. 5, pp. 6095-6109, 2017.

[15] J. M. Jornet and I. F. Akyildiz, "Graphene-based Plasmonic Nano-transceiver for Terahertz Band Communication" *Proceeding of the 8th European Conference on Antennas and Propagation (EuCAP)*, 2014.

[16] P. Y. Chen, A.Alù, "All-Graphene terahertz analog nanodevices and nanocircuits," *Proceeding of the 7th European Conference on Antennas and Propagation (EuCAP)*, 2013.

[17] B. Yu, Y. Ye, X. L. Liu, Q. J. Gu, "Sub-THz Interconnect Channel for Planar Chip-to-Chip Communication," *Proceedings of the IEEE Conference*, 2016.

[18] N. Aflakian, T. LaFave, R. M. Henderson, K. K. O, and D. L. MacFarlane, "Square dielectric interconnect for chip-to-chip THz communication," *Proceedings of the IEEE Conference*, 2017.

[19] R. Araneo, G. Lovat and P. Burghignoli, "Graphene nanostrip lines: Dispersion and attenuation analysis", *IEEE 16th workshop on Signal and Power integrity*, May 2012.

[20] S. M. Asif, A. Iftikhar, B. D. Braaten and M. S. Khan, "Wave propagation and coupling of graphene based conductor transmission lines on a conformal surface-An Experimental Study", *IEEE International Symposium on Antennas and Propagation*, July 2016.

[21] M. Dragoman, D. Neculoiu, A. Cismaru, A. A. Muller, G. Deligeorgis, G. Konstantinidis, D. Dragoman and R. Plana, "Coplanar waveguide on graphene in the range 40 MHz-110 GHz", *Appl. Phys. Lett.*, vol. 99, no. 3, July 2011.

[22] J. S. Gomez-Diaz and J. Perruisseau-Carrier, "A transmission line model for plasmon propagation on a graphene strip", *IEEE MTTS International Microwave Symposium*, pp. 1-3, June 2013.

[23] J. T. Kim and S. Y. Choi, "Graphene based plasmonic waveguides for photonic integrated circuits", *Opt. Exp.*, vol. 19, no. 24, pp. 24557-24562, Nov. 2011.

[24] Y. Wu, M. Qu and Y. Liu, "A generalized transmission line model for tunable graphene-based transmission lines with attenuation phenomenon", *Nature*, vol. 6, Aug. 2016.

[25] A. S. Sadeghi, G. Moradi, R. S. Shirazi and A. Bagheri, "Analysis of graphene based transmission line in the THz band", *Optik*, 157, pp. 606-611, Oct. 2017.

[26] D. Svintsov, V. Vyurkov, V. Ryzhii and T. Otsuji, "Voltage-controlled surface plasmon-polaritons in double graphene layer structures," *J. Appl. Phys.*, vol. 113, no. 4, pp. 053701 1-5, Feb. 2013.

[27] H. Hajian, A. Soltani-Vala, M. Kalafi and P. T. Leung, "Surface plasmons of a graphene parallel plate waveguide bounded by Kerr-type nonlinear media," *J. Appl. Phys.*, vol. 115, pp. 083104 1-7, Feb. 2014.

[28] D. Correas-Serrano, J. S. Gomez-Diaz, J. Perruisseau-Carrier and A. Álvarez-Melcón, "Spatially dispersive graphene single and parallel plate waveguides: Analysis and circuit model," *IEEE Trans. Microw. Theory Tech.*, vol. 61, no. 12, pp. 4333–4344, Dec. 2013.

[29] A. Malekabadi, S. A. Charlebois and D. Deslandes, "Parallel plate waveguide with anisotropic graphene plates: Effect of electric and magnetic biases," *J. Appl. Phys.*, vol. 113, pp. 113708 1-9, March 2013.

[30] H. Hajian, A. Soltani-Vala and M. Kalafi, "Optimizing terahertz surface plasmons of a monolayer graphene and a graphene parallel plate waveguide using one-dimensional photonic crystal," *J. Appl. Phys.*, vol. 114, no. 2013, pp. 0331021-8, July 2013.

[31] G. W. Hanson, "Quasi-transverse electromagnetic modes supported by a graphene parallel-plate waveguide," *J. Appl. Phys.*, vol. 104, pp. 1–5, Oct. 2008.

[32] J. S. Gomez-Diaz, J. R. Mosig and J. Perruisseau-Carrier, "Effect of Spatial Dispersion on Surface Waves Propagating Along Graphene Sheets," *IEEE trans. Antennas Propag.*, vol. 61, no. 7, pp. 3589-3596, July 2013.

[33] E. Kymakis, E. Stratakis, M. M. Stylianakis, E. Koudoumas and C. Fotakis, "Spin coated graphene films as the transparent electrode in organic photovoltaic devices," *Thin solid films*, vol. 520, pp. 1238-1241, 2011.

[34] D. M. Pozar, *Microwave Engineering*. Wiley Series, 2012.

[35] Y. Kokubo, "Analysis of propagation loss of metallic photonic crystal waveguides", *Microw. Opt. Technol. Lett.*, vol. 50, no. 11, Nov. 2008.

[36] S. A. Maier, "Plasmonics: Fundamentals and applications," *Springer*, 2006.

[37] B. G. Ghamsari and A. H. Majedi, "Terahertz transmission lines based on surface waves in plasmonic waveguides", *J. Appl. Phys.*, 104, May 2008.

[38] N. Joshi and N. P. Pathak, "Graphene backed graphene plasmonic coplanar waveguide (GB-GCPW) for terahertz integrated circuit applications," *Proceedings of Applied Electromagnetics Conference*, vol. 103, pp. 1-2, Dec. 2015.

[39] P. I. Buslaev, I. V. Iorsh, I. V. Shadrivov, P. A. Belov, and Y. S. Kivshar, "Plasmons in waveguide structures formed by two graphene layers," *JETP Lett.*, vol. 97, no. 9, pp. 535–539, April 2013.

[40] P. Y. Chen, C. Argyropoulos and A. Alu, "Terahertz antenna phase shifters using integrally-gated graphene transmission-lines," *IEEE Trans. Antennas Propag.*, vol. 61, no. 4, pp. 1528–1537, April 2013.

[41] X. Xia, J. Wang, F. Zhang, Z. Da Hu, C. Liu, X. Yan and L. Yuan, "Multi-mode Plasmonically Induced Transparency in Dual Coupled Graphene-Integrated Ring Resonators," *Plasmonics*, vol. 10, no. 6, pp. 1409–1415, May 2015.

[42] Y. Gao, G. Ren, B. Zhu, L. Huang, H. Li, B. Yin and S. Jian, "Tunable Plasmonic Filter Based on Graphene Split-Ring," *Plasmonics*, vol. 11, no. 1, pp. 291–296, Aug. 2015.

[43] B. Sensale Rodriguez, "Graphene-insulator-graphene active plasmonic terahertz devices," *Appl. Phys. Lett.*, vol. 103, no. 12, pp. 123109 1-4, Sept. 2013.

[44] B. Sensale Rodriguez, R. Yan, L. Liu, D. Jena;, H.G. Xing, "Graphene for Reconfigurable THz Optoelectronics," *Proceedings of the IEEE*, vol 101, no. 7, pp.1705 - 1716, July 2013.

[45] B. Sensale-Rodriguez, "Graphene Based Optoelectronics," *J. Lightwave Techn.*, vol. 33, no. 5, pp. 1100-1108, March 2015.

[46] B. Wang and G. P. Wang, "Plasmonic waveguide ring resonator at terahertz frequencies," *Appl. Phys. Lett.*, vol. 89, no. 13, pp. 1–4, Sept. 2006.

[47] T. Wu, Y. Liu, Z. Yu, Y. Peng, C. Shu, and H. He, "The sensing characteristics of plasmonic waveguide with a single defect," *Opt. Commun.*, vol. 323, no. 7, pp. 44–48, April 2014.

[48] C. Y. Chen, S. C. Wu, and T. J. Yen, "Experimental verification of standing-wave plasmonic resonances in split-ring resonators," *Appl. Phys. Lett.*, vol. 93, no. 3, pp. 2006–2009, July 2008.

[49] J. Wang, W. B. Lu, X. B. Li, X. F. Gu, and Z. G. Dong, "Plasmonic metamaterial based on the complementary split ring resonators using graphene," *J. Phys. D. Appl. Phys.*, vol. 47, no. 32, p. 325102, July 2014.

[50] S. Cakmakyapan, H. Caglayan, and E. Ozbay, "Coupling enhancement of split ring resonators on graphene," *Carbon N. Y.*, vol. 80, no. 1, pp. 351–355, Aug. 2014.

[51] H. J. Chen and K. Di Zhu, "Graphene-based nanoresonator with applications in optical transistor and mass sensing," *Sensors (Switzerland)*, vol. 14, no. 9, pp. 16740–16753, Sept. 2014.

[52] P. Q. Liu, I. J. Luxmoore, S. A. Mikhailov, N. A. Savostianova, F. Valmorra, J. Faist, and G. R. Nash, "Highly tunable hybrid metamaterials employing split-ring resonators strongly coupled to graphene surface plasmons," *Nat. Commun.*, vol. 6, p. 8969, Nov. 2015.

[53] Y. Gao, G. Ren, B. Zhu, L. Huang, H. Li, B. Yin, and S. Jian, "Tunable Plasmonic Filter Based on Graphene Split-Ring," *Plasmonics*, vol. 11, no. 1, pp. 291–296, August 2015.

[54] D. Correas Serrano, J. S. Gomez-Diaz, J. Perruissea-Carrier, Alvarez-Melcon, "A Graphene-based plasmonic tunable low-pass filters in the THz band", *IEEE T. Nano*, vol. 13, no. 6, pp. 1145-1153, Nov. 2014.

[55] H. Deng, Y. Yan, and Y. Xu, "Tunable flat-top bandpass filter based on coupled resonators on a graphene sheet", *IEEE Photonic. Techn. L.*, vol. 27, no. 11, pp. 1161-1164, March 2015.

[56] A. Z. Illic and D. Budimir, "Electromagnetic analysis of graphene based tunable waveguide resonators", *Microw. Opt. Technol. Lett.*, vol. 56, no. 10, July 2014.

[57] C. Zhao and J. Zhang, "Plasmonic Demultiplexer and guiding", *ACS*, vol. 4, no. 11, pp. 6433-6438, Oct. 2010.

[58] G. Wang, H. Lu, X. Liu, D. Mao, and L. Duan, "Tunable multi-channel wavelength demultiplexer based on MIM plasmonic nanodisk resonators at telecommunication regime", *Opt. Exp.*, vol. 19, no. 4, pp. 3513-3518, Feb. 2011.

[59] Ma, Y. Li, and X. Zhang, "Coupled Mode Theory for Surface Plasmon Polariton Waveguides," *Plasmonics*, vol. 8, no. 2, pp. 769-777, Dec. 2012.

[60] A. Locatelli, A. D. Capobianco, M. Midrio, S. Boscolo and C. D. Angelis, "Graphene-assisted control of coupling between optical waveguides," *Opt. Exp.*, vol. 20, no. 27, pp. 28479-28484, Dec. 2012.

[61] D. A. Smirnova, A. V. Gorbach, I. V. Iorsh, I. V. Shadrivov and Y. S. Kivshar, "Nonlinear switching with a graphene coupler," *Phys. Rev. B*, vol. 88, no. 4-15, July 2013.

[62] A. Auditore, C. D. Angelis, A. Locatelli and A. B. Aceves, “Tuning of surface plasmon polaritons beat length in graphene directional couplers,” *Opt. Lett.*, vol. 38, no. 20, Oct. 2013.

[63] H. Li, L. Wang, Z. Huang, B. Sun, X. Zhai and X. Li, “Mid-infrared, plasmonic switches and directional couplers induced by graphene sheets coupling system,” *Europhysics Letters*, vol. 104, no. 3, Nov. 2013.

[64] T. Zhang, X. Yin, L. Chen and X. Li, “Ultra-compact polarization beam splitter utilizing a graphene-based asymmetrical directional coupler,” *Opt. Lett.*, vol. 41, no. 2, Jan. 2016.

[65] M. D. He, K. J. Wang, L. Wang, J. B. Li, J. Q. Liu, Z. R. Huang, L. Wang, L. Wang, W. D. Hu, X. Chen, “Graphene based terahertz tunable plasmonic directional coupler,” *Appl. Phys. Lett.*, vol. 105, no. 081903, pp. 1-5, Aug. 2014.

[66] W. Huang, S. J. Liang, E. Kyoseva and L. K. Ang, “Adiabatic control of surface-plasmon-polaritons in a 3-layers graphene curved configuration,” *Carbon*, Nov. 2017.

[67] F. Xu, H. Zhang and Y. Sun, “Compact graphene directional couplers based on dielectric ridges for planar integration,” *Optik*, vol. 131, pp. 588-591, Feb. 2017.

[68] J. F. Federici, B. Schulkin, F. Huang, D. Gary, R. Barat, F. Oliveira, and D. Zimdars, “THz Imaging and Sensing for Security Applications-Explosives, Weapons, and Drugs,” *Semicond. Sci. Technol.*, vol. 20, pp. 266-280, June 2005.

[69] J. F. Federici, L. Moeller, and K. Su, “Terahertz Wireless Communications,” *Handbook of Terahertz Technology for Imaging, Sensing, and Communications, Woodhead Publishers*, Jan. 2013.

[70] J. Koo, J. Park, Y. Song, S. Lee, K. Lee and J. H. Lee, “Fiber-optic polariztion beam splitter using a reduced graphene-oxide based interlayer,” *Optical Materials*, vol. 46, pp. 324-328, Aug. 2015.

[71] P. Rickhaus, P. Makk, M. Liu, K. Richter and C. Schonenberger, “Gate tuneable beamsplitter in ballistic graphene,” *Appl. Phys. Lett.*, vol. 107, pp. 251901 1-5, Nov. 2015.

[72] X. B. Li, J. X. Hong, W. B. Lu and J. Wang, “Multiple beams-splitter based on graphene,” *International Journal of Optics*, vol. 2016, no. 2016, pp. 7651216 1-5, June 2016.

[73] Y. Song, L. Xie, Z. G. Shi, S. Li and J. Zhang, “Spin-valley beam splitter in graphene,” *AIP Advances 6*, pp. 115215 1-5, Nov. 2016.

[74] Y. Wang, X. R. Hong, T. Sang and G. F. Yang, "Tunable 1x2 plasmonic splitter of dielectric-loaded graphene waveguide based on multimode interference," *Appl. Phys. Exp.*, vol. 9, no. 12, pp. 125102 1-3, Nov. 2016.

[75] P. Qiu, W. Qiu, Z. Lin, H. Chen, Y. Tang, J. Wang, Q. Kan and J. Pan, "Ultra-compact tunable graphene-based plasmonic multimode interference power splitter in mid-infrared frequencies," *China Inf Sci 2017*, vol. 60, no. 8, pp. 082402 1-6, Aug. 2017.

[76] J. N. George and M. G. Madhan, "Analysis of single band and dual band graphene based patch antenna for terahertz region," *Physica E.: Low-Dimensional systems and nanostructures*, vol. 94, pp. 126-131, Oct. 2017.

[77] M. Bozzi, L. Pierantoni and S. Bellucci, "Applications of Graphene at microwave frequencies," *Radioengineering*, vol. 24, no. 3, Sept. 2015.

[78] R. Bala, A. Marwaha and S. Marwaha, "Comparative analysis of zigzag and armchair structures for graphene patch antenna in THz band," *J. Mater. Sci.: Mater. Electron.*, vol. 27, no. 5, pp. 5064-5069, Jan. 2016.

[79] I. Llaster, C. Kremers, A. C. Aparicio, J. M. Jornet, E. Alarcon and D. N. Chigrin, "Graphene-based nano-patch antenna for terahertz radiation," *Photonics and Nanostructures-Fundamentals and Applications*, vol. 10, no. 4, pp. 353-358, Oct. 2012.

[80] J. Jornet and I. F. Akyildiz, "Graphene-based plasmonic nano-antenna for terahertz band communication in nanonetworks," *IEEE J. Sel. Areas Commun.*, vol. 32, no. 12, pp. 685-694, Dec. 2013.

Chapter 2

Electromagnetic Modeling of Graphene based wave guiding structures and discontinuities

2.1 Introduction

Plasmonic waveguides have been studied for a long time [1-5]. The electromagnetic wave propagation in these waveguiding structures depend on the propagation of SPPs in inert metals [6-10]. Photonic devices and plasmonic networks have been developed utilizing these waveguides [11-15]. Graphene nano-ribbon waveguides have also been studied [16-18]. In this section we will describe the characteristics of graphene films developed over silicon substrate, electromagnetic modelling of graphene [19-24] based plasmonic waveguides (GPWs) and variants of GPPW [25-35] such as graphene plasmonic nanostrip waveguide (GPNSW), graphene plasmonic suspended nanostrip waveguide (GPSNSW), graphene plasmonic coplanar waveguide (GPCPW), graphene plasmonic graphene backed coplanar waveguide (GB-GPCPW). Apart from discussing the waveguide properties of these guided wave structures, we will also describe the behaviour of physical discontinuties [36-46] and their electromagnetic behaviour.

2.2 Deposition and characterization of graphene for THz integrated circuits

Multi-layer graphene can be deposited on 300 nm SiO_2/Si wafer using spin-coating method. For the purpose, firstly, the sample is prepared and then, characterized with various techniques.

Sample Preparation and Characterization

In the fabrication procedure of graphene film on Si substrate with 300 nm thermal oxide on its top, firstly, the graphite powder flakes (1 gm) were added to concentrated H_2SO_4 (46 ml). Then, after stirring it for one hour, 0.6 gm $NaNO_3$ and 3 gm $KMnO_4$ were added slowly under ice bath (temperature should not exceed 20^oC), and thereafter, the stirring was continued for 24 hours. Finally, it was washed with water several times and then dried in oven to obtain graphene oxide powder. It can be stored indefinitely for future use. This is modified Hummer's method [47-49].

This powder was used to make aqueous solution of 20 ml with the concentration of 1 mg/ml. Now, this solution can be characterized with the help of Infra-Red (IR), and Photoluminiscence (PL) spectroscopy [48]. For the infra-red spectroscopy, the absorbance and transmittance spectra are shown in Fig. 2.2.1(a) and (b). In the absorbance spectra, as shown in Fig. 2.2.1, the absorption peak of obtained graphene oxide is at 250 nm because of graphene sheets. GO has a peak at 1081 cm^{-1} which is attributed to the C-O bond, confirming the presence of oxide functional groups after the oxidation process. The peaks in the range of 1630 cm^{-1} to 1650 cm^{-1} show that the C=C bond still remained before and after the oxidation process. The absorbed water in GO is shown by a broad peak at 2885 cm^{-1} to 3715 cm^{-1} contributed by the O-H stretch of H_2O molecules. This supports the fact that GO is a highly absorptive material, as verified by its ability to become a gel-like solution.

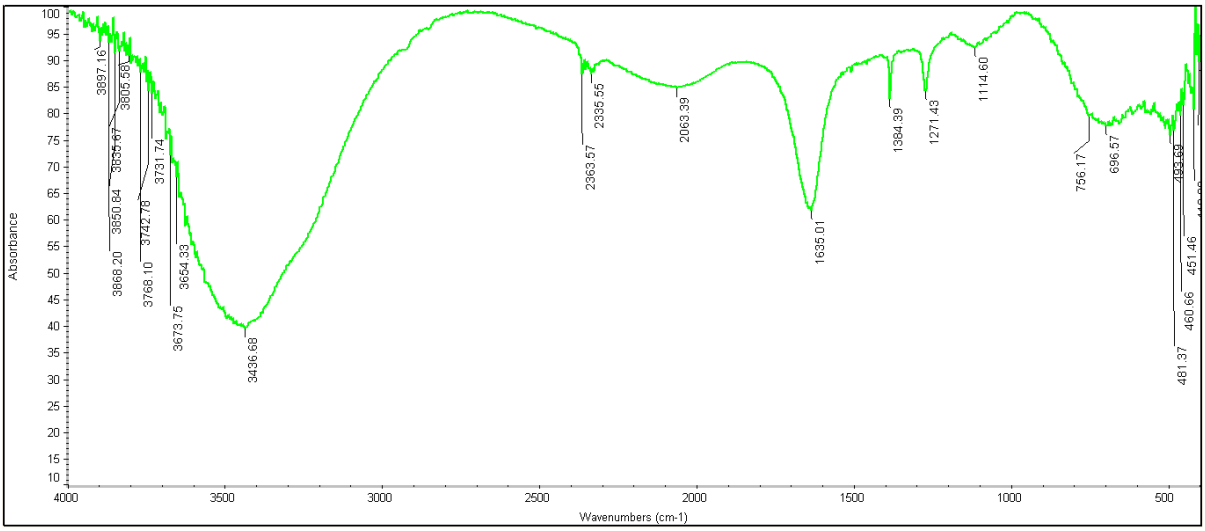

(a)

Next, the solution is characterized with PL spectroscopy. In this plot (Fig. 2.2.2), as the center wavelength of incident light increases, in response the output photon intensity peaks shift to the right side. This is due to the emission from the electron gases in the solution. Here, wavelengths in the legends show the excitation energy.

Then, the solution is spin coated on 300 nm SiO_2/Si wafer at the speed of 6000 rpm for 30 s. It is left for drying at room temperature for 24 hours. The characterization is done by FE-SEM. The images are shown for various resolutions.

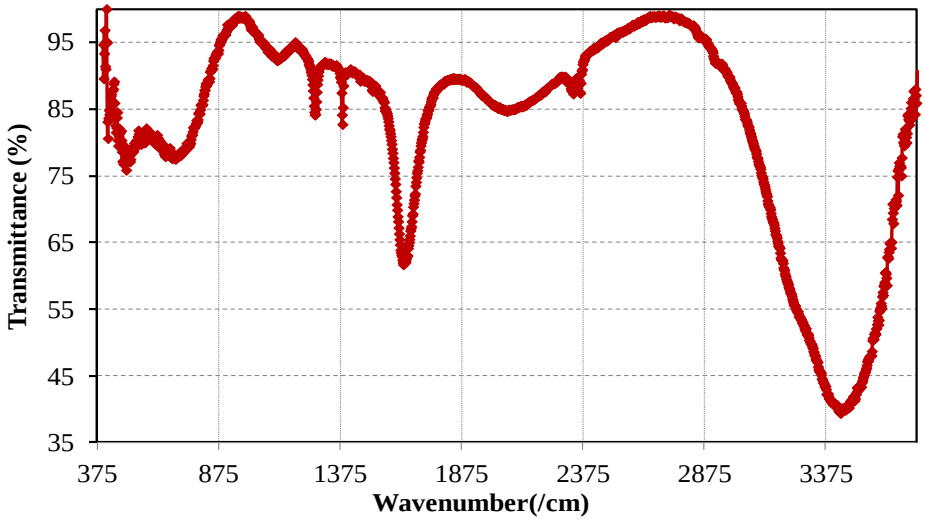

(b)

Fig. 2.2.1. (a), (b) Absorbance and transmittance spectra of aqueous solution of graphene oxide.

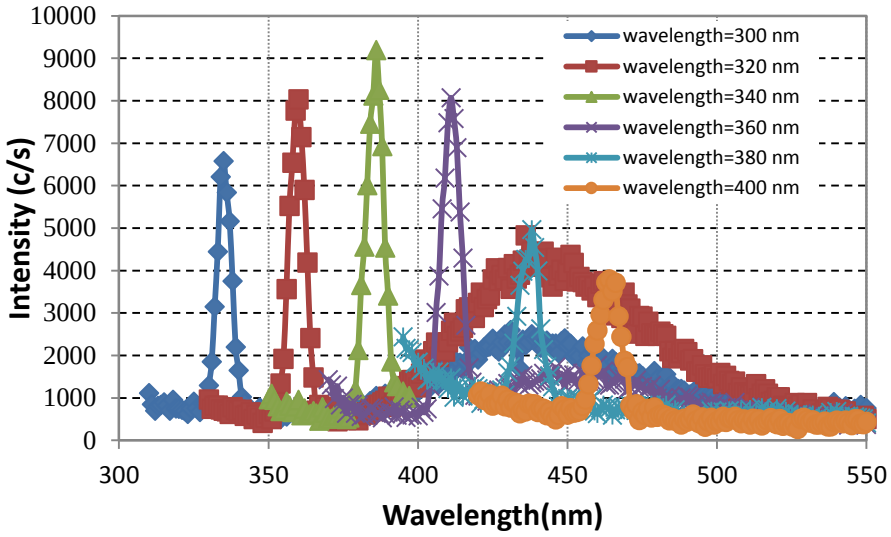

Fig. 2.2.2 PL spectra of aqueous solution of graphene oxide.

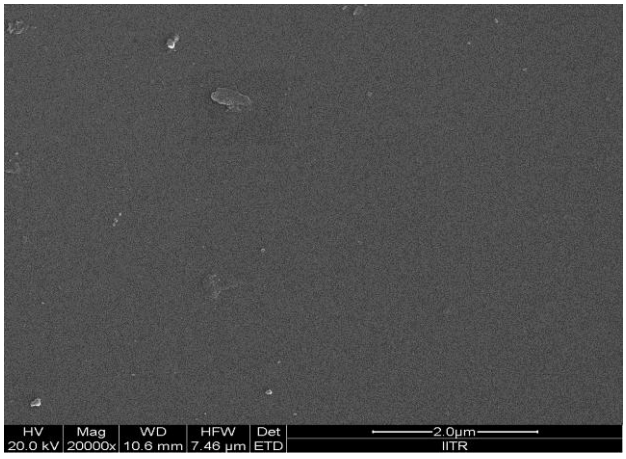

(a)

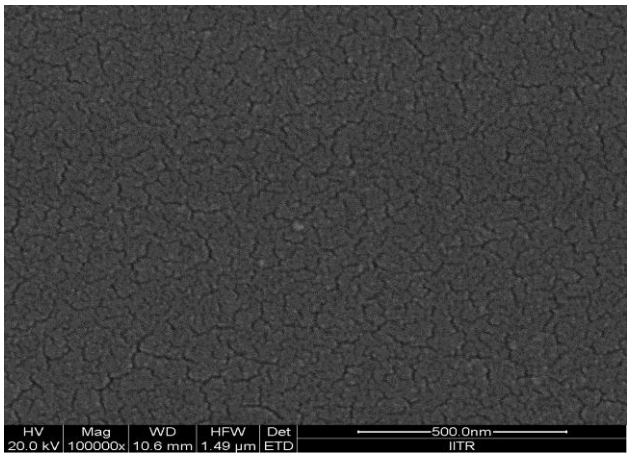

(b)

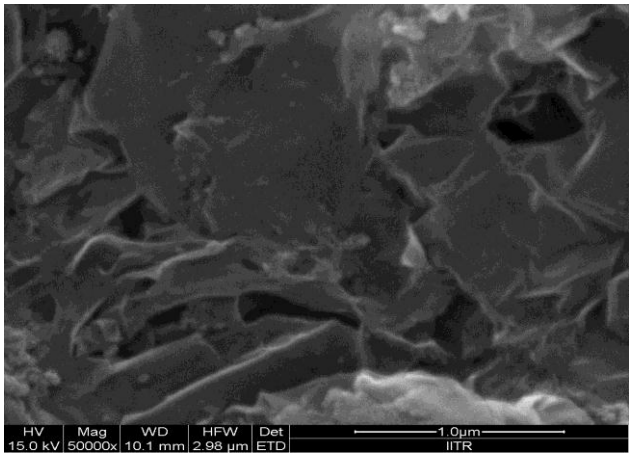

(c)

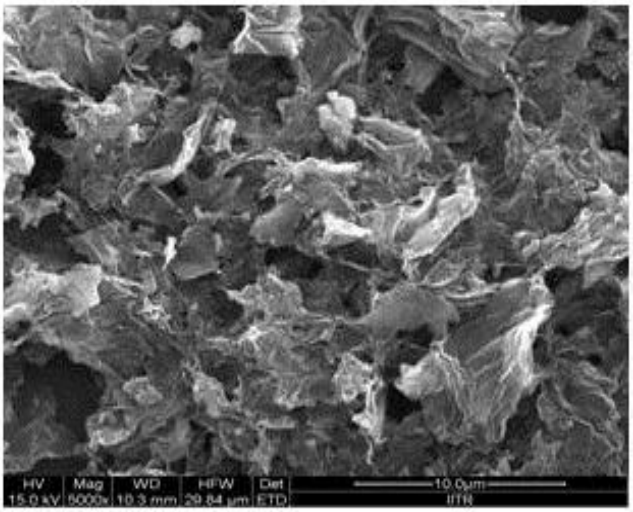

(d)

Fig.2.2.3. (a), (b), (c), (d) SEM images of graphene material.

Fig. 2.2.3 (a), (b), (c) and (d) represent the SEM images of the deposited graphene material on Si/SiO_2 dielectric substrate, showing the presence of graphene on dielectric. The EDX images for the graphene deposition on SiO_2/Si wafer are shown in Fig. 2.2.4, where the carbon peaks show the presence of graphene. In this manner, graphene deposition can be achieved on SiO_2/Si wafer. This film deposition method can be improved further to design passive integrated circuits.

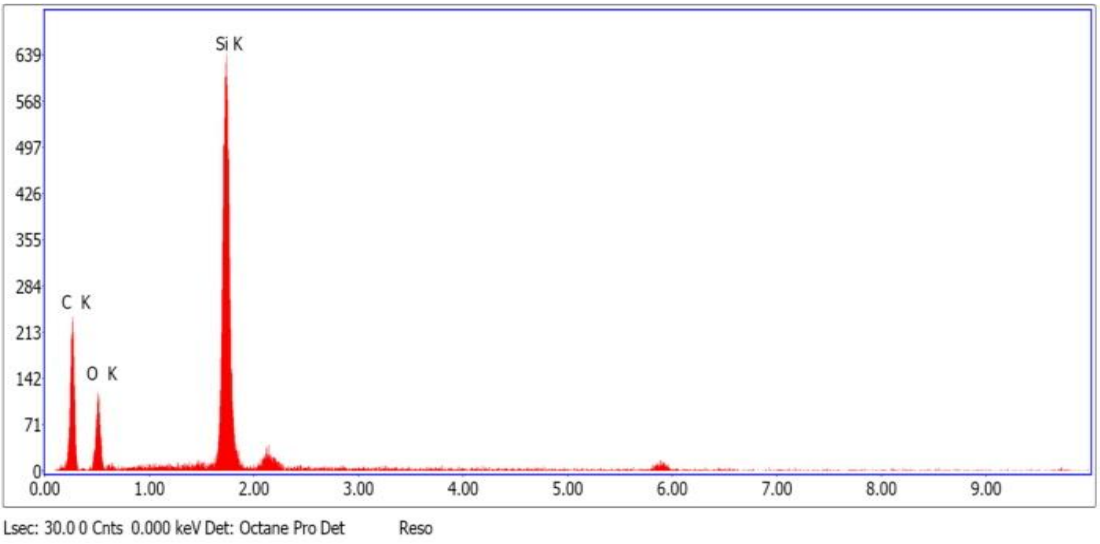

Fig. 2.2.4 EDX image of graphene material.

As the THz circuit characterization facilities like network analyzer and associated THz components, probe station for nanoscale resolution, etc. are not available in the institute, further research work has been proceeded in the theoretical domain.

2.3 Electromagnetic modelling of variants of Graphene Parallel Plate Waveguide (GPPW): Simplest graphene based plasmonics waveguide structure supporting electromagnetic wave propagation is GPPW shown in Fig. 2.3.1 (a, b). By changing the width of one plate of GPPW and composition of dielectric material between the plates, we can obtain several other waveguide structures which have either planar or quasi planar geometry as shown in Fig. 2.3.1. These waveguide are referred as graphene plasmonic nanostrip waveguide, graphene plasmonics suspended nanostrip waveguide, graphene plasmonics coplanar waveguide and graphene plasmonics graphene backed coplanar waveguide. The details of each of these waveguide structures are discussed in subsequent sections.

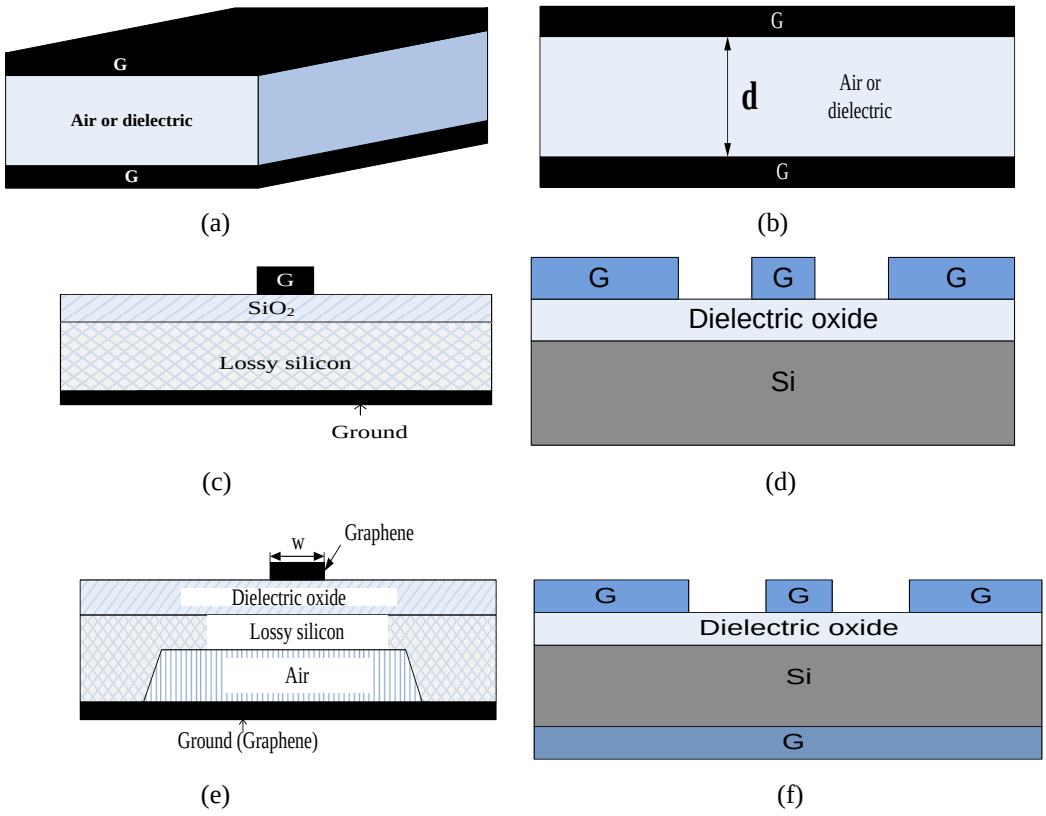

Fig. 2.3.1(a) 3-D view of GPPW **(b)** 2-D cross-sectional view of GPPW **(c)** Cross-sectional view of graphene plasmonic nanostrip waveguide **(d)** Cross-sectional view of graphene plasmonic coplanar waveguide **(e)** Cross-sectional view of graphene plasmonic suspended nanostrip waveguide **(f)** Cross-sectional view of graphene plasmonic graphene-backed coplanar waveguide. Here, G stands for graphene material.

2.3.1 Graphene plasmonic nanostrip waveguide (GPNSW): The geometry of graphene based plasmonic nanostrip waveguide along with its two-wire transmission line equivalent circuit has been shown in Fig. 2.3.1.1(a). One can obtain the geometry of nanostrip waveguide from GPPW by varying the width of upper plate; while keeping lower plate unchanged. Equivalent circuit representation requires knowledge of propagation constant γ ($\gamma=\alpha+j\beta$) and the characteristic impedance Z_0 of the nanostrip waveguide geometry [50-52]. The transmission line equivalent circuit has been obtained using full wave e. m. solver CST Microwave studio (Appendix). The values of chemical potential for graphene conduction in the THz frequency region ranges from $0<\mu_c<1$ (units in eV). The actual parameters used in this case are: chemical potential, $\mu_c=0.5$ eV; relaxation time, $\tau=0.5$ ps, corresponding mobility, $\mu=30{,}000$ $cm^2V^{-1}s^{-1}$ and temperature, T=300 K. In the simulation, we have used following parameters to obtain the transmission line characteristics of this waveguide geometry: width of the nanostrip waveguide is w, thickness of silicon dioxide d = 40 nm, h=100 nm, $t=t_0=0.5$nm and chemical potential μ of graphene strip: varied from 0.4 to 0.7. Aspect ratio has been defined as:

$\frac{w}{(d+h)} = \frac{w}{h'}$. Variation of normalized phase constant (β/k_0) and normalized attenuation constant (α/k_0) with frequency and aspect ratio has been shown in Figures 2.3.1.1(b-d).

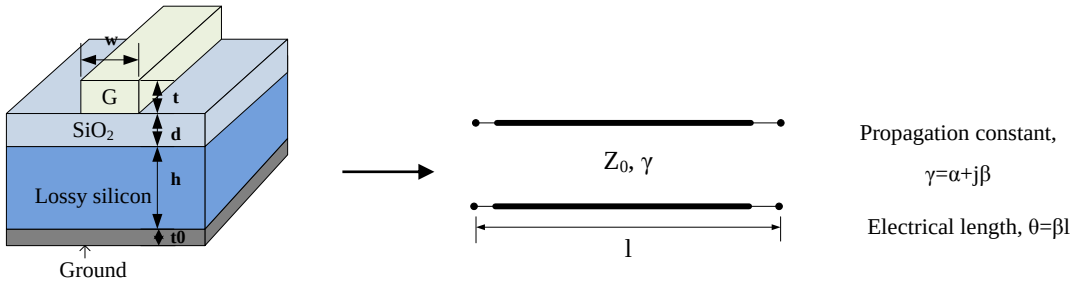

Fig. 2.3.1.1(a) Geometry of graphene plasmonic nanostrip waveguide along with its 2-wire transmission-line equivalent circuit.

The characteristic impedance of the graphene based plasmonics nanostrip waveguide has been computed using the relation $Z_{VI} = \frac{V}{I}$ or $Z_{PV} = \frac{V^2}{P}$ or $Z_{PI} = \frac{P}{I^2}$, where P is the power and V and I are the voltage and currents. The most appropriate definition for nanostrip waveguide is Z_{PI} which is computed on the basis of power and current. Power flow can be obtained from the knowledge of electric and magnetic fields and current can be computed with the help of integrating magnetic field lines along a known path. The variation in characteristic impedance of the nanostrip waveguide with respect to aspect ratio has been given in Fig. 2.3.1.1(e). It is clear from the Fig. 2.3.1.1 (e) that if, we increase the aspect ratio, there is a decrease in characteristic impedance. The highest value of the characteristic impedance for graphene based nanostrip waveguide is around ~3000 Ω, which is large in comparison to its microwave counterpart i.e. microstrip line. The large values of characteristic impedance play a major role in radical miniaturization of THz integrated circuits. The values for α, β and Z_0 in case of metal waveguides are 0.59 m^{-1}, 42.88 m^{-1} and 50 Ω, respectively, showing better performance of graphene plasmonic waveguide over metal waveguide. Closed form expressions have been derived to obtain normalized phase constant and characteristic impedance of graphene based plasmonics nanostrip waveguide as given in Eq. (2.3.1.1 and 2.3.1.2). The propagation length of the propagating surface plasmon polariton wave (SPP) are also computed using full wave e. m. simulation and it has been shown in Fig. 2.3.1.1(f).

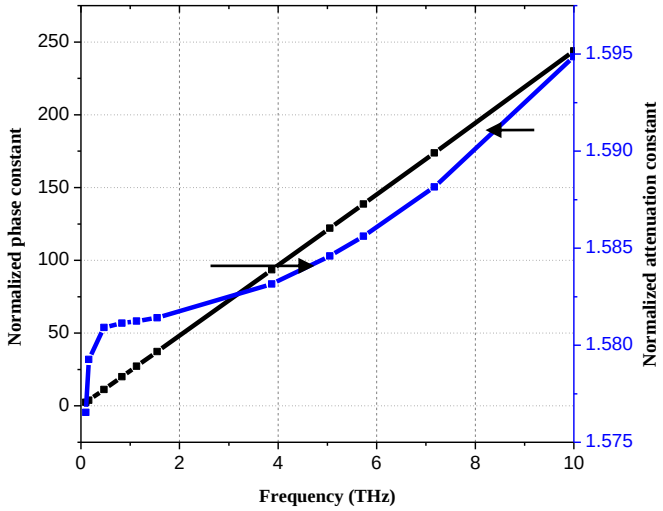

Fig. 2.3.1.1(b) Plots of β/k_0 and α/k_0 with frequency.

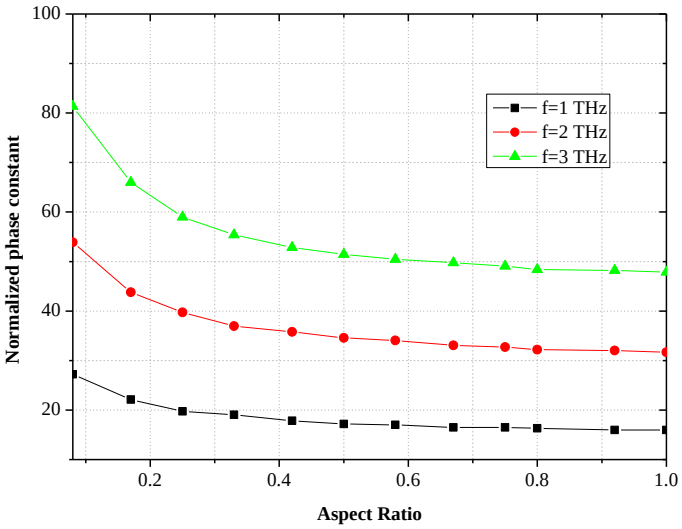

Fig.2.3.1.1(c) Plot of β/k_0 with aspect ratio.

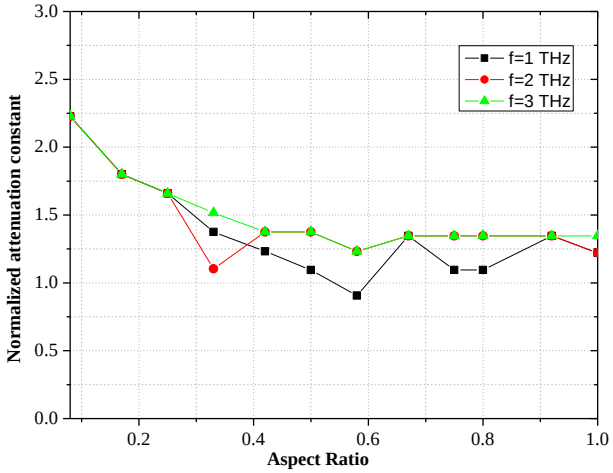

Fig. 2.3.1.1(d) Plot of α/k_0 with aspect ratio.

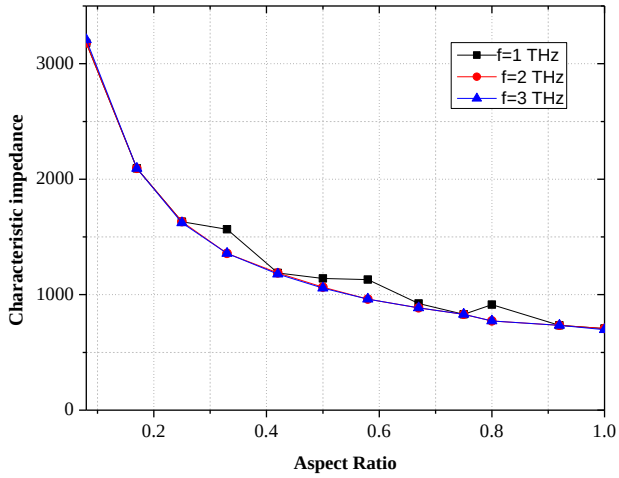

Fig. 2.3.1.1(e) Plots of Z_0 with aspect ratio.

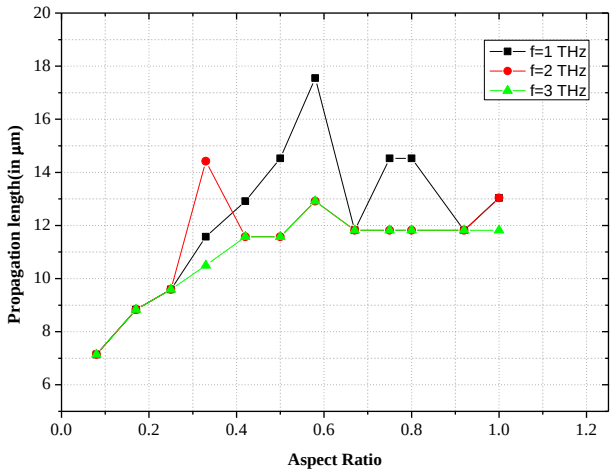

Fig. 2.3.1.1(f) Plots of L_{spp} with aspect ratio.

Closed form expression for computing normalized propagation constant ($\frac{\beta}{k_o}$) is given as:

$$\frac{\beta}{k_o} = A_2 f(A_1(w/h)^2 + B_1(w/h) + C_1)\left((A_3 d^2 + B_3 d + C_3)\right)e^{-2.66\sigma}$$

…….(2.3.1.1)

where σ = conductivity, *f*= frequency, h = is thickness of silicon layer, and d is thickness of SiO_2 layer. Here,

$$A_1 = \frac{\left(5.4533h^2 - 7.9759h - 605.088\right)}{\left(h^2 - 868.09h - 6063.3556\right)}$$

$$B_1 = \frac{\left(1856516h^2 + 32475202h + 499886728\right)}{\left(h^2 - 192087878h - 5114185973\right)}$$

$$C_1 = \frac{\left(0.8804h^2 - 4.6082h - 124.046\right)}{\left(h^2 - 1.2433h + 225.4\right)}$$

$$A_2 = \frac{\left(0.8703h^2 - 0.9625h - 35.7841\right)}{\left(h^2 + 3.01594h + 31.2524\right)}$$

$$A_3 = \frac{\left(0.6721h^2 - 8.9619h - 203.4982\right)}{\left(h^2 + 19.4096h - 173.1685\right)}$$

$$B_3 = \frac{\left(-6.4543h^2 - 304h - 119225.99\right)}{\left(h^2 - 161.2127h - 3131.4411\right)}$$

$$C_3 = \frac{\left(34719h^2 + 2862283h + 57340555\right)}{\left(h^2 - 257562.68h + 24617562\right)}$$

The closed form expression for computing characteristic impedance has been derived using curve-fitting equations from the expression for normalized propagation constant and it is given as:

$$Z_o = e^{\left(-1.5379(w/h) - 6.3263f + 2.6518\sigma + \frac{0.01475\beta}{k_o} + 8.0039\right)} \quad \text{.....(2.3.1.2)}$$

The calculated and simulated results agree well as depicted in Fig. 2.3.1.2(a) and 2.3.1.2(b).

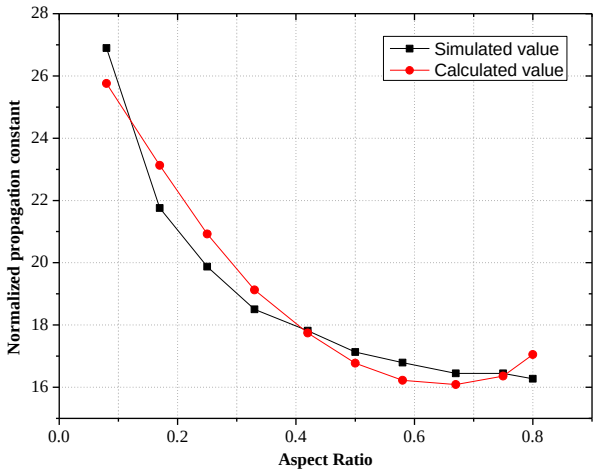

Fig. 2.3.1.2(a) Plots of β/k_0 with aspect ratio (w/h').

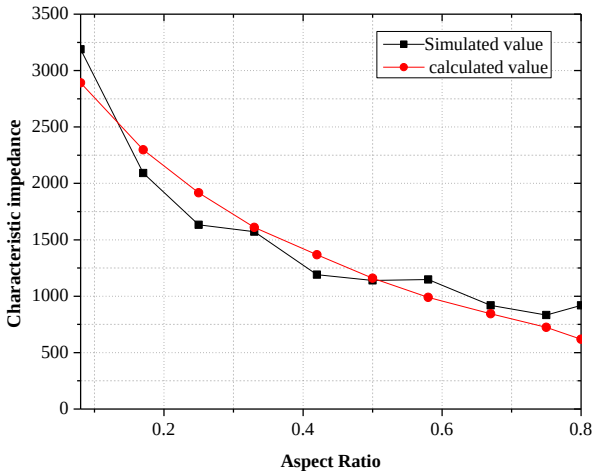

Fig. 2.3.1.2(b) Plot of Z_0 with aspect ratio (w/h').

Lumped element equivalent circuit of graphene plasmonics nanostrip waveguide has been shown in Fig. 2.3.1.3.

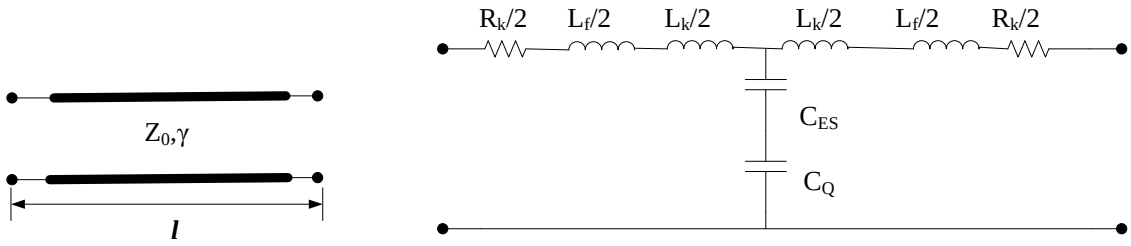

Fig. 2.3.1.3 RF equivalent circuit of nanostrip waveguide.

The equivalent circuit parameters are given by following equations.

$$Z' = R'_K + j\omega(L'_F + L'_K)$$

And $$Y' = j\omega C'_{ES} \quad \ldots(2.3.1.3)$$

Where $$C'_{ES} = 2\epsilon_r\epsilon_0\beta W \quad \ldots(2.3.1.4)$$

$$L'_F = \frac{\mu_0}{2\beta W} \quad \ldots(2.3.1.5)$$

Also, at higher frequencies,

$$L'_K \approx \frac{1}{\omega W \sigma_i} \quad \ldots(2.3.1.6)$$

and $$R'_K \approx \frac{2\sigma_r}{W\sigma_i^2} \quad \ldots(2.3.1.7)$$

Here, Z' is characteristic impedance of graphene nanostrip transmission line; R_K' is kinetic resistance; L_F' is Faraday inductance; L_K' is kinetic inductance; Y' is characteristic admittance; C_{ES}' is electrostatic capacitance; ω is angular frequency; ε_r is permittivity of dielectric which in this case is air; ε_0 is dielectric permittivity of vacuum; β is propagation constant; W is width of graphene layer; μ_0 is permeability of vacuum and σ_i is intrinsic conductivity of conductor which in this case is graphene. Due to finite value of chemical potential of graphene strip, the effect of the presence of quantum capacitance in the equivalent circuit can be neglected; hence, it is not included.

When integrated circuits are designed using graphene plasmonic nanostrip waveguide, it is difficult to avoid physical discontinuities in the structure. Some of the well known discontinuities are: open end, short circuit, gap, step, T-junction etc. The occurrence of physical discontinuity in the structure disturbs either electric field vectors or flow of current or magnetic field vectors. The disturbance in electric field can give the effect of extra capacitance and disturbance in magnetic field will give the increase in inductance in the overall equivalent circuit of the waveguide structure. Fig. 2.3.1.4 (a), (b) and (c) shows the discontinuities discussed in this chapter. Full wave e. m. solver CST microwave studio can be used to obtain S-parameters of these discontinuities and subsequently deriving its lumped element equivalent circuit.

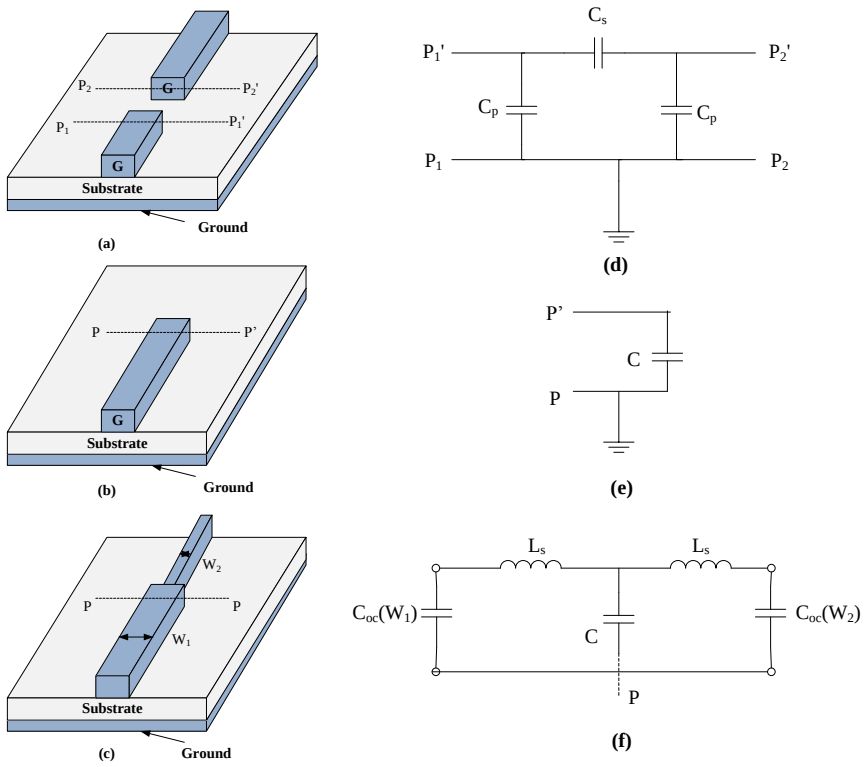

Fig. 2.3.1.4 Discontinuities in graphene based nanostrip waveguide. (a) gap. (b) Open. (c) Step

2.3.2 Graphene plasmonic suspended nanostrip waveguide (GPSNSW): This waveguide geometry is obtained, if we introduce air gap between ground and substrate as shown in Fig. 2.3.2.1(a). The overall effect of this waveguide geometry is the reduction in effective dielectric constant of the medium and hence reduced loss, increased operational bandwidth and increased characteristic impedance. The geometry of graphene plasmonic suspended Nanostrip waveguide comprises of a silicon substrate: ε_r=11.9 and σ=0.00025 S/m over which a layer of silicon dioxide (ε_r=3.9) is deposited. A graphene layer present on the backside of the substrate acts as ground plane for the waveguide structure. The thickness of different materials used in the simulation are: thickness of monolayer graphene $t=t_0$=0.5 nm, thickness of Si substrate h=100 nm and thickness of SiO_2 layer d =20 nm. The air gap is at an angle of 54.7 degrees with a gap above of thickness, d1= 10 nm. Similar to graphene plasmonics nanostrip waveguide, this guided wave structure can also be modeled with the help of two-wire transmission line equivalent circuit. The transmission line parameters such as normalized phase and attenuation constant, characteristic impedance and propagation length have been given as a function of aspect ratio i.e. w/h′ as shown in Fig. 2.3.2.1 (d-g). From the Fig. 2.3.2.1 (d), it is evident that characteristic impedance for this waveguide structure is very high and it is of the order of 6 KΩ.

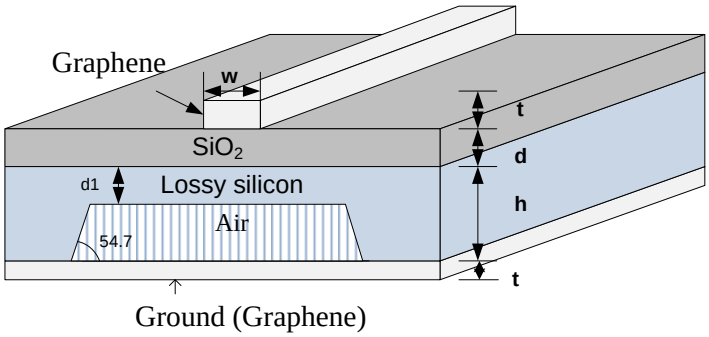

Fig. 2.3.2.1(a) Design of suspended nanostrip transmission line, where G stands for graphene and the ground layer also consists of graphene.

The closed-form expressions have been derived using the curve-fitting approach so that propagation constant and characteristic impedance can be easily calculated during the design work. The normalized phase constant and characteristic impedance for graphene plasmonics suspended nanostrip waveguide are given as:

$$\frac{\beta}{k_o} = A_2 f(A_1(w/h)^2 + B_1(w/h) + C_1)\left(\left(A_3 d^2 + B_3 d + C_3\right)\right) e^{-12.855\sigma}$$

…….(2.3.2.1)

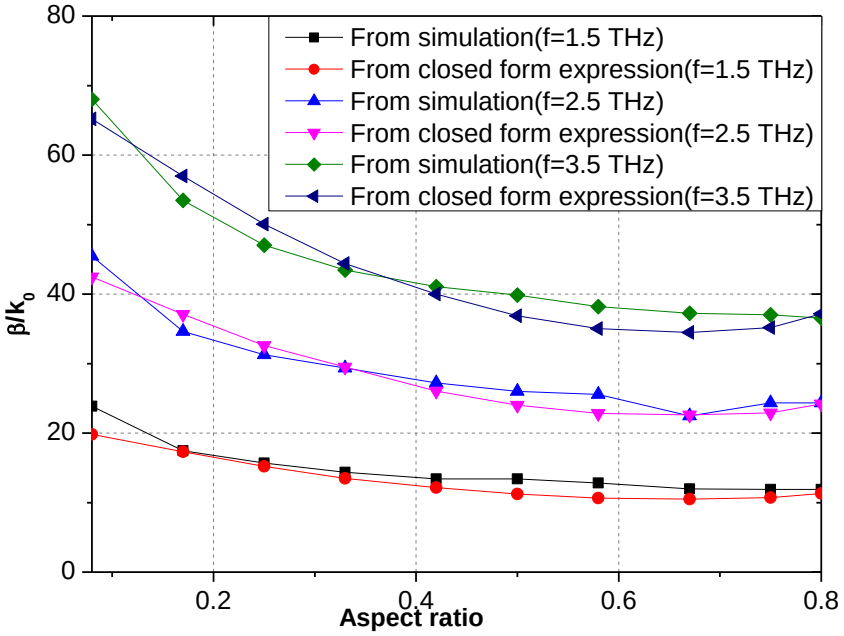

Fig. 2.3.2.1(b) Plot of β/k_0 with w/h ratio.

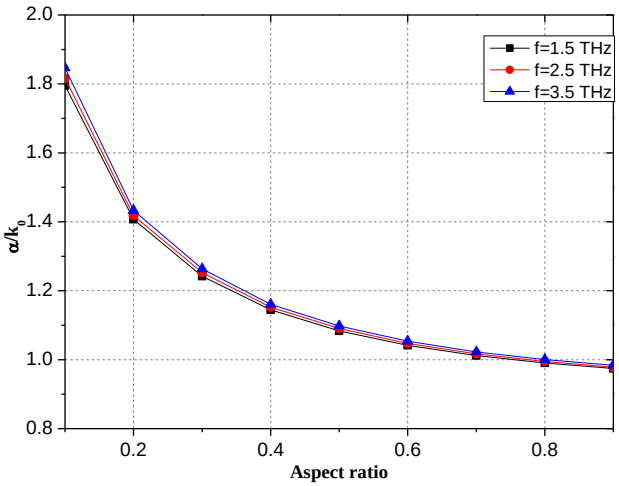

Fig. 2.3.2.1(c) Plot of α/k_0 with w/h ratio.

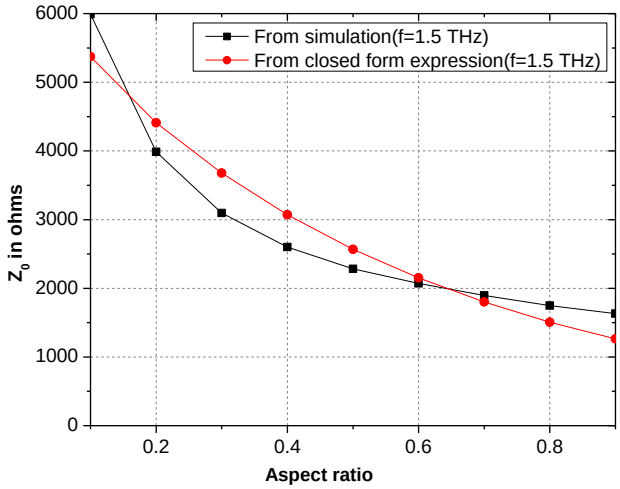

Fig. 2.3.2.1(d) Plot of Z_0 with w/h ratio at frequency, *f*=1.5 THz.

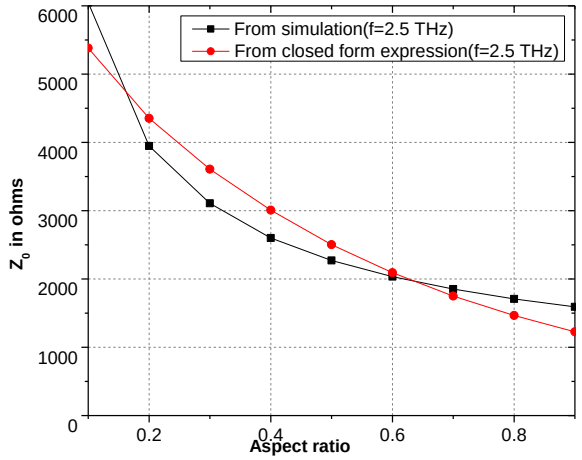

Fig. 2.3.2.1(e) Plot of Z_0 with w/h ratio at frequency, *f*=2.5 THz.

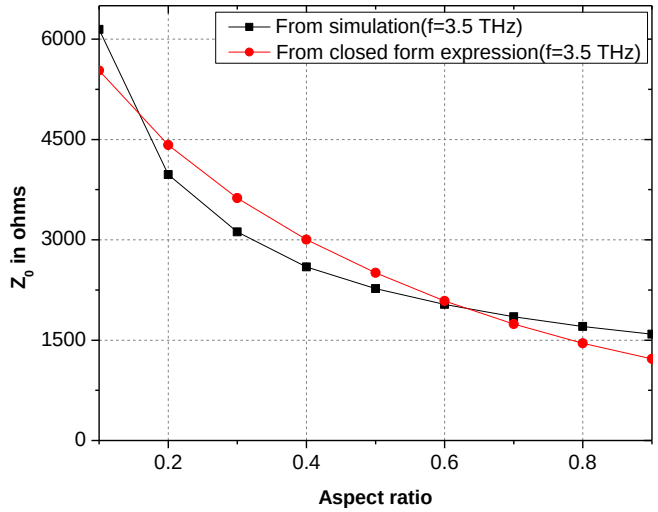

Fig. 2.3.2.1(f) Plot of Z_0 with w/h ratio at frequency, *f*=3.5 THz.

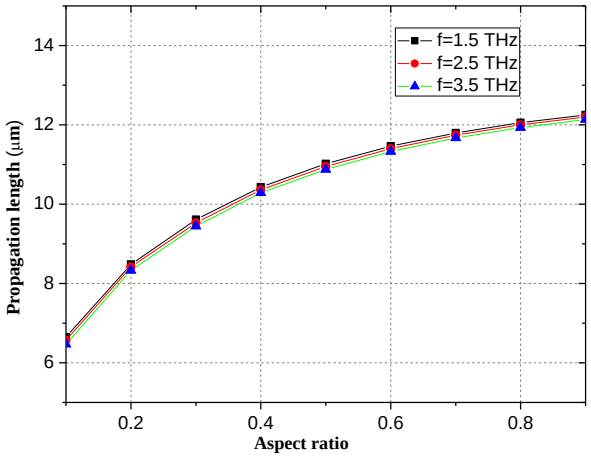

Fig. 2.3.2.1(g) L_{spp} with aspect ratio at frequencies, *f*=1.5 THz, *f*=2.5 THz and *f*=3.5 THz.

where

$$A_1 = \frac{\left(0.0000008186426h^2 - 0.000005741778h + 0.00153540628\right)}{\left(h^2 + 0.000001428464h - 0.01028940621\right)}$$

$$B_1 = \frac{\left(0.00000729628h^2 - 0.00316782490h + 0.25889104067\right)}{\left(h^2 + 0.00008387767h + 0.03249911566\right)}$$

$$C_1 = \frac{\left(0.00000226708h^2 - 0.00072225229h + 0.02320356799\right)}{\left(h^2 + 0.00004741758h - 0.00077150191\right)}$$

$$A_2 = \frac{\left(0.00012925767h^2 + 0.00672921587h + 0.70355612897\right)}{\left(h^2 - 0.000000774019h - 0.00358137783\right)}$$

$$A_3 = \frac{\left(0.000000212281h^2 - 0.00008215508h - 0.01108422066\right)}{\left(h^2 + 0.00000619957h + 0.00025100378\right)}$$

$$B_3 = \frac{\left(0.00376644876h^2 + 0.20308313729h + 3.1364\right)}{\left(h^2 + 0.00168112835h - 0.07306\right)}$$

$$C_3 = \frac{\left(128995h^2 + 6700185h + 399353033\right)}{\left(h^2 + 6021.49h + 115070\right)}$$

and

$$Z_o = e^{\left(0.1548(w/h)+0.0026f+8.6959\sigma+\frac{0.0000000267\beta}{k_o}+0.1275\right)}$$

……(2.3.2.2)

2.3.3 Graphene plasmonic coplanar waveguide (GPCPW): Both graphene plasmonics nanostrip waveguide and graphene plasmonics suspended nanostrip waveguide have their guiding strip and ground plane on the opposite side of the substrate. Graphene plasmonic coplanar waveguide shown in Fig. 2.3.3.1(a) represents another variant of GPPW in which guiding strip and ground plane are present on the same side of the substrate; hence it is uniplanar waveguide structure. This plasmonic waveguide supports two modes viz. even mode and odd mode. Even mode has characteristics similar to quasi TEM mode and it is desired. Odd mode is undesired and it can be suppressed by properly selecting waveguide geometry.

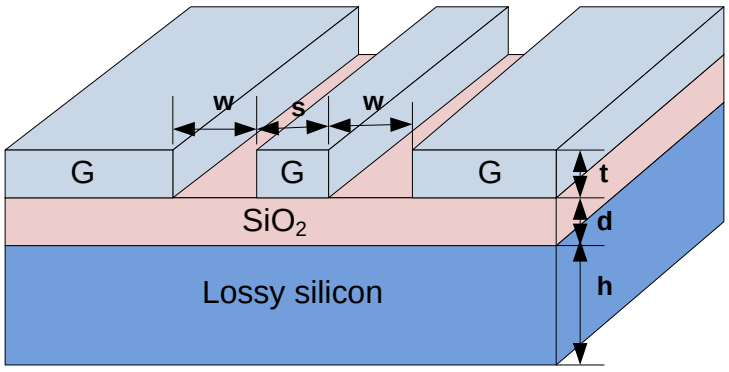

Fig. 2.3.3.1(a) Design of Graphene coplanar waveguide (GCPW) where G stands for graphene material.

The characteristic impedance, Z_0 of odd modes and even modes have been shown in Fig. 2.3.3.1(b) as a function of aspect ratio. We can conclude from the figure that the characteristic impedance decreases with increase in the strip width, s. Fig. 2.3.3.1(c) shows that the decrease in characteristic impedance

for odd and even modes of GPCPW with increase in frequency. The variation in the characteristic impedance for odd and even mode as a function of frequency is shown in Fig. 2.3.3.1 (d-e). The variation in phase constant and attenuation constant as a function of aspect ratio are shown in Fig. 2.3.3.1 (f-g). Fig. 2.3.3.1 (h) shows the decrease in characteristic impedance of GPCPW with increase in chemical potential. The variation in propagation length of SPP as a function of aspect ratio has been shown in Fig. 2.3.3.1 (i), which indicates high field confinement. The closed form expressions for the determination of normalized phase constant and characteristic impedance of desired even mode for GPCPW are given by eq. (2.3.3.1 and 2).

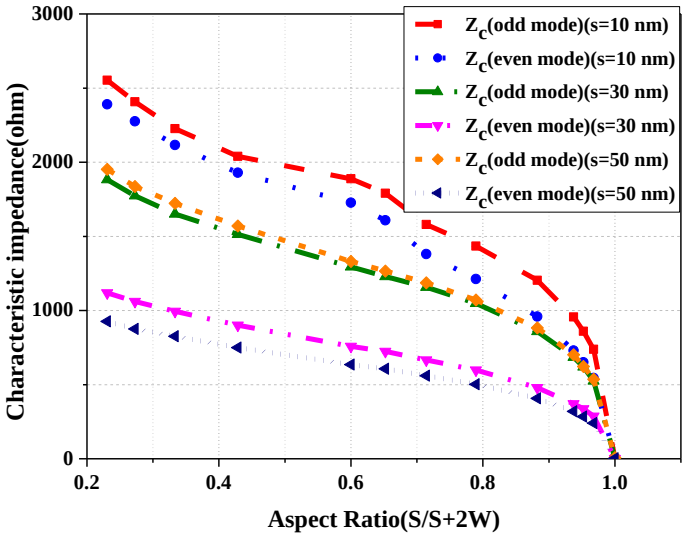

Fig. 2.3.3.1(b) Plot of Z_0 with aspect ratio of GPCPW.

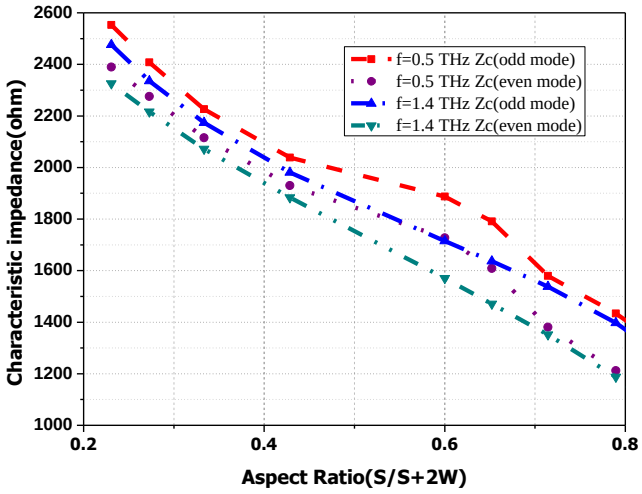

Fig. 2.3.3.1(c) Plot of Z_0 with aspect ratio.

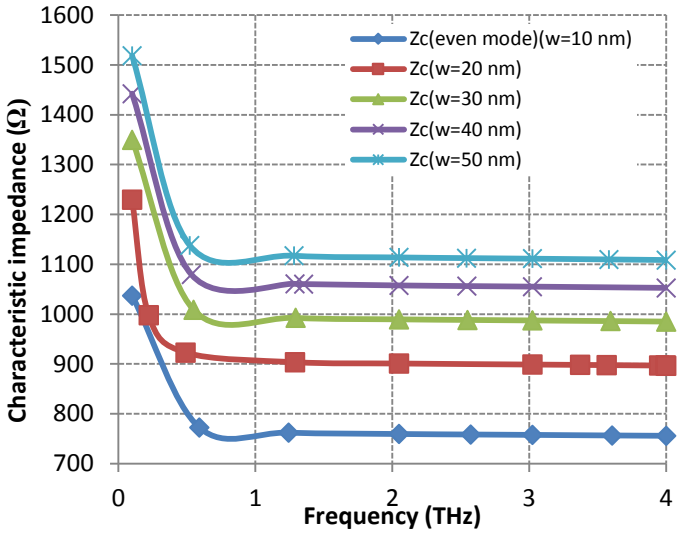

Fig. 2.3.3.1(d) Plot of Z_0 vs frequency for even mode.

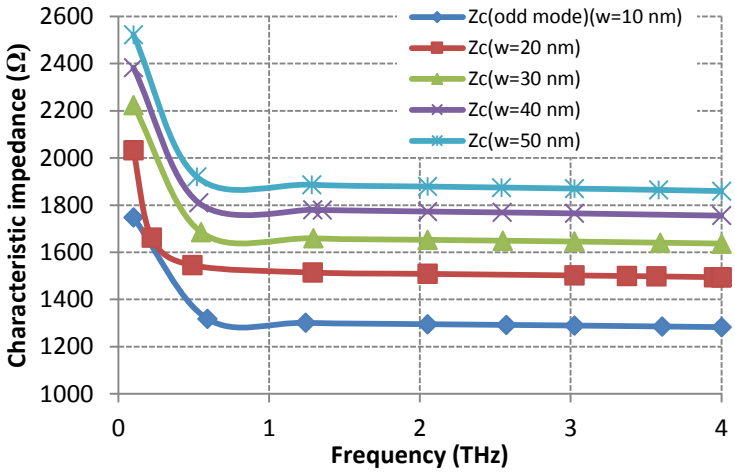

Fig. 2.3.3.1(e) Plot of Z_0 vs frequency for odd mode.

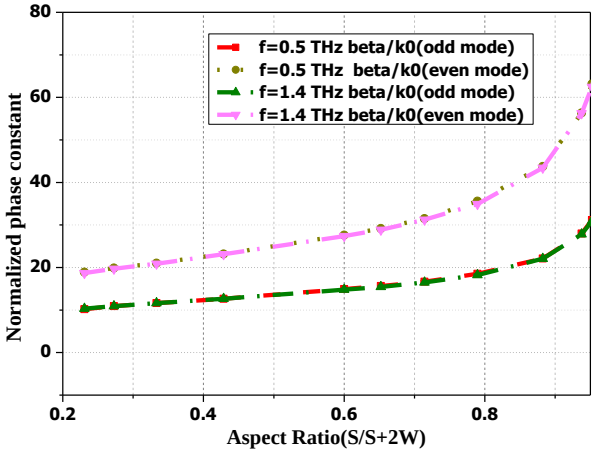

Fig. 2.3.3.1 (f) Plot of β/k_0 vs aspect ratio of GCPW.

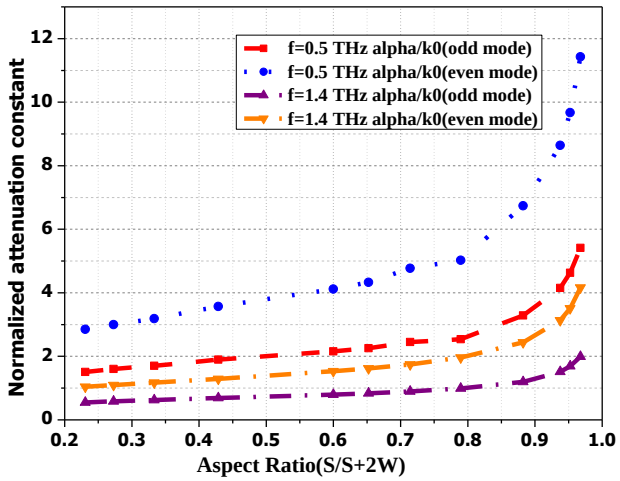

Fig. 2.3.3.1 (g) Plot of α/k_0 vs aspect ratio of GCPW.

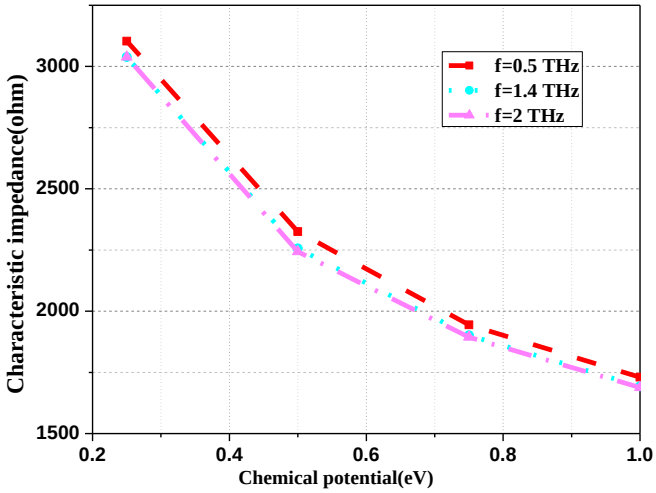

Fig. 2.3.3.1 (h) Plot of Z_0 vs chemical potential of GCPW.

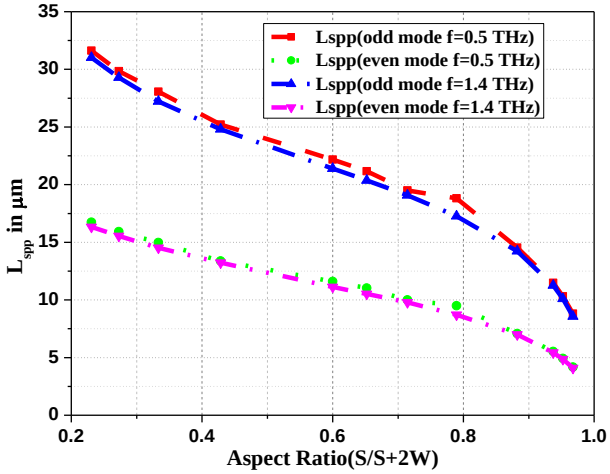

Fig. 2.3.3.1 (i) Plot of L_{spp} vs aspect ratio of GCPW.

The normalized propagation constant is derived to give

$$\frac{\beta}{k_o} = A_3 f\left(A_1\left(s/(s+2w)\right)^2 + B_1\left(s/(s+2w)\right) + C_1\right)\left(A_2(s+2w) + (A_4 d_2^2 + B_4 d_2 + C_4)\right)e^{-32.8326\sigma} \quad \ldots(2.3.3.1)$$

where

$$A_1 = \frac{(0.1624d_1^2 - 2.7457d_1 + 23.4108)}{(d_1^2 + 8.2278d_1 - 56.8407)}$$

$$B_1 = \frac{(0.1068d_1^2 - 4.3025d_1 + 1.4353)}{(d_1^2 + 21.8861d_1 + 120.6147)}$$

$$C_1 = \frac{(0.1501d_1^2 - 3.0585d_1 + 21.4697)}{(d_1^2 + 13.7482d_1 - 81.9105)}$$

$$A_2 = \frac{(3.1286d_1^2 + 137.6073d_1 + 2819.3353)}{(d_1^2 - 65.8905d_1 - 292.3834)}$$

$$A_3 = \frac{(0.4049d_1^2 - 1.7505d_1 + 17.3948)}{(d_1^2 + 5.2993d_1 - 31.5516)}$$

$$A_4 = \frac{(0.3491d_1^2 - 3.8381d_1 - 18.0069)}{(d_1^2 + 5.0328d_1 + 6.133)}$$

$$B_4 = \frac{(-4.8654d_1^2 + 43.5682d_1 + 1501.0384)}{(d_1^2 + 8.7869d_1 - 20.9173)}$$

$$C_4 = \frac{(1853446.2044d_1^2 + 41835454.8844d_1 + 727975409)}{(d_1^2 + 53165.68d_1 + 607854.8058)}$$

The expression for characteristic impedance can be written as:

$$Z_o = e^{\left(0.135\left(s/(s+2w)\right)+0.1f+1.29\sigma+\frac{0.01\beta}{k_o}+0.1266\right)} \quad \ldots(2.3.3.2)$$

The simulated and calculated values are shown in Fig. 2.3.3.2 (a) and (b).

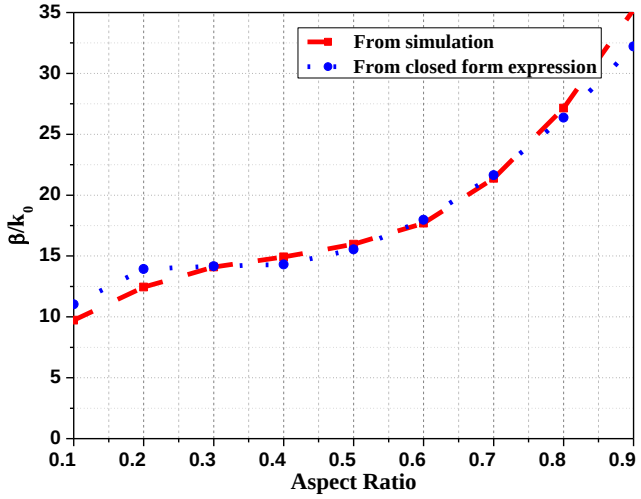

(a)

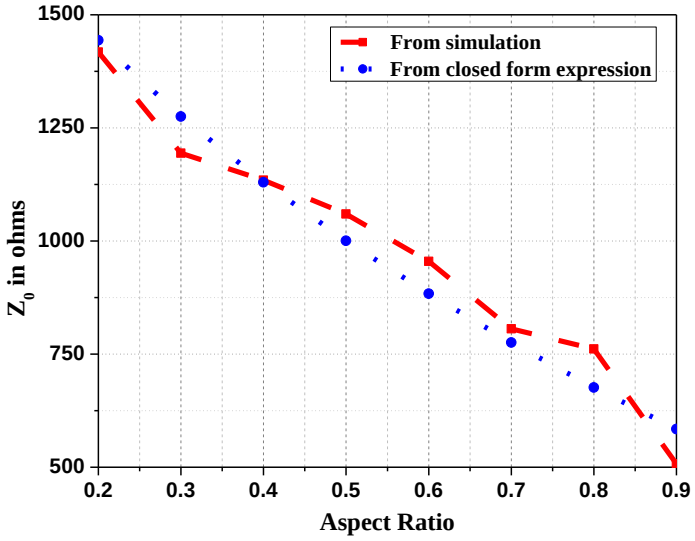

(b)

Fig. 2.3.3.2 (a), (b). Plot of β/k_0 and Z_0 obtained from closed form expression and simulation.

The data in form of tables 2.3.3.1 to 2.3.3.22 have been presented in appendix for the GCPW structure, which shows the change in values of characteristic impedance, Z_0 with frequency (f) in THz relative to the aspect ratio (AR) at different values of strip width, s for odd and even modes.

2.3.4 Graphene backed graphene plasmonic coplanar waveguide (GB-GPCPW): Next, GB-GPCPW has been shown in Fig. 2.3.4.1 [51], where the ground is a thin layer of graphene and the various structure values considered are: $t_1=t_2=10$ nm, h=40 nm, d =20 nm. The boundary conditions have been assumed to be PML.

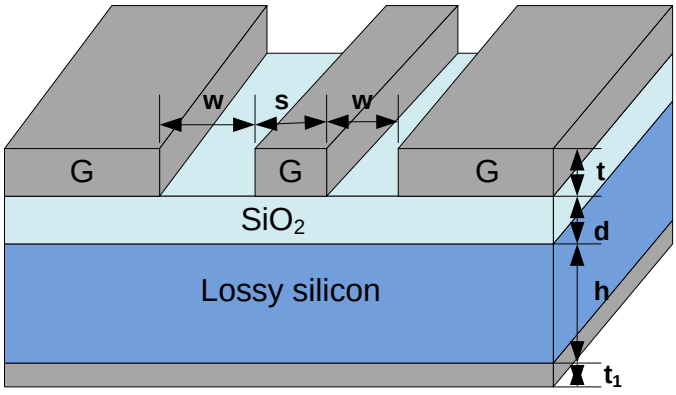

Fig. 2.3.4.1. Plot of Graphene backed graphene plasmonic coplanar waveguide (GB-GCPW).

For the GB-GPCPW structure shown in Fig. 2.3.4.1, the characteristic impedances (odd and even modes) is shown in Fig. 2.3.4.2 (a) and (b). The characteristic impedances for coplanar waveguide

structure are calculated neglecting the effect of substrate. The gap widths are taken from w=10 nm to w=50 nm. The normalized attenuation constant, phase constant and propagation lengths have also been shown in Fig. 2.3.4.2 (c), (d) and (e).

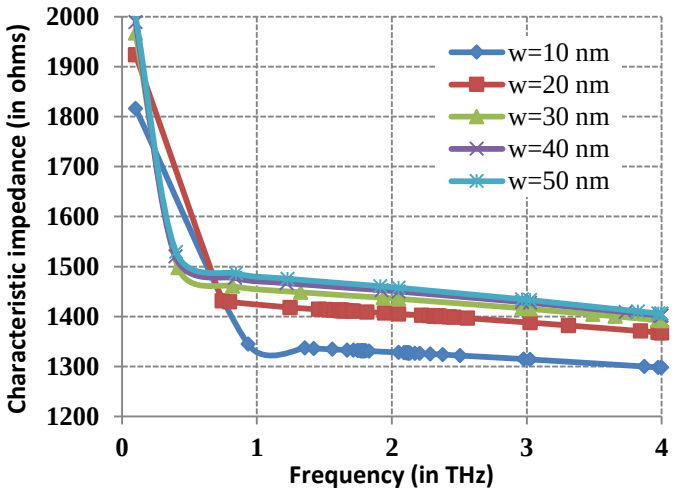

(a)

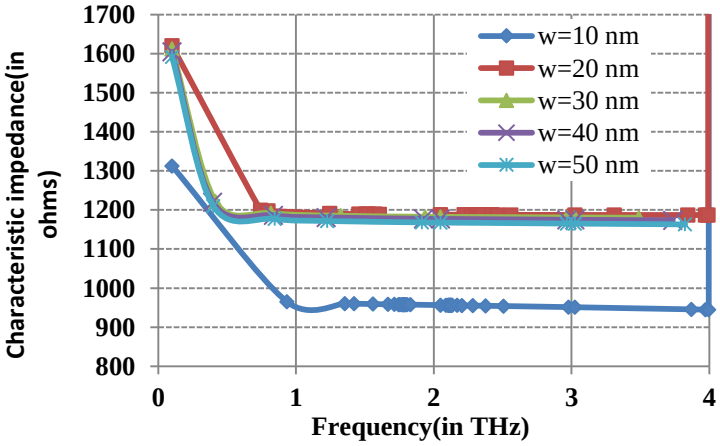

(b)

Fig. 2.3.4.2. (a), (b) Plots of Z_0 for even and odd modes of GB-GPCPW.

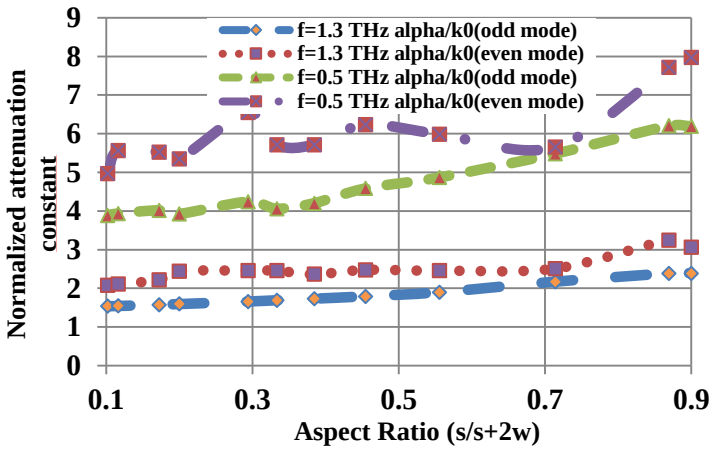

(c)

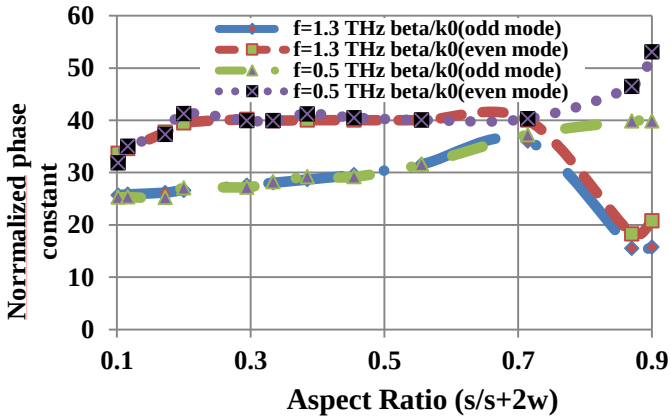

(d)

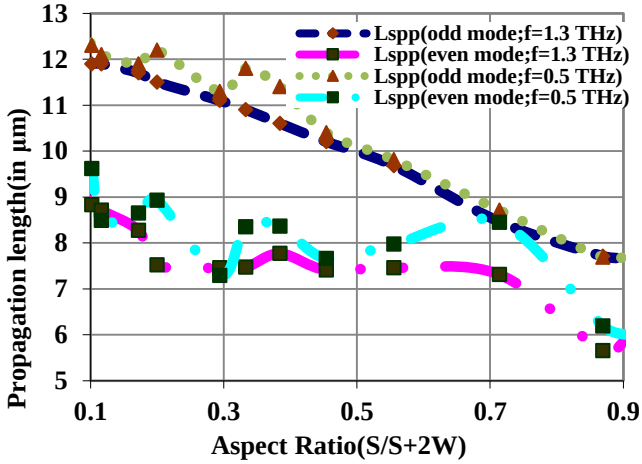

(e)

Fig. 2.3.4.2. (c), (d) and (e) Plots of α/k_0, β/k_0 and L_{spp} for even and odd modes of GB-GPCPW.

The curve fitting equations can be used similarly for the evaluation of normalized propagation constant and characteristic impedance.

2.4 Graphene CPW based discontinuities:

Now, the graphene CPW based discontinuity structures have been discussed. In order to analyze these structures, firstly, we have obtained their S-parameters using e.m. simulation tools and afterwards, an equivalent circuit have been devised using these calculated s-parameter values. In microwave circuits, number of discontinuities have been observed to date. They can be represented by their lumped-equivalents with their device dimensions independent of substrate thickness. Here, the field occurs largely in the spacing between the conductors with some deviation of their characteristic values. Substantially large number of methods have been utilized to study the coplanar waveguide discontinuities. The THz integrated circuits based on coplanar waveguide transmission lines may have discontinuities in the CPW. When the geometry of the graphene strip changes abruptly, these discontinuities in GCPW arise. The design of the millimeter wave ICs require a high degree of accuracy, so it is mandatory to characterize these discontinuities. The discontinuities can be characterized through their lumped equivalent circuits, their sizes being smaller than the wavelengths. These discontinuity structures have been represented in Fig. 2.4.1(a), (b) and (c) and their lumped equivalent models have been shown in Fig. 2.4.1(d), (e) and (f).

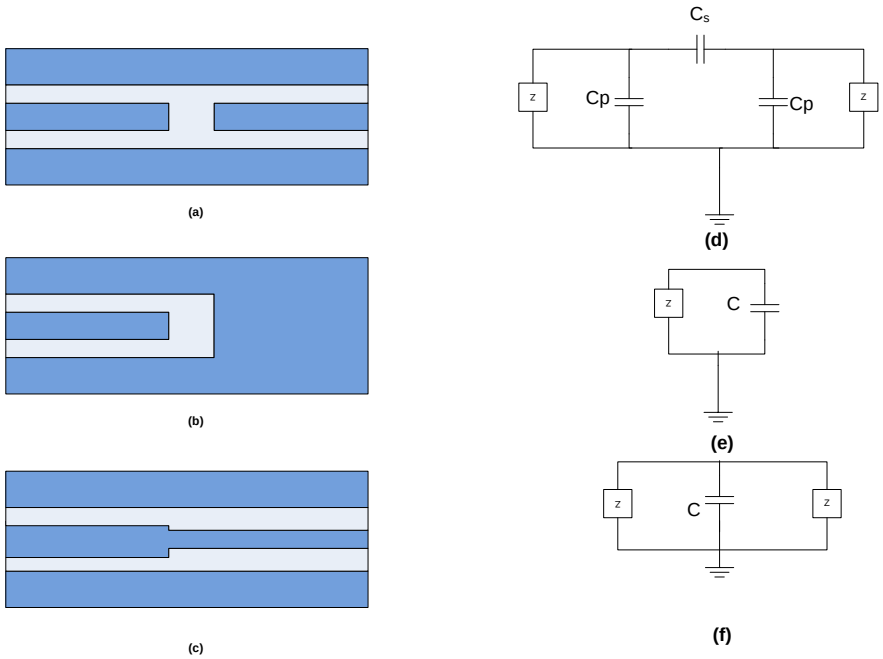

Fig. 2.4.1 Discontinuities in GCPW. **(a)** gap. **(b)** Open. **(c)** Step and lumped models of **(d)** gap **(e)** Open **(f)** Step discontinuities.

2.4.1 Series gap discontinuity

First, the series gap discontinuity has been studied and analyzed as shown in Fig. 2.4.1(a). There is a small gap in the centre conductor of GCPW resulting in a symmetrical geometry of the strip conductors on both sides. The field lines occur in between the open end of the line and ground plane. This results in a parallel capacitance, C_p and a series capacitance, C_s between the open ends. The various values for the gap discontinuity are considered to be t=10 nm, h=40 nm, d=20 nm and g=50 nm and the derived lumped parameters model has been shown in Fig. 2.4.2(a). Here, the capacitances, C_s and C_p are not dependent on the varying gap width as shown in Fig. 2.4.2(b).

2.4.2 Open-end discontinuity

In the open type of discontinuity structure, the strip of graphene acting as conductor ends in an abrupt manner after certain width as presented in Fig. 2.4.1 (b). It should ideally reflect the entire incident light. However, some reflections occur after this open-end when observed practically. These results in fringing field developed at the open section of the discontinuity structure denoted by capacitances, C_s and C_p in the lumped parameter circuit as denoted in Fig. 2.4.2(c). Also, the physical edge length vary because of this capacitance as depicted in Fig. 2.4.2(d) with respect to frequency.

2.4.3 Step discontinuity

The stepped-type discontinuity structure, as shown in Fig. 2.4.1(c), gives a step change in the strip width across the structure. The electric and magnetic field varies at the discontinuity due to the sudden increase in current density from narrow to wide conductor. Also, the fringing field intensifies at the end of the wide graphene strip. The capacitance, C_p varies as shown in Fig. 2.4.2(e). The plot for variation in physical edge length vs. aspect ratio is presented in Fig. 2.4.2(f).

A few more discontinuities like bends, notch, T-junction have also been analyzed with their S-parameters.

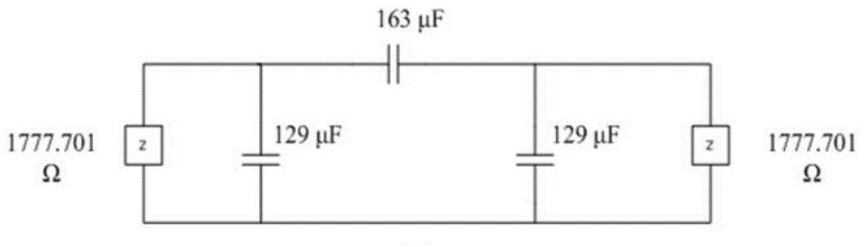

Fig. 2.4.2 (a) Circuit equivalent model for gap type of discontinuity.

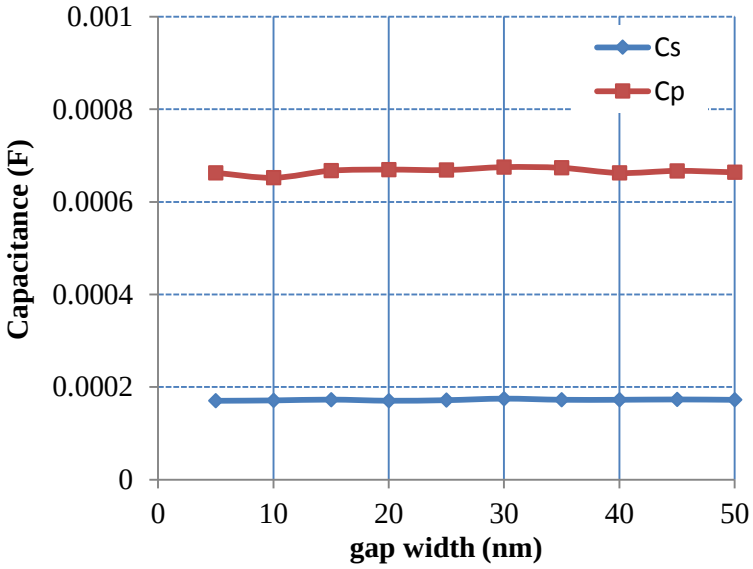

Fig. 2.4.2 (b) Plots for variation of capacitances developed in series and parallel with respect to gap width, g.

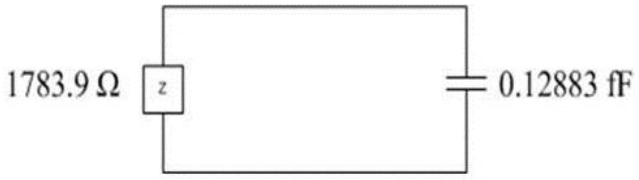

Fig. 2.4.2 (c) Circuit model for open type of discontinuity.

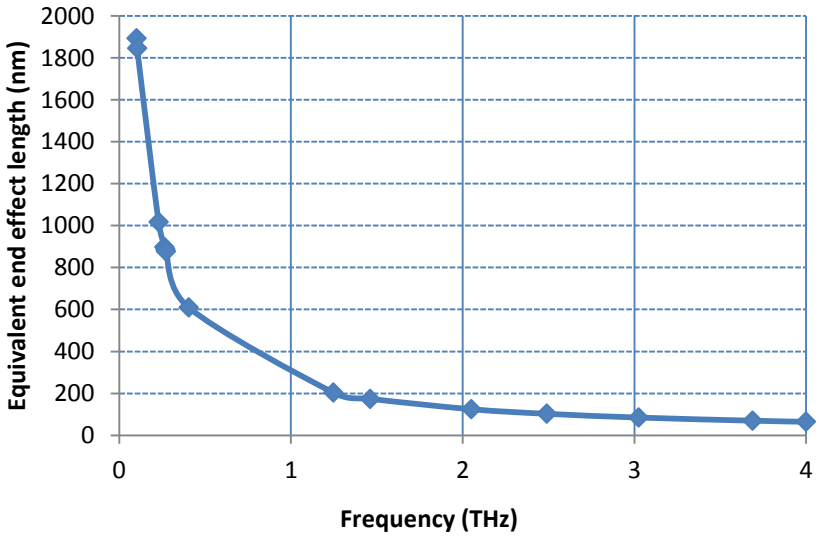

Fig. 2.4.2 (d) Plot of physical edge length vs frequency.

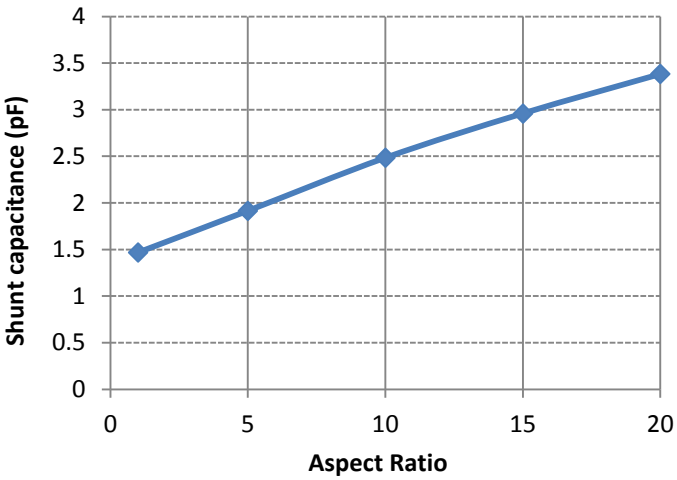

Fig. 2.4.2 (e) Plot of shunt capacitance vs aspect ratio.

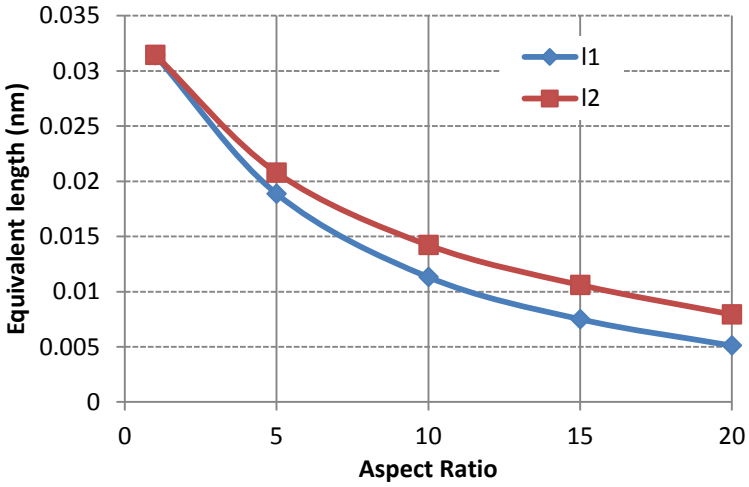

Fig. 2.4.2 (f) Plot of effective physical length vs aspect ratio.

2.4.4 Analysis

The S-parameters of the discontinuity structures have been simulated. Using these S-parameters, the lumped equivalent models may be derived. As shown in Fig. 2.4.4.1(a-f), the reflection and transmission coefficients of series-gap, open-end, step, bend, notch, T-junction have been plotted. Here, it has been considered that the thickness of graphene layer has been taken as 0.5 nm, thickness of lossy silicon substrate 40 nm, thickness of silicon dioxide layer 10 nm.

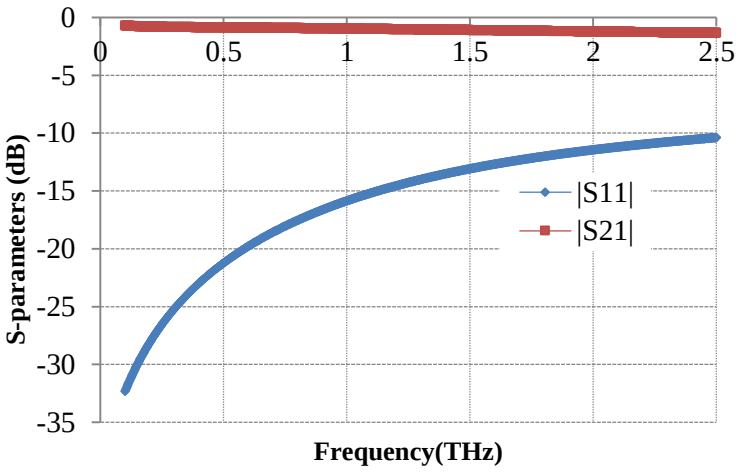

Fig. 2.4.4.1 (a) S-parameters for series gap discontinuity.

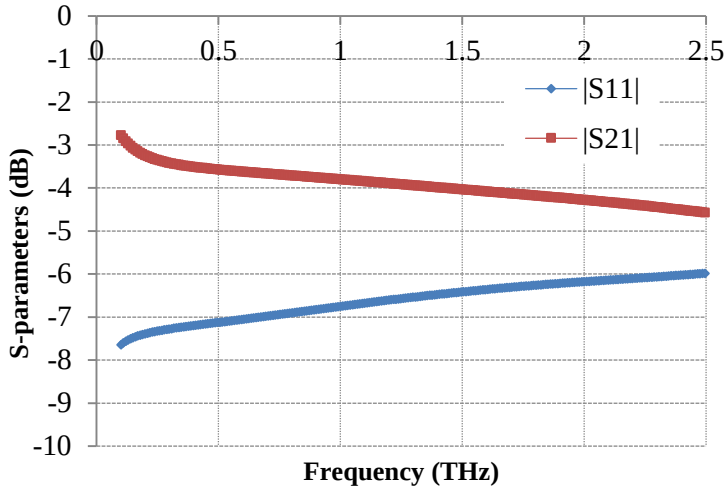

Fig. 2.4.4.1 (b) S-parameters for open-end discontinuity.

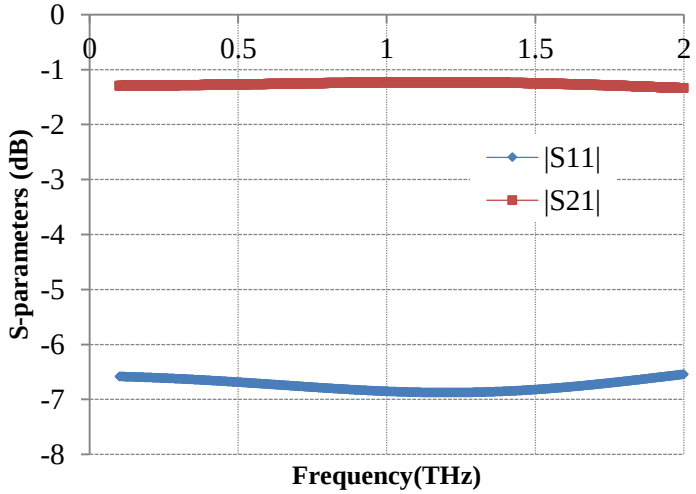

Fig. 2.4.4.1 (c) S-parameters for step discontinuity.

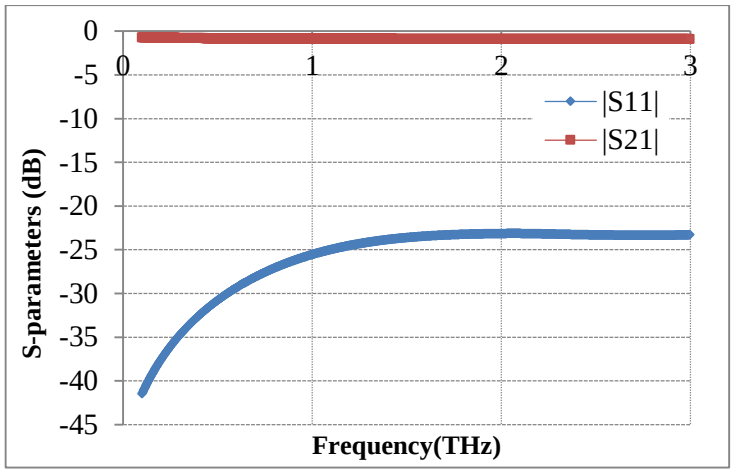

Fig. 2.4.4.1 (d) S-parameters for bend discontinuity.

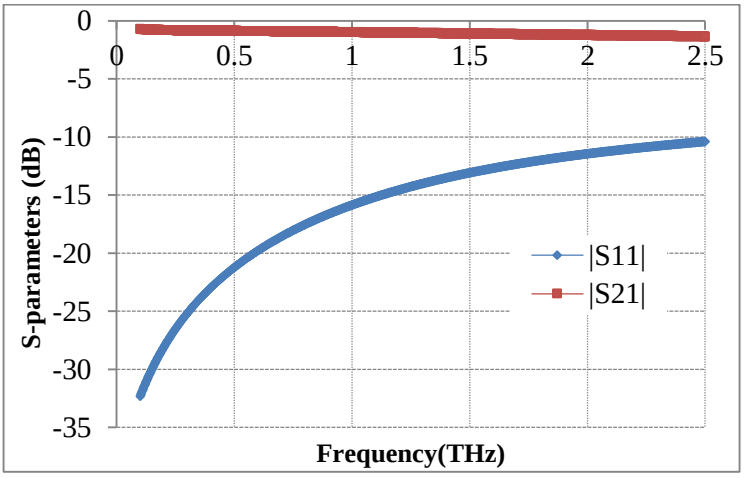

Fig. 2.4.4.1 (e) S-parameters for notch discontinuity.

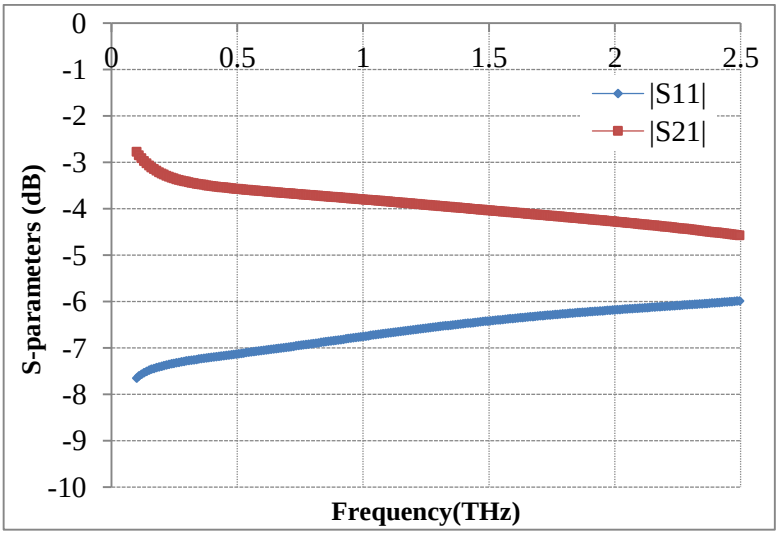

Fig. 2.4.4.1 (f) S-parameters for T-junction discontinuity.

These discontinuities are inevitable because of electrical or mechanical transitions from one medium to another for example a coax-to-microstrip transition or a junction between two waveguides. Even though discontinuity effect is undesired but it is significant enough to mandate their characterization. These discontinuities may be introduced knowingly into the circuit for completion of certain electrical functions like filter circuits or stubs in microstrip line or reactive diaphragms in waveguide). Although a transmission line discontinuity can be converted to its lumped equivalent circuit, the equivalent circuit may be either a T- or π-equivalent circuit or series or shunt combinations depending on the type of discontinuity. After the characterization of the discontinuity structure, its effect can be added in the analysis of the transmission line.

2.5 CONCLUSION

Equivalent transmission line parameters of graphene plasmonic waveguide and its several variants such as nanostrip, coplanar, conductor backed coplanar waveguide and suspended nanostrip waveguide have been described in detail. These have been shown in Table 2.5.1. The simulation model has been validated from the literature survey on the existing structures. The values for propagation constant, β is greater for GPNSW than metal NSW. As compared to regular metal conductor, tunability can be achieved in graphene CPW. The even and odd mode characteristics have been analyzed for the graphene CPW and their field distributions have been shown. RF equivalent models have been evaluated and they give different port impedances from the S-parameter values. These parameters are important for designing integrated circuits discussed in the next chapter.

Table 2.5.1. Graphene plasmonic structures and their parameters.

Structure	α/k_0	β/k_0	References
Graphene nanostrip waveguide	0.377	25	[52]
Graphene nanoribbon based nanostrip waveguide	1	35	[53]
Graphene coplanar waveguide	1	60	[52]
Graphene nanoribbon based coplanar waveguide	6	30	[54]
Graphene conductor backed coplanar waveguide	2	40	[52]
Graphene suspended nanostrip waveguide	1	20	[52]
Microwave coplanar waveguide	--	1.55	[46]

REFERENCES

[1] J. A. Dionne, L. A. Sweatlock, H. A. Atwater, and A. Polman, "Planar metal plasmon waveguides: Frequency-dependent dispersion, propagation, localization, and loss beyond the free electron model," *Phys. Rev. B - Condens. Matter Mater. Phys.*, vol. 72, no. 7, pp. 1-11, Aug. 2005.

[2] R. Zia, M. D. Selker, and M. L. Brongersma, "Leaky and bound modes of surface plasmon waveguides," *Phys. Rev. B -Condens. Matter Mater. Phys.*, vol. 71, no. 16, pp. 1-9, Apr. 2005.

[3] G. Veronis and S. Fan, "Bends and splitters in metal-dielectric-metal subwavelength plasmonic waveguides," *Appl. Phys. Lett.*, vol. 87, no. 13, pp. 131102 (1-3), Sep. 2005.

[4] G. Veronis and S. Fan, "Guided subwavelength plasmonic mode supported by a slot in a thin metal film," *Opt. Lett.*, vol. 30, no. 24, pp. 3359-3361, Dec.2005.

[5] J. A. Dionne, L. A. Sweatlock, H. A. Atwater, and A. Polman, "Plasmon slot waveguides: Towards chip-scale propagation with subwavelength-scale localization," *Phys. Rev. B - Condens. Matter Mater. Phys.*, vol. 73, no. 3, pp. 1-9, Jan. 2006.

[6] E. D. Palik, Handbook of optical constants. *Academic Press,* 1985.

[7] E. Kretschmann, "Reflection and transmission of light by a rough surface, including results for surface-plasmon effects," *J. Opt. Soc. Am.*, vol. 65, no. 2, pp. 313-324, Feb. 1975.

[8] P. B. Johnson and R. W. Christy, "Optical constants of the noble metals," Phys. Rev. B, vol. 6, no. 12, pp. 4370-4379, Dec. 1972.

[9] D. Sarid, "Long-range surface-plasma waves on very thin metal films," *Phys. Rev. Lett.,* vol. 47, no. 26, pp. 1927-1930, Dec. 1981.

[10] P. Berini, "Plasmon - polariton modes guided by a metal of finite width," *Opt. Lett.*, vol. 24, no. 15, pp. 1011-1013, Aug. 1999.

[11] S. A. Maier, "Plasmonics: metal nanostructures for subwavelength photonic devices," *IEEE J. Sel. Top. Quantum Electron.*, vol. 12, no. 6, pp. 1214–1220, Nov. 2006.

[12] C. Huebner and K. Kupfer, "Modelling of electromagnetic wave propagation along transmission lines in inhomogeneous media," *Meas. Sci. Technol.*, vol. 18, no. 4, pp. 1147-1154, Feb. 2007.

[13] J. Chen, G. A. Smolyakov, S. R. J. Brueck, and K. J. Malloy, "Surface plasmon modes of finite , planar , metal-insulator-metal plasmonic waveguides," *Opt. Exp*., vol. 16, no. 19, pp. 14902-14909, Sep. 2008.

[14] B. G. Ghamsari and A. H. Majedi, "Terahertz transmission lines based on surface waves in plasmonic waveguides," *J. Appl. Phys.*, vol. 104, no. 8, pp. 0831081-10, Oct. 2008.

[15] G. Veronis, S. E. Kocabas, D. A. B. Miller, and S. Fan, "Modeling of plasmonic waveguide components and networks," *J. Comput. Theor. Nanosci.*, vol. 6, no. 8, pp. 1808-1826, Aug. 2009.

[16] S. Rakheja and A. Naeemi, "On physical limits and challenges of graphene nanoribbons as interconnects for all-spin logic," *Nanoelectronic Device Applications Handbook, James Morris and Krzysztof Inieweski (Eds.), CRC Press*, June 2013.

[17] S. Rakheja and P. Sengupta, "Graphene nanoribbon plasmonic waveguides: fundamental limits and device implications," *Device Research Conference (DRC)*, June 2014.

[18] S. Rakheja, "Engineering Plasmons in Graphene Nanostructures in THz Frequencies: Compact Modeling and Performance Analysis for On-chip Interconnects," *The International Conference on Simulation of Semiconductor Processes and Devices (SISPAD)*, Sept. 2015.

[19] A. N. Grigorenko, M. Polini and K. S. Novoselov, "Graphene plasmonics – optics in flatland," pp. 1-19, 2013.

[20] A. K. Geim and K. S. Novoselov, "The rise of graphene," *Nat. Mater.*, vol. 6, pp. 183–191, 2007.

[21] X. Gu, I. T. Lin and J. M. Liu, "Extremely confined terahertz surface plasmon-polaritons in graphene-metal structures," *Appl. Phys. Lett.*, vol. 103, pp. 071103 1-4, Aug. 2013.

[22] K. S. Novoselov, Z. Jiang, Y. Zhang, S. V. Morozov, H. L. Stormer, U. Zeitler, J. C. Maan, G. S. Boebinger, P. Kim, and A. K. Geim, "Room-Temperature Quantum Hall Effect in Graphene," *Science*, vol. 315, no. 2000, pp. 1379–1379, 2007.

[23] Y. Zhang, Y. Tan, H. L. Stormer and P. Kim, "Experimental observation of quantum Hall-effect and Berry's phase in graphene," *Nature*, vol. 438, pp. 201-204, Nov. 2005.

[24] K. I. Mikhail, "Graphene : carbon in two dimensions," *Mater. Today*, vol. 10, no. 1, pp. 20–27, Feb. 2007.

[25] H. Hajian, A. Soltani-Vala, M. Kalafi and P. T. Leung, "Surface plasmons of a graphene parallel plate waveguide bounded by Kerr-type nonlinear media," *J. Appl. Phys.*, vol. 115, pp. 083104 1-7, Feb. 2014.

[26] D. Correas-Serrano, J. S. Gomez-Diaz, J. Perruisseau-Carrier and A. Álvarez-Melcón, "Spatially dispersive graphene single and parallel plate waveguides: Analysis and circuit model," *IEEE Trans. Microw. Theory Tech.*, vol. 61, no. 12, pp. 4333–4344, Dec. 2013.

[27] A. Malekabadi, S. A. Charlebois and D. Deslandes, "Parallel plate waveguide with anisotropic graphene plates: Effect of electric and magnetic biases," *J. Appl. Phys.*, vol. 113, pp. 113708 1-9, March 2013.

[28] H. Hajian, A. Soltani-Vala and M. Kalafi, "Optimizing terahertz surface plasmons of a monolayer graphene and a graphene parallel plate waveguide using one-dimensional photonic crystal," *J. Appl. Phys.*, vol. 114, no. 2013, pp. 0331021-8, July 2013.

[29] J. S. Gomez-Diaz, J. R. Mosig and J. Perruisseau-Carrier, "Effect of Spatial Dispersion on Surface Waves Propagating Along Graphene Sheets," *IEEE Trans. Antennas Propag.*, vol. 61, no. 7, pp. 3589-3596, July 2013.

[30] G. W. Hanson, "Dyadic Green's functions and guided surface waves for a surface conductivity model of graphene," *J. Appl. Phys.*, vol. 103, pp. 1–8, March 2008.

[31] T. Stauber, N. M. R. Peres and A. K. Geim, "Optical conductivity of graphene in the visible region of the spectrum," *Phys. Rev. B - Condens. Matter Mater. Phys.*, vol. 78, pp. 1–8, Aug. 2008.

[32] F. T. Vasko and V. Ryzhii, "Voltage and temperature dependencies of conductivity in gated graphene," *Phys. Rev. B - Condens. Matter Mater. Phys.*, vol. 76, pp. 1–5, Dec. 2007.

[33] L. A. Falkovsky and S. S. Pershoguba, "Optical far-infrared properties of a graphene monolayer and multilayer," *Phys. Rev. B - Condens. Matter Mater. Phys.*, vol. 76, no. 3, pp. 1–4, Feb. 2013.

[34] D. Svintsov, V. Vyurkov, V. Ryzhii and T. Otsuji, "Voltage-controlled surface plasmon-polaritons in double graphene layer structures," *J. Appl. Phys.*, vol. 113, no. 4, pp. 053701 1-5, Feb. 2013.

[35] P. I. Buslaev, I. V. Iorsh, I. V. Shadrivov, P. A. Belov, and Y. S. Kivshar, "Plasmons in waveguide structures formed by two graphene layers," *JETP Lett.*, vol. 97, no. 9, pp. 535–539, April 2013.

[36] G. W. Hanson, "Quasi-transverse electromagnetic modes supported by a graphene parallel-plate waveguide," *J. Appl. Phys.*, vol. 104, pp. 1–5, Oct. 2008.

[37] R. N. Simons and G. E. Ponchak, "Modeling of some coplanar waveguide discontinuities," *IEEE Trans. Microw. Theory Tech.*, vol. 36, pp. 1796–1803, May 1988.

[38] C. J. Railton, and T. Rozzi, "The Rigorous Analysis of Cascaded Step Discontinuities in Microstrip," *IEEE Trans. Microw. Theory Tech.*, vol. 36, no. 7, pp. 1177–1185, July 1988.

[39] M. Naghed and I. Wolff, "Equivalent capacitances of coplanar waveguide discontinuities and interdigitated capacitors using a three-dimensional finite difference method," *IEEE Trans. Microw. Theory Tech*, vol. 38, no. 12, pp. 1808–1815, Dec. 1990.

[40] N. I. Dib, L. P. B. Katehi, G. E. Ponchak and R. N. Simons, "Theoretical and experimental characterization of Coplanar waveguide discontinuities for filter applications," *IEEE Trans. Microw. Theory Tech.*, vol. 39, no. 5, pp. 873-882, May 1991.

[41] L. Wu and H. Chang, "Analysis of Dispersion and Series Gap Discontinuity in Shielded Suspended Striplines with Substrate Mounting Grooves," *IEEE Trans. Microw. Theory Tech.*, vol. 40, no. 2, pp. 279-284, Feb. 1992.

[42] J. Martel, R. R. Boix and M. Horno, "Equivalent circuits for MIS microstrip discontinuities," *IEEE Microw. Guid. Wave Lett.*, vol. 3, no. 11, pp. 408–410, 1993.

[43] T. L. Willke and S. S. Gearhart, "Novel Micromachined Liga Microstrip Transmission Lines and Filters," *IEEE MTT-S International Microwave Symposium Digest*, pp. 5–8, 1996.

[44] C. W. Chiu and R. Wu, "Capacitance computation for CPW discontinuities with finite metallization thickness by hybrid finite-element method," *IEEE Trans. Microw. Theory Tech.*, vol. 45, no. 4, pp. 498–504, April 1997.

[45] M. Prasad, A. S. Gaur, V. K. Sharma and N. P. Pathak, "Modeling of Multilayer Suspended Microstrip Line and its Discontinuities on CMOS Grade Silicon Substrate for Millimeter Wave Integrated Circuit Applications," *Int. J. Infrared Milli Waves*, vol. 29, pp. 1123-1135, Aug. 2008.

[46] S. K. Koul, A. Kumbhat and A. Basu, "Micromachined conductor backed coplanar waveguides for millimeter wave circuit application," *Indian Journal of Pure & Applied Physics*, vol. 45, pp. 336-344, Feb. 2007.

[47] C. J. Docherty and M. B. Johnston, "Terahertz properties of graphene," *J. Infrared, Millimeter, Terahertz Waves*, vol. 33, pp. 797–815, June 2012.

[48] E. Kymakis, E. Stratakis, M. M. Stylianakis, E. Koudoumas and C. Fotakis, "Spin coated graphene films as the transparent electrode in organic photovoltaic devices," *Thin solid films*, vol. 520, pp. 1238-1241, 2011.

[49] F. Y. Ban, S. R. Majid, N. M. Huang and H. N. Lim, "Graphene oxide and its electrochemical performance," *Int. J. Electrochem. Sci.*, vol. 7, pp. 4345 - 4351, May 2012.

[50] N. Joshi and N. P. Pathak, "Graphene plasmonics based terahertz integrated circuits," Book chapter in springer, *communicated*.

[51] N. Joshi and N. P. Pathak, "Graphene Backed Graphene Plasmonic Coplanar Waveguide (GB-GPCPW) for Terahertz Integrated Circuit Applications ," *IEEE Proceedings of Applied Electromagnetics Conference*, Dec. 2015.

[52] N. Joshi and N. P. Pathak, "Modeling of graphene coplanar waveguide and its discontinuities for THz integrated circuit applications," *Plasmonics,* vol. 12, no. 5, pp. 1-10, Nov. 2016.

[53] R. Araneo, G. Lovat and P. Burghignoli, "Graphene nanostrip lines: Dispersion and attenuation analysis", *IEEE 16th workshop on Signal and Power integrity*, May 2012.

[54] R. Araneo, P. Burghignoli, G. Lovat and G. W. Hanson, "Modal propagation and cross-talk analysis in coupled Graphene nanoribbons", *IEEE trans. Electromagn. Compat.*, vol. 57, no. 4, pp. 726-733, Aug. 2015.

Design and Simulation of Graphene Plasmonic Waveguide Based Resonators and Filters

3.1 Introduction

This chapter describes the graphene plasmonic stepped width resonator (GPSWR), graphene plasmonic waveguide based ring resonators, GPSWR based band pass filters by using graphene plasmonic uniform width resonator (GPUWR). GPSWR has been analyzed in terms of their electrical parameters by using commercially available electromagnetic full-wave simulation software. A GPSWR has been designed and simulated to obtain its transmission and reflection coefficients. The concurrent dual-pass band characteristics of SWR can be used in the design of dual band photonic integrated circuits (PICs). GPSWR based dual band filters are more compact with reduced space and power requirements in PICs. This concept can be extended to design several other components such as multiplexers/diplexers, directional couplers/branch line couplers and antenna discussed in following chapters.

3.2 Graphene Plasmonic Waveguide Resonators

Planar plasmonic waveguide resonators [1] are classified into two categories. They are MIM and IMI waveguide based resonators. Resonators behave as filters, which can accept or reject specific wavelengths from an input signal in single or dual band. The transmission line resonators have low Q-values as compared to waveguide-based resonators; but they possess simple structure, small size and wide applicability to various nanophotonic circuits [1-4]. The graphene plasmonic waveguide based resonators in cylindrical and rectangular shapes can be used at THz frequencies in the design of filters and other tuning elements.

The graphene plasmonic waveguide [2] based resonators can be excited in various resonant modes. The basic characteristics of such resonators are their resonant frequencies, Q-factors and field distributions. These properties must be known for the lowest order resonant mode and a few higher order modes to allow proper selection of a mode that can be used for a particular application. The mode should be excited by a suitable coupling mechanism. The field distribution provides the information to devise proper technique for suppression of unwanted mode, which may interfere with the desired mode.

3.2.1 Graphene Plasmonic Waveguide Uniform Width Resonators

Graphene plasmonic uniform width resonator (GPUWR) can be described by following definition i.e., the transmission line having uniform characteristic impedance using an electrical length of π radians and these kind of transmission line resonators are simply called as GPUWR and are shown in Fig. 3.2.1.1. Because of their simple structure and easy design features, transmission line resonators are widely used in the conventional filters [3-6]. However, practical GPUWRs have a number of disadvantages like limited design parameters because of their simple design.

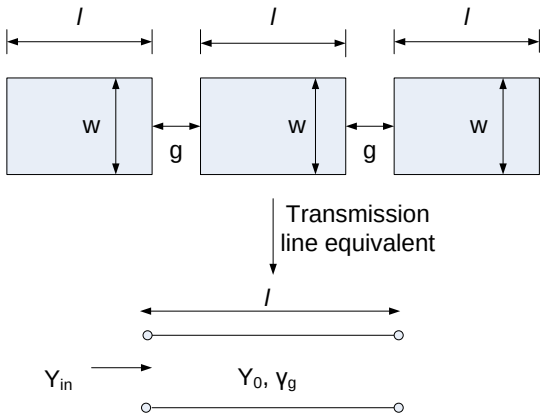

Fig. 3.2.1.1 Graphene plasmonic uniform-width-resonator and its transmission-equivalent.

A transmission line with an open end circuit with length of $\lambda_g/2$ or multiples of $\lambda_g/2$ at a frequency $\omega = \omega_0$ behaves as a parallel LC type resonator. The basic characteristics of transmission line resonators have been described in several text books such as D. M. Pozar [7].

The input admittance (Y_{in}) of the open circuit with the length l is

$$Y_{in} = Y_0 \tanh(\gamma_g l)$$

$$= Y_0 \frac{\tanh \alpha_g l + j \tan \beta_g l}{1 + j \tan \beta_g l \tanh \alpha_g l} \tag{3.1}$$

where Y_0 is output admittance, γ_g, α_g and β_g are guided propagation constant, attenuation constant and phase constant.

Fig. 3.2.1.2 Design of resonator. Here, G denotes graphene and A stands for air.

As seen earlier in chapter 2, graphene [8-14] can be used to design plasmonic waveguides [15-18] and discontinuities. This can also be extended to design resonators and filters. With the use of the series-gap discontinuity, a graphene based resonator can be modeled and simulated as shown in Fig. 3.2.1.2. The design dimensions are considered to be same as the series-gap discontinuity described in section 2.4.1. Its S-parameters have been simulated and analyzed with various values of gap widths, g_1 and g_2 as shown in Fig. 3.2.1.3. The S_{11} and S_{21} values show a little change with the increase or decrease in gap widths.

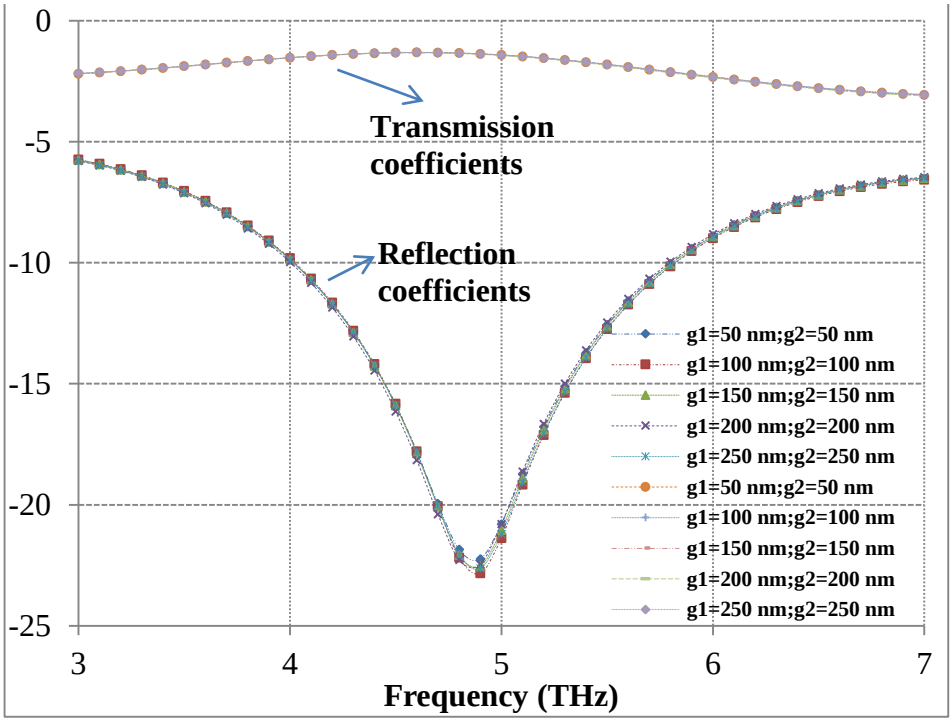

Fig. 3.2.1.3 Transmission and reflection coefficients of resonator.

3.2.2 Graphene Plasmonic Ring resonators

The device comprises of two graphene plasmonic nanostrip waveguides (GPNSW) and a ring resonator [19-22]. Its schematic diagram has been shown in Fig. 3.2.2.1(a-b). Here, the ring resonator consists of graphene and the remaining material is a material with variable refractive index like skin (thermal conductivity, $\rho = 0.293$ W/K/m), or bone (conductivity, $\rho = 0.41$ W/K/m)

or air. In case, the structure is placed underground, the graphene CSRR has been enclosed by upper layer of sand. The 2D simulations have been performed in order to reduce the computational burden, with the widths of the input and output waveguides taken as d. Also, the coupling distance between SPPs waveguide and the ring resonator is g. Next, the values of d, l, g, a, b, c, x and x' are set to be 40 nm, 250 nm, 10 nm, 10 nm, 10 nm, 10 nm, 10 nm and 10 nm, respectively. The following equation gives the resonance condition for the ring resonator [23]:

$$\frac{J_n'(kR_m)}{J_n'(kR_{inner})} - \frac{N_n'(kR_m)}{N_n'(kR_{inner})} = 0 \qquad \text{.....(3.2.2.1)}$$

Here, k is wave vector and J_n' and N_n' are the derivatives to the Bessel functions of the first kind and second kind of order n, respectively.

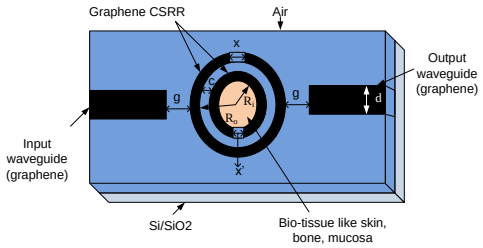

(a)

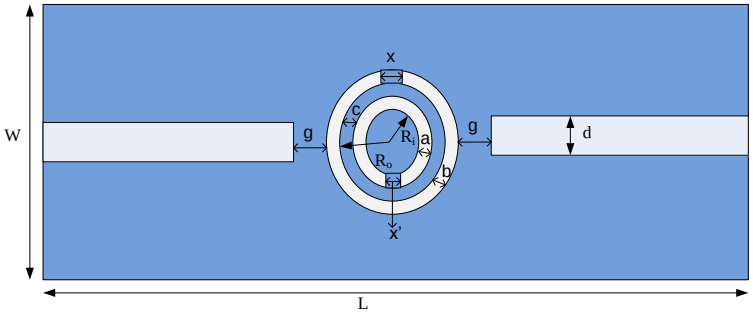

(b)

Fig. 3.2.2.1 Structure schematic of two waveguides with a ring resonator. **(a)** Three dimensional structure. **(b)** Top view of the structure.

Fig. 3.2.2.2 shows the transmission spectrum in which the insulating medium is air. The surface plasmon polaritons (SPPs) travel along the structure with a few reonance peaks in the spectrum. The peaks of the transmission coefficient is plotted with frequency (in THz) in Fig. 3.2.2.2.

The width of the slits are taken as 40 nm. The coupling distance between the waveguides and the ring resonator is set as 10 nm and radius of the ring as 100 nm. Here, three transmission peaks are visible in the spectrum as in Fig. 3.2.2.2. These peaks show different transmittance values at

different wavelengths of λ = 26000 nm, 34800 nm and 41900 nm. Next, the field distribution at different frequencies *f* = 6.6157 THz and *f* = 7.9625 THz is shown in Fig. 3.2.2.3.

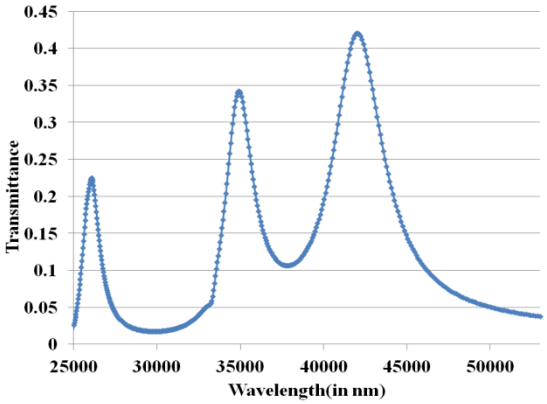

Fig. 3.2.2.2 Transmission spectrum of graphene based stucture.

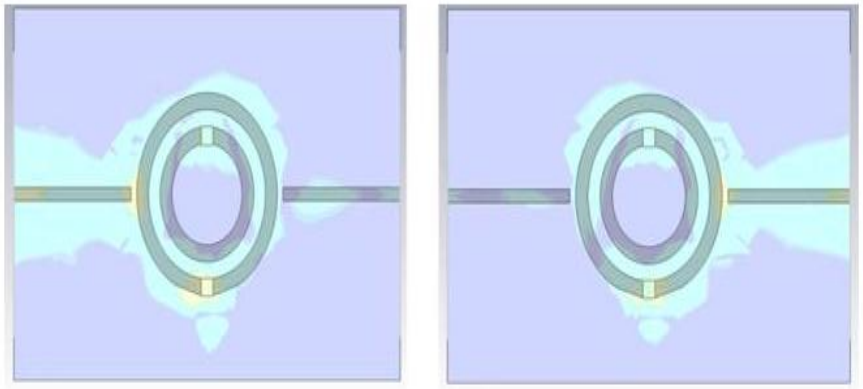

(a)

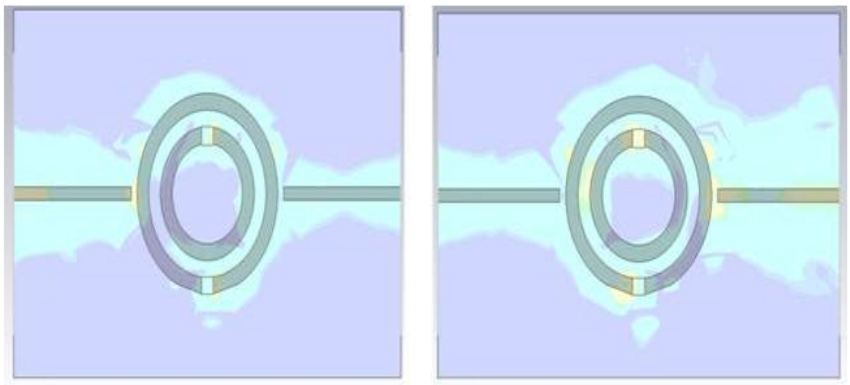

(b)

Fig. 3.2.2.3 Field distribution at different frequencies (a) *f*=6.6157 THz and (b) *f*=7.9625 THz.

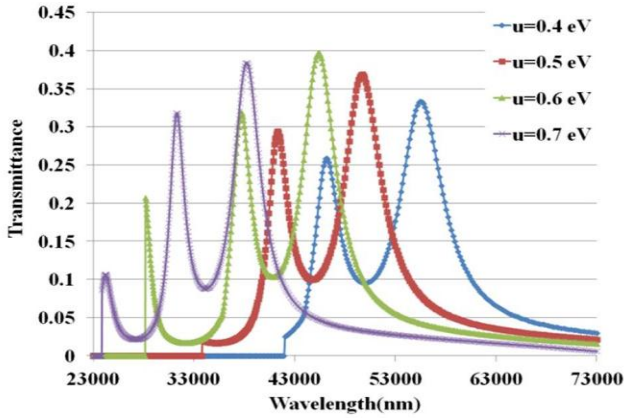

Fig. 3.2.2.4 Transmittance spectrum of graphene based structure for different values of chemical potential.

In Fig. 3.2.2.4 and Fig. 3.2.2.5, the peaks of the transmission spectrum of the graphene based structure are observed with respect to the different values of chemical potential of graphene. As the chemical potential increases, the values shift more to the left side showing an increase in the losses. The values of chemical potential vary from 0.4 to 0.7 eV.

Additionally, the transmission spectrum is shown in relation to the temperature showing no changes in the peaks with increase in temperature showing its relative insensitivity to temperature in Fig. 3.2.2.6. Next, the transmission spectrum is observed with the change in structural parameters. Fig. 3.2.2.7 shows the peaks of the transmission spectrum with the change in chemical potential at different values of radius of ring resonator, r=450 nm, 500 nm, 550 nm and 600 nm. The radius of the ring changes the position of the peaks of the transmission spectrum. As the radius increases, the frequencies decrease and consequently, the wavelengths become larger with the increase in the radius. Also, the transmission loss increases.

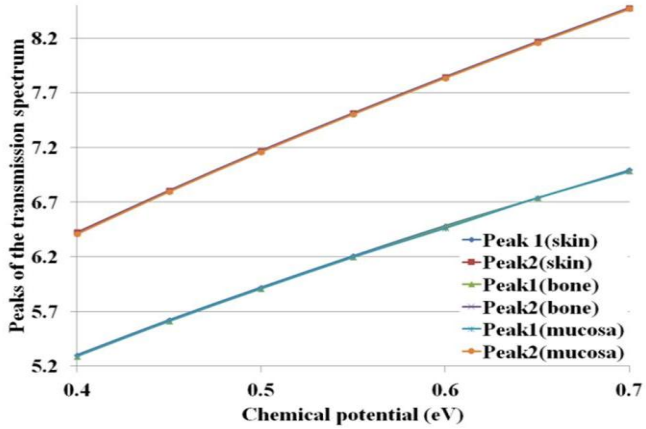

Fig. 3.2.2.5 Transmission spectrum of graphene based structure with respect to chemical potential.

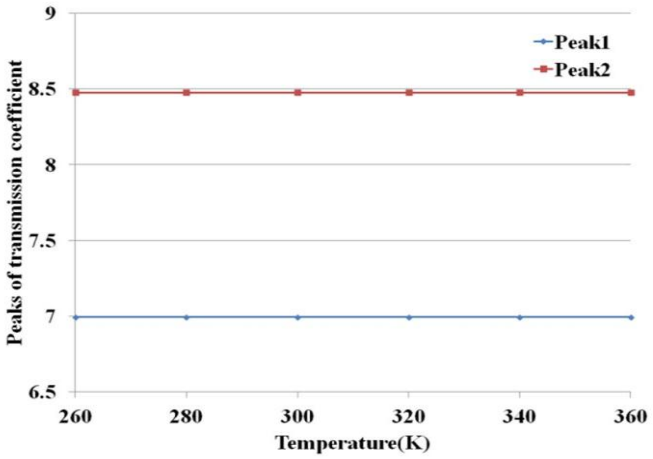

Fig. 3.2.2.6 Transmission spectrum of graphene based structure with respect to temperature (K).

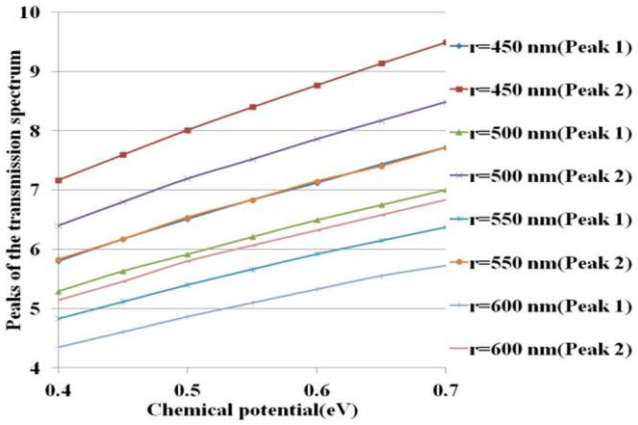

Fig. 3.2.2.7 Peaks of the transmission spectrum with chemical potential at different radii of ring resonator.

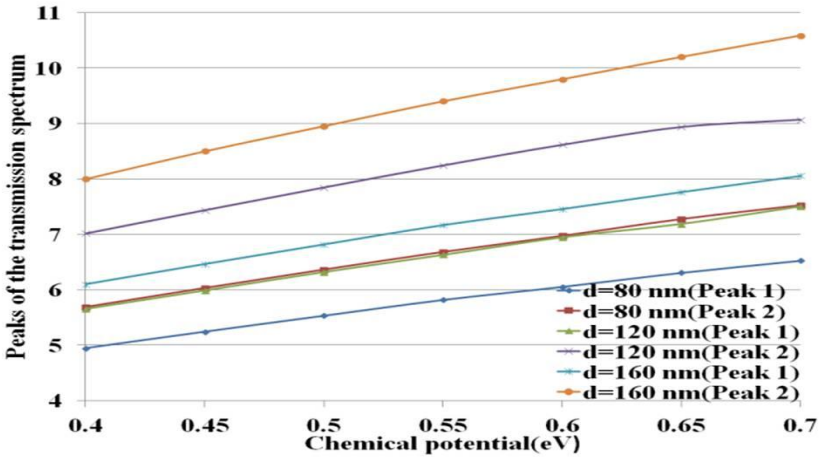

Fig. 3.2.2.8 Peaks of the transmission spectrum with chemical potential at different widths of input and output waveguides of graphene based split ring resonator.

Fig. 3.2.2.8 displays the transmission spectrum of the structure at different widths of input and output microstrip waveguides. The different values of the widths are assumed to be d=80 nm, d=120 nm and, d=160 nm. As the widths increase, the frequency peaks increase showing smaller

values of wavelengths with increase in the widths of the waveguides. Fig. 3.2.2.9 shows the transmission spectrum of the structure for different radius of ring resonator at specified values of chemical potential and widths of the input and output waveguides. Thus, the sensitivity of the structure can be improved by increasing the radius of the ring resonator or decreasing the widths of the input and output waveguides at the cost of increase in transmission loss.

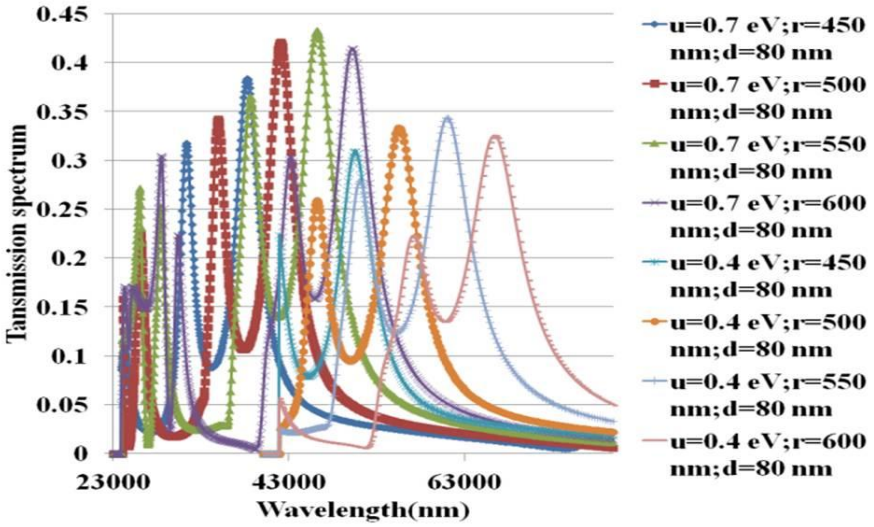

Fig. 3.2.2.9 Transmission spectrum with wavelength for different values of radius of ring resonator at specified values of chemical potential and widths.

3.2.3 Graphene plasmonic modified ring resonators

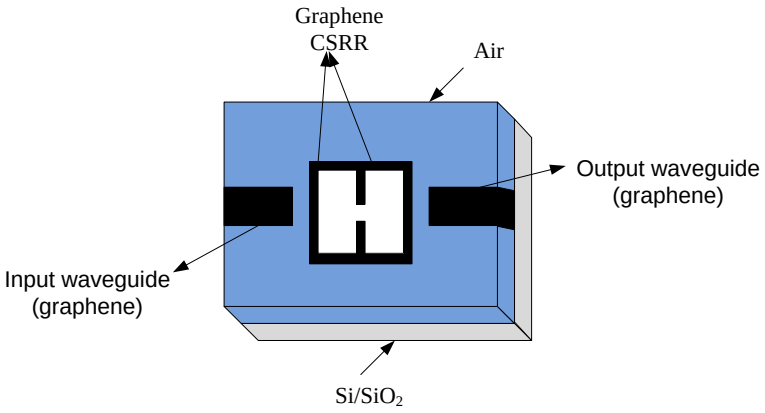

(a)

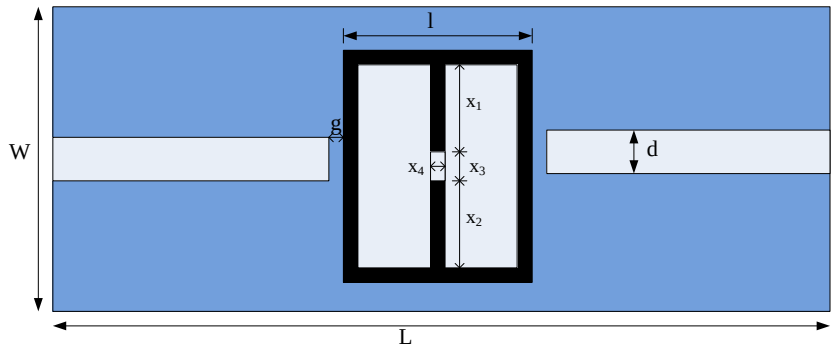

(b)

Fig. 3.2.3.1 Schematic diagram of graphene based CSRR. (a) 3-D view. (b) Top view.

Now, moving further from simple ring resonator structure to the complex structures, modified ring resonator structures have been presented in Fig. 3.2.3.1. First graphene plasmonic SRR consists of two nanostrip lines and a modified ring resonator [24-30]. The ring resonator comprises of graphene and the remaining material on the substrate is filled with the material under sensing. In the design, the width of the input and output nanostrip waveguide *d* is set to be 40 nm, and the material is opted to be graphene. The side length of the modified ring is *l* as shown in Fig. 3.2.3.1(b). Also, the coupling distance between SPPs waveguide and the ring resonator is *g*. For general cases, the values of *d*, *l*, *g*, x_1, x_2, x_3 and x_4 are set to be 40 nm, 250 nm, 10 nm, 90 nm, 90 nm, 50 nm and 10 nm, respectively. Another kind of modified ring resonator structure with its characteristics has been mentioned in Fig. 3.2.3.2. In this structure, the value of y_1 is 100 nm. Next, the material parameters, dielectric permittivity and dielectric permeability, *ε(eps)* and *μ(mu)* can be obtained from the S-parameters of the graphene based SPPs waveguide sensor designed as shown in Fig. 3.2.3.2(c). The fact can be validated by the following expressions [31]:

$$n = \frac{1}{kd}\cos^{-1}\left[\frac{1}{S21}(1 - S_{11}^2 + S_{21}^2)\right] \quad ..(3.2.3.1)$$

$$z = \sqrt{\frac{(1+S11)^2 - S_{21}^2}{(1-S11)^2 - S_{21}^2}} \quad ..(3.2.3.2)$$

$$\varepsilon = n/z \text{ and } \mu = nz \quad ..(3.2.3.3)$$

Here, *n* is refractive index, *z* is wave impedance, *k* is wave vector, and *d* is width of the ring. It is analyzed further in the next chapter.

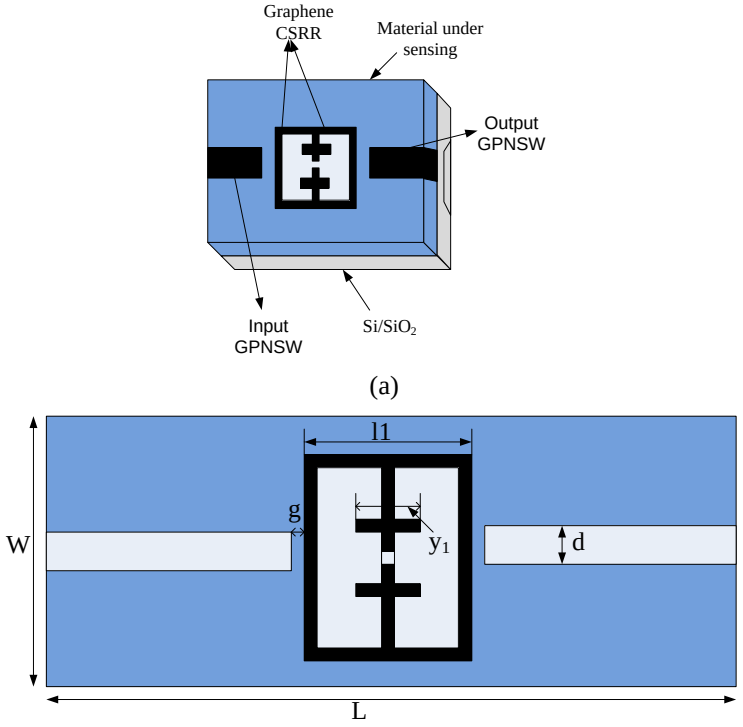

Fig. 3.2.3.2 Structure schematic of two waveguides with a modified ring resonator. (a) Three-dimensional view (b) Top view of the structure showing graphene based CSRR. (c) Dielectric permittivity and permeability of graphene based CSRR.

3.3. General Procedure for the Design of Plasmonic Waveguide Filters

The general steps for the band-pass-filter design have been summarized in the following procedure. It illustrates a fundamental approach needed for the analysis of generalized plasmonic filters, which have been described later.

Step 1: The basic filter properties have been specified to obtain an approximately required frequency response. It includes bandwidth (B.W.), centre frequency of the pass-band, insertion

loss, source and load impedances, and attenuation at a specific frequency in stop band. These specifications lead to derivation of a particular filter, which may be Butterworth, Chebyshev or Bessel's filter. Here, a Chebyshev Filter has been illustrated.

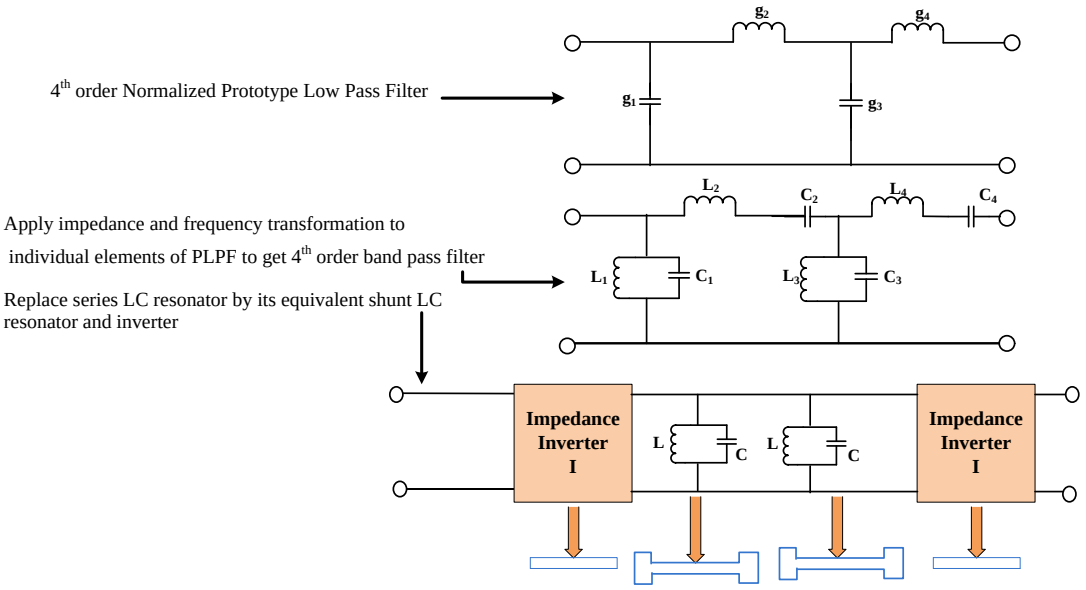

Fig. 3.3.1 Steps used in the design of 4th order band-pass filter.

Step 2: The frequency transformation is applied to obtain prototype low pass filter (PLPF) as described in Fig. 3.3.1. Relative comparisons have been performed with the obtained Chebyshev response in PLPF plane. The minimum order of the filter in our case is selected to be n = 4. A 4th order prototype filter has been synthesized as ladder network with the elemental values, g_1, g_2, g_3 and g_4 (shown in Table 3.3.1). Here, g_1 is capacitor, g_2 is inductor, g_3 is capacitor and g_4 is inductor. The description is given in detail in [7].

Step 3: It can be converted to an equivalent circuit comprising inductances and capacitances in parallel and series. This gives the lumped equivalent circuit model.

Step 4: Instead of lumped components, distributed parameters with transmission line sections have been presented at THz frequencies. The series LC resonator has been transformed into parallel LC reconator circuit and impedance inverter [7].

Table 3.3.1 Element values for Equal-Ripple Low-Pass Filter Prototypes (g_0 = 1,ω_c = 1, N = 1 to 0.5 dB ripple [7])

Normalized Element Values for Low Pass Filter Prototype (Chebyshev response with 0.5 dB ripple)											
Filter Order(N)	g_1	g_2	g_3	g_4	g_5	g_6	g_7	g_8	g_9	g_{10}	g_{11}
1	1.0000										
2	0.7071	1.9841									
3	1.5963	1.0967	1.5963	1.0000							
4	1.6703	1.1926	2.3661	0.8419	1.9841						
5	1.7058	1.2296	2.5408	1.2296	1.7058	1.0000					
6	1.7254	1.2479	2.6064	1.3137	2.4758	0.8696	1.9841				
7	1.7372	1.2583	2.6381	1.3444	2.6381	1.2583	1.7372	1.0000			
8	1.7451	1.2647	2.6564	1.3590	2.6964	1.3389	2.5093	0.8796	1.9841		
9	1.7504	1.2690	2.6678	1.3673	2.7239	1.3673	2.6678	1.2690	1.7504	1.0000	
10	1.7543	1.2721	2.6754	1.3725	2.7392	1.3806	2.7231	1.3485	2.5239	0.8842	1.9841

Step 5: Next, GPSWR replaces shunt LC resonator and plasmonic waveguide sections are used in place of impedance inverters.

Step 6: The final layout of the filter has been shown in Fig. 3.3.1. Its simulated results give transmission (S_{21}) and reflection (S_{11}) characteristics using full wave simulations.

3.4 Graphene plasmonic band-pass filters

Now, the proposed graphene plasmonic band-pass filters have been described. In the first design, concurrent dual-band operation has been explained and in the next design, ultra broadband operation has been included.

3.4.1 Model structure and theoretical analysis

In the band-pass filter design as shown in Fig. 3.4.1.1, two SIRs have been coupled and connected to input and output microstrip feed waveguides [31-32]. The entire structure is designed on SiO_2 substrate with lossy silicon at the bottom. The dimensions of the substrate are taken to be 480 nm x

2500 nm x 90 nm. The structure designed over the substrate is graphene layer with thickness 0.5 nm.

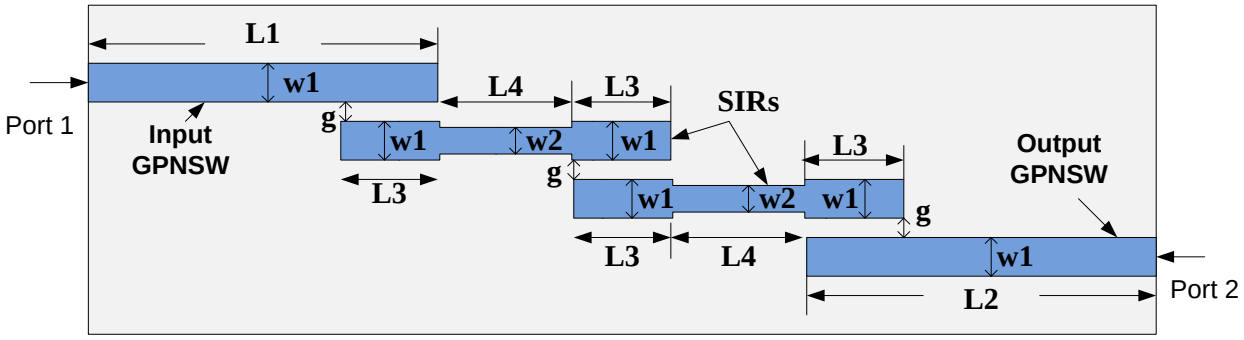

Fig. 3.4.1.1 Design of wide-band graphene based band-pass filter, where L1=1300 nm, L2=1500 nm, L3=200 nm, L4=200 nm, w1=50 nm, w2=40 nm.

3.4.2 Synthesis and simulated results of graphene based band-pass filter

The graphene based band-pass filter has been designed using the following specifications.

Filter specifications:

- Center frequency = 4.6594 THz
- B.W. = 0.7192 THz
- Attenuation passband = 3 dB
- Source and load impedances: 770 Ω
- Insertion loss: 4 dB
- Attenuation stop band = 20 dB

Using the simulation software ADS, we get the transmission equivalent circuit as shown in Fig. 3.4.2.1(a).

The simulated results of the graphene based band-pass filter have been presented in Fig. 3.4.2.1(b) and compared with theoretical results. In the plots, a wideband has been observed ranging from 4.2648 THz to 4.8939 THz. The transmission coefficient represents a constant value at around -4 dB with a ripple of around 1 dB. The filter provides the following features:

- Band-pass range: 4.2648 THz to 4.8939 THz
- Order 4 Butterworth filter
- Ripple: 1 dB

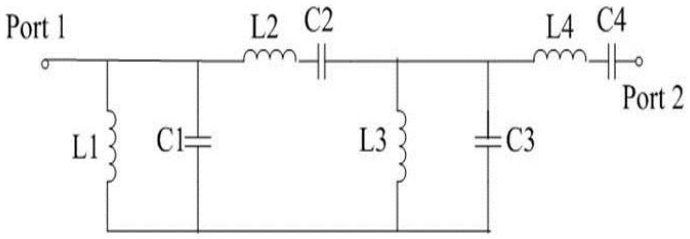

Fig. 3.4.2.1. (a) Graphene based band-pass filter transmission line equivalent.

- L1=5.339287 pH, C1=0.219832 fF;
- L2=314.665199 pH, C2=0.00373015 fF;
- L3=2.211605 pH, C3=0.530722 fF;
- L4=130.338595 pH, C4=0.00900537 fF
- f_p^1, lower passband corner frequency=4.2998 THz
- f_p^2, upper passband corner frequency=5.019 THz
- f_s^1, lower stopband frequency edge=1.6747 THz
- f_s^2, upper stopband frequency edge=5.4339 THz
- Electrical length of SIR: 1.875 m (at 4.5 THz)

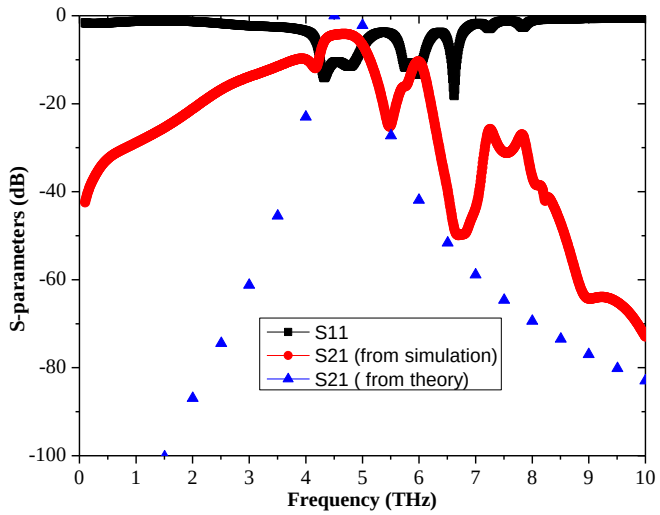

Fig. 3.4.2.1. (b) S-parameters of graphene based ultra wideband band-pass filter.

The same band-pass filter can be used for concurrent dual-band operation as shown in Fig. 3.4.2.2. In the design, two SIRs have been coupled to the input and output microstrip feed waveguides [24-30]. The design is same as the previous band-pass filter, but in this case, the length of the feed line

has been considered to be L1=900 nm. The simulated results of the graphene based band-pass filter have been presented in Fig. 3.4.2.2(b). In the plots, a wideband has been observed ranging from 4.2648 THz to 4.8939 THz. The transmission coefficient represents a constant value at around -0.5 dB with a ripple of around 1 dB.

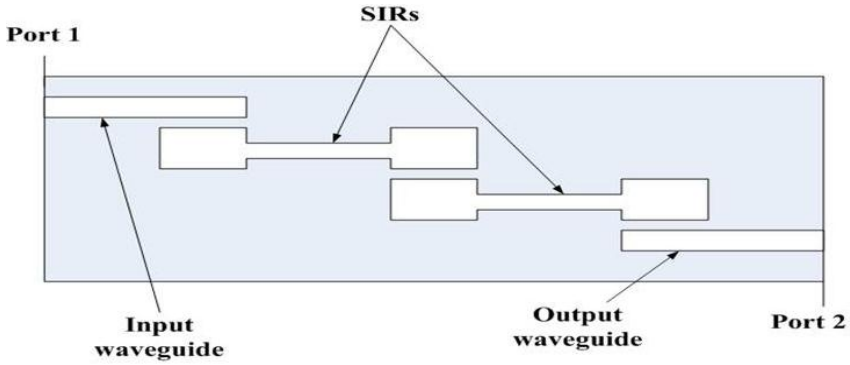

Fig. 3.4.2.2 (a)

Next, the tunability feature has been incorporated in the designed band-pass filter. This feature has been achieved by changing the chemical potential to obtain the structure transmission and reflection coefficients shown in Fig. 3.4.2.3. As the chemical potential changes from 1.0 to 0.8, the band shifts from center frequency 4.5793 THz to 4.088 THz. Similarly, for the values of chemical potential 0.6, 0.4 and 0.2, the band shifts to the frequencies 3.5795, 2.9391 and 2.0686 THz. This variation has been observed among the transmission and reflection coefficients as well. Therefore, tuning can be performed over the entire frequency range by changing the externally applied bias voltage.

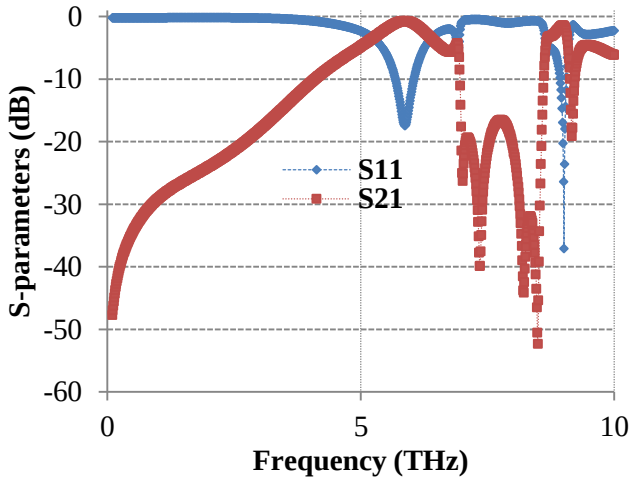

(b)

Fig. 3.4.2.2 (a) Design of concurrent dual-band graphene based band-pass filter. **(b)** S-parameters of designed band-pass filter.

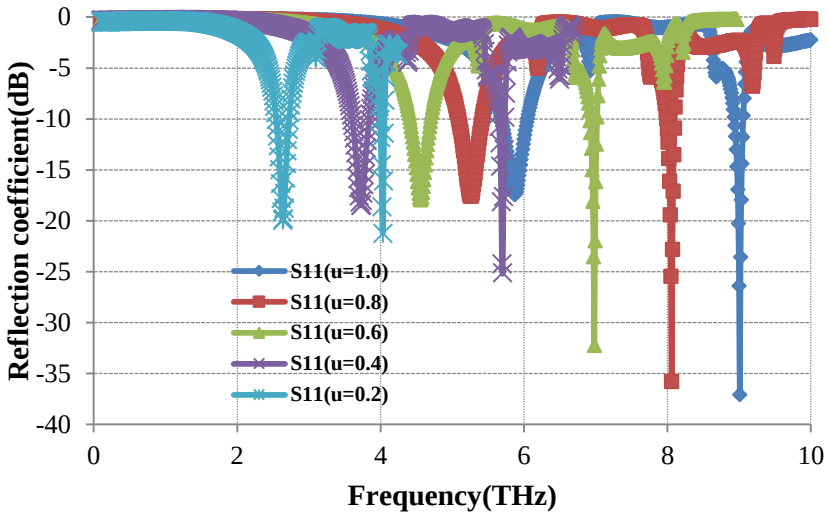

Fig. 3.4.2.3. (a) S11 with frequency in THz at different chemical potentials.

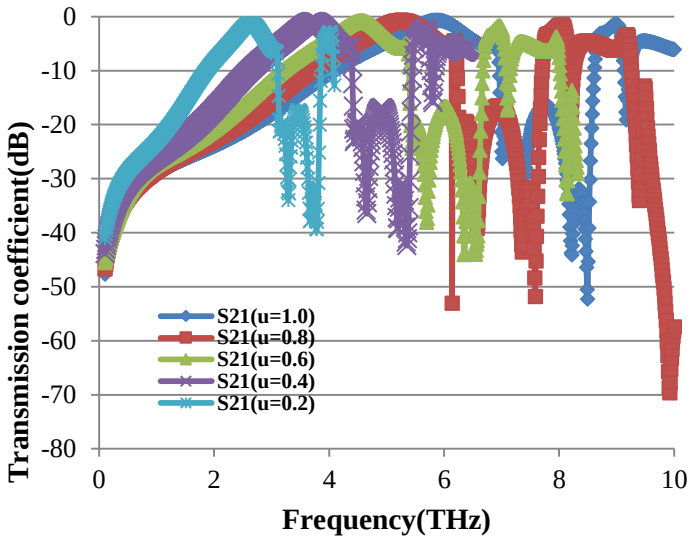

Fig. 3.4.2.3. (b) S21 with frequency in THz at different chemical potentials.

The GPPW leads to the modeling of moderate loss, tunable, and compact THz transmission lines. They can be used for the realization of THz loaded lines for phase shifters (active) and electronic switching devices. The value of graphene chemical potential can be varied in the range -1 eV to 1 eV in the THz frequency range. The chemical potential of single layer of graphene is as follows.

$$\mu_c = \hbar \vartheta_F \sqrt{\frac{\pi C_{ox} V_g}{e}} \qquad \ldots.(3.4.2.1)$$

where $C_{ox}=\varepsilon_{ox}/t_{ox}$ is the gate capacitance, t_{ox} is the gate oxide thickness and V_g, the applied gate voltage. An n^+-doped polysilicon or metal gate positioned behind the oxide, which may be Al_2O_3, SiO_2, or BN results in the tuning of the surface resistance of the graphene layers placed above and below the gate. This allows variation in the characteristic impedance, Z_c of the gate section.

3.5 CONCLUSION

The transmission line characteristics of GPNSW along with the resonant behavior of SWR have been numerically investigated. The pass band characteristics of GPSWR have been found useful in the design of THz integrated circuits. This will make the system more compact and will reduce the space and power requirements. This concept can be extended to design several other components such as power splitters/combiners, couplers and diplexers.

REFERENCES

[1] S. A. Maier, Plasmonics: Fundamentals and applications. *Springer*, 2006.

[2] T. Low and P. Avouris, "Graphene Plasmonics for Terahertz to Mid-Infrared Applications," *ACS*, vol. 8, no. 2, pp. 1086-1101, Jan. 2014.

[3] Kaijun Song and Yong Fan, "Compact Ultra-Wideband Bandpass Filter using Dual-Line Coupling Structure," *IEEE Microw. Wirel. Compon. Lett.*, vol. 19, no. 1, Jan 2009.

[4] Amir Hosseini and Yehia Massoud, "Nanoscale surface plasmon based resonator using rectangular geometry," *Appl. Phys. Lett.*, vol. 90, pp. 1811021-5, April 2007.

[5] Kazuo Tanaka, Tran Trong Minh and Masahiro Tanaka, "Analysis of propagation characteristics in the surface plasmon polariton gap waveguides by method of lines," Opt. Exp., vol. 17, no. 2, Jan. 2009.

[6] Wenjie Feng, Quan Xue, and Wenquan Che, "Compact Dual-Band Bandpass Filter based on Stepped impedance resonators And T-shaped line," 2010 Wiley Periodicals, Microwave Opt. Technol. Lett., vol. 52, no. 12, pp. 2721–2724, Dec. 2010.

[7] D. M. Pozar, *Microwave Engineering*. Wiley Series, 2012.

[8] J. S. Gómez-Díaz and J. Perruisseau-Carrier, "Microwave to THz properties of graphene and potential antenna applications", *Proceedings of ISAP2012, Nagoya, Japan*, pp. 239-2 42, May 2012.

[9] A. N. Grigorenko, M. Polini, and K. S. Novoselov, "Graphene plasmonics – optics in flatland", July 2013

[10] A. K. Geim and K. S. Novoselov, "The rise of graphene.," *Nat. Mater.*, vol. 6, pp. 183–191, Sept. 2007.

[11] X. Gu, I. T. Lin, and J. M. Liu, "Extremely confined terahertz surface plasmon-polaritons in graphene-metal structures," *Appl. Phys. Lett.*, vol. 103, July 2013.

[12] K. S. Novoselov, Z. Jiang, Y. Zhang, S. V. Morozov, H. L. Stormer, U. Zeitler, J. C. Maan, G. S. Boebinger, P. Kim, and A. K. Geim, "Room-Temperature Quantum Hall Effect in Graphene," *Science*, vol. 315, no. 2000, pp. 1379–1379, May 2007.

[13] Y. Zhang, Y. Tan, H. L. Stormer, and P. Kim, "Experimental observation of the Quantum Hall Effect and Berry's phase in Graphene," *Nature*, vol. 438, pp. 201-204, Sept. 2005.

[14] K. Mikhail I, "Graphene : carbon in two dimensions," *Mater. Today*, vol. 10, no. 1, pp. 20–27, Feb. 2007.

[15] H. Hajian, A. Soltani-Vala, M. Kalafi, and P. T. Leung, "Surface plasmons of a graphene parallel plate waveguide bounded by Kerr-type nonlinear media," *J. Appl. Phys.*, vol. 115, Jan. 2014.

[16] D. Correas-Serrano, J. S. Gomez-Diaz, J. Perruisseau-Carrier, and A. Álvarez-Melcón, "Spatially dispersive graphene single and parallel plate waveguides: Analysis and circuit model," *IEEE Trans. Microw. Theory Tech.*, vol. 61, no. 12, pp. 4333–4344, Dec. 2013.

[17] A. Malekabadi, S. A. Charlebois, and D. Deslandes, "Parallel plate waveguide with anisotropic graphene plates: Effect of electric and magnetic biases," *J. Appl. Phys.*, vol. 113, Jan. 2013.

[18] H. Hajian, A. Soltani-Vala, and M. Kalafi, "Optimizing terahertz surface plasmons of a monolayer graphene and a graphene parallel plate waveguide using one-dimensional photonic crystal," *J. Appl. Phys.*, vol. 114, no. 2013, June 2013.

[19] Y. Gao, G. Ren, B. Zhu, L. Huang, H. Li, B. Yin, and S. Jian, "Tunable Plasmonic Filter Based on Graphene Split-Ring," *Plasmonics*, vol. 11, no. 1, pp. 291–296, August 2015.

[20] D. Correas Serrano, J. S. Gomez-Diaz, J. Perruissea-Carrier, and Alvarez-Melcon, "A Graphene-based plasmonic tunable low-pass filters in the THz band," *IEEE T. Nano.*, vol. 13, no. 6, pp. 1145-1153, Nov. 2014.

[21] H. Deng, Y. Yan, and Y. Xu, " Tunable flat-top bandpass filter based on coupled resonators on a graphene sheet ," *IEEE Photonic. Techn. L.*, vol. 27, no. 11, pp. 1161-1164, June 2015.

[22] N. Joshi and N. P. Pathak, "Modeling of graphene coplanar waveguide and its discontinuities for THz integrated circuit applications," *Plasmonics*, pp 1-10, Nov. 2016.

[23] B. Wang and G. P. Wang, "Plasmonic waveguide ring resonator at terahertz frequencies," *Appl. Phys. Lett.*, vol. 89, no. 13, pp. 1–4, Sept. 2006.

[24] T. Wu, Y. Liu, Z. Yu, Y. Peng, C. Shu, and H. He, "The sensing characteristics of plasmonic waveguide with a single defect," *Opt. Commun.*, vol. 323, no. 7, pp. 44–48, April 2014.

[25] J. Wang, W. B. Lu, X. B. Li, X. F. Gu, and Z. G. Dong, "Plasmonic metamaterial based on the complementary split ring resonators using graphene," *J. Phys. D. Appl. Phys.*, vol. 47, no. 32, p. 325102, July 2014.

[26] S. Cakmakyapan, H. Caglayan, and E. Ozbay, "Coupling enhancement of split ring resonators on graphene," *Carbon N. Y.*, vol. 80, no. 1, pp. 351–355, Aug. 2014.

[27] H. J. Chen and K. Di Zhu, "Graphene-based nanoresonator with applications in optical transistor and mass sensing," *Sensors (Switzerland)*, vol. 14, no. 9, pp. 16740–16753, Sept. 2014.

[28] P. Q. Liu, I. J. Luxmoore, S. A. Mikhailov, N. A. Savostianova, F. Valmorra, J. Faist, and G. R. Nash, "Highly tunable hybrid metamaterials employing split-ring resonators strongly coupled to graphene surface plasmons," *Nat. Commun.*, vol. 6, p. 8969, Nov. 2015.

[29] N. Joshi and N. P. Pathak, "Graphene-backed graphene plasmonic coplanar waveguide (GB-GPCPW) for terahertz integrated circuit applications," *IEEE Proceedings of AEMC*, Dec. 2015.

[30] D. R. Smith, D. C. Vier, T. Koschny, and C. M. Soukoulis, "Electromagnetic parameter retrieval from inhomogeneous metamaterials," *Phys. Rev. E*, vol. 71, no. 036617, pp. 1-11, March 2005.

[31] N. Joshi and N. P. Pathak, "Concurrent dual-band tunable graphene based band-pass filter," *ICIIS, Roorkee*, India, Dec., 2016.

[32] N. Joshi and N. P. Pathak, “Compact ultra-wide-band graphene based tunable band-pass filter,” *International Conference on Advanced Functional Materials*, Los Angeles, U.S.A. Aug. 4-6, 2017.

Chapter 4

Design and Simulation of Graphene Plasmonic Waveguide Based Multiplexer and Coupler

4.1 Introduction

The detailed analysis of graphene plasmonic waveguides have been studied in chapter 2. They have been used to design filters and resonators in chapter 3. In this chapter, we will study the use of GPWs for the operation of demultiplexing using wavelength-division-demultiplexer (WDM). Further, a diplexer has been designed using GPSNSW and then, a directional coupler has been designed using GPCPW. Their sensing application has also been studied.

4.2 GPPW for demultiplexing operation

Metallic SRRs have been used from decades to enhance and localize the incident light [1]. Several devices can be designed with the help of SRRs like low-pass filters [2], metamaterials [3], etc. They can also be used to study the photon decay rate [4]. Additionally, the plasmonic demultiplexers for SPPs have been demonstrated for realization of light to show coupling, dispersion and guiding characteristics of SPPs, which can be used for demultiplexing and filtering operations [5]. WDM using MIM plasmonic nanodisk resonators have been proposed and simulated with the help of FDTD based electromagnetic simulations [6]. The WDM based on graphene split ring resonators has been discussed in the subsequent section.

Split ring resonators (SRRs) have been widely used for the purpose of enhancement and localization of incident electromagnetic field in nanoscale integrated circuit applications. The wavelength demultiplexing application is provided with a structure of two graphene nanostrip lines coupled to each other by a ring resonator. The demultiplexing operation in the proposed device depends on the dielectric constant of the surrounding material as well as on the chemical potential of graphene material. The material properties of graphene based CSRR WDM mainly decide the localization of transmission peaks. Here also the variation in chemical potential of graphene provides an efficient tuning of graphene surface plasmons. The applied gate voltage in graphene changes the transmission peaks of SRR structures, and therefore the optical conductivity of monolayer graphene. Subsequently, the demultiplexing characteristics are analyzed with the help of the transmission spectrum at the output

port. The resultant transmittance curves are simulated using CST microwave studio finally providing its demultiplexing results. The curves between the resonance peaks in the transmission spectrum have been plotted. Further, the structural parameters of the device effects on sensitivity have been analyzed to optimize the performance. The transmission properties have been simulated numerically using full wave simulations.

4.2.1 Model structure: The geometry of graphene based plasmonic nanostrip waveguide along with its two-wire transmission line equivalent circuit has been described previously in Fig. 2.2.1.1(a) [7, 8]. The equivalent circuit representation is shown and analyzed in chapter 2 (section 2.2.1). In the full-wave simulations, we have used following parameters to obtain the transmission line characteristics of this waveguide geometry: width of the nanostrip waveguide is w, thickness of silicon dioxide d = 40 nm, h=100 nm, $t=t_0$=0.5nm and chemical potential μ of graphene strip: varied from 0.4 to 0.7. The device comprises of two graphene plasmonic nanostrip waveguides (GPNSW) and a ring resonator. Its schematic diagram has been shown previously in Fig. 3.2.3.1.

4.2.2 Transmission characteristics of CSRR: The transmission characteristics of the graphene based CSRR presented in the previous section has been shown in Fig. 4.2.2.1. The surface plasmonic resonances occur at some fixed frequencies in these characteristics. These transmission resonances have been shown with respect to the propagating frequencies. Here, the widths of input and output GPNSWs, d have been considered to be 40 nm. Also, the split-ring radius is considered as 100 nm with the value of the coupling distance, g between the waveguides and the ring resonator set to be 10 nm. There are three transmission resonances available in the frequency response curve shown in Fig. 4.2.2.1. These transmission peaks are observed at 3.3 THz, 8 THz and 9.5 THz.

Next, the transmission spectra of graphene based CSRR has been observed further with respect to various design parameters like chemical potential of graphene, refractive index of material, etc. [1]. Firstly, the transmission resonances have been obtained with different values of chemical potential of graphene as shown in Fig. 4.2.2.2. These resonances travel towards right with the increase in the values of applied chemical potential resulting in sufficient increase in transmission. These values of chemical potential have been varied from 0.4 to 0.7 eV. The transmission characteristics shows a linear variation with chemical potential.

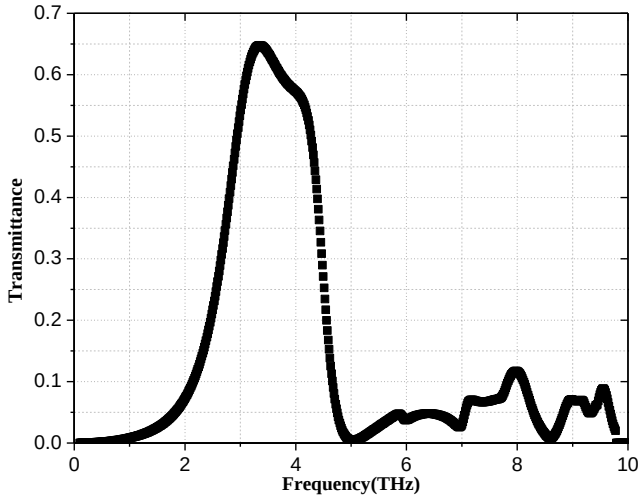

Fig. 4.2.2.1 Transmission spectrum of graphene based CSRR structure.

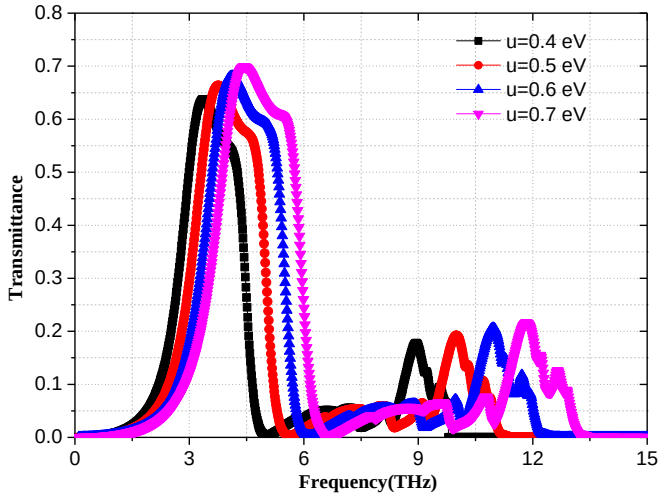

Fig. 4.2.2.2 Transmittance spectrum of graphene based CSRR structure for different values of chemical potential.

Now, the impact of variation in values of structural parameters have been observed on the transmission characteristics of the graphene based CSRR structure. Firstly, the transmission peaks have been observed at different values of side lengths of ring resonator, l1=200 nm, 225 nm, 250 nm and 275 nm as shown in Fig. 4.2.2.3. There is a relative change in the position of the peaks of the transmission spectrum with change in values of the side lengths of the modified ring. With the increase in side lengths, the transmission resonances are obtained at lower values of frequencies and consequently, higher values of wavelengths. As is clearly observed from the figure, as the transmission values decrease, the transmission loss also increases.

Fig. 4.2.2.4 shows the transmission spectrum of the structure at different widths of input and output GPNSWs, considering different values of the widths to be d=10 nm, d=20 nm, d=30 nm, and d=40 nm. With the increase in widths, the transmission resonances are obtained at higher values of frequencies

and consequently, lower values of wavelengths. Thus, the transmission peaks can be tuned at desired frequencies or wavelengths, increasing the radius of the ring resonator or decreasing the widths of the input and output waveguides, simultaneously suffering with the increase in transmission loss. Fig. 4.2.2.5 shows the transmission spectrum of the structure for different lengths, *l* of ring resonator. The spectra is obtained at specified values of chemical potential and widths of the input and output waveguides.

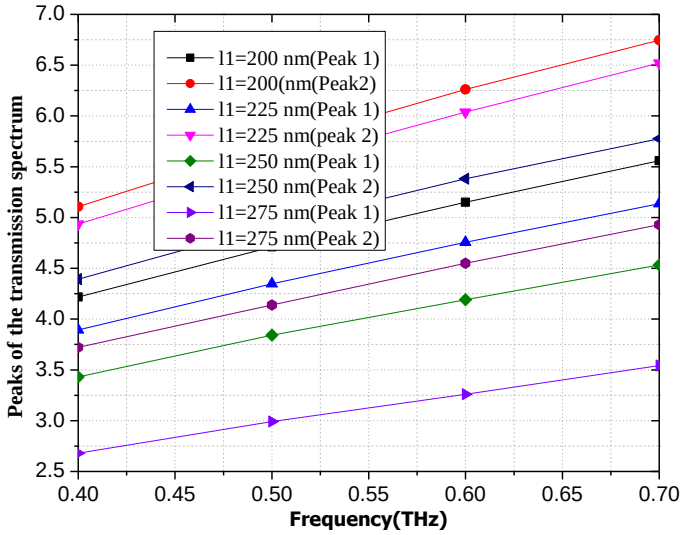

Fig. 4.2.2.3 Peaks of the transmission spectrum with chemical potential at different side lengths of ring resonator.

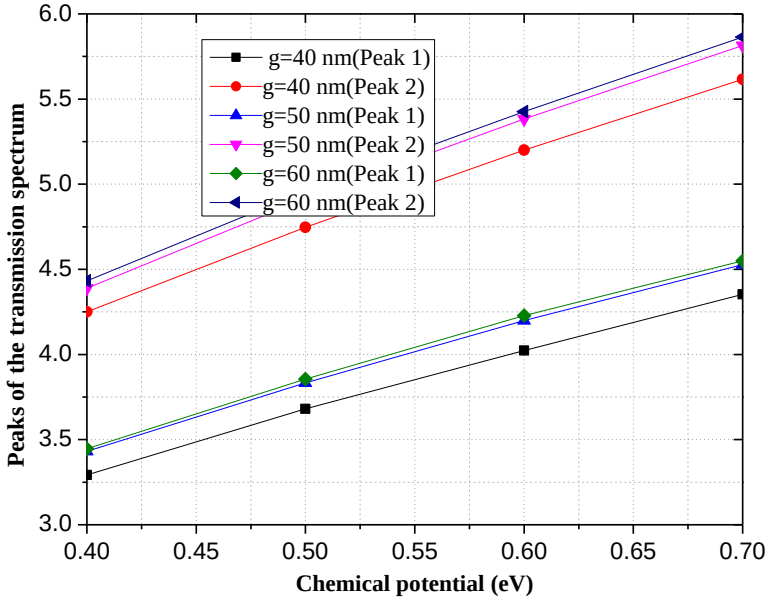

Fig. 4.2.2.4 Peaks of the transmission spectrum with chemical potential at different widths of input and output waveguides of graphene base split ring resonator.

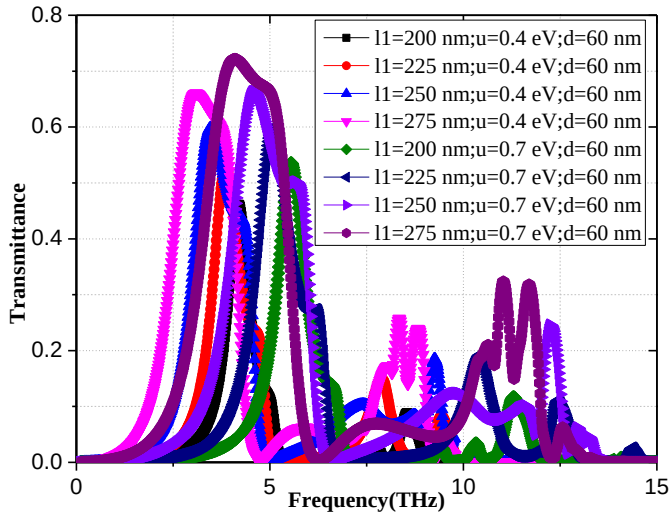

Fig. 4.2.2.5 Transmission spectrum with wavelength for different values of radius of ring resonator at specified values of chemical potential and widths.

4.2.3 Transmission properties of WDM: The graphene based CSRR can be utilized for channel demultiplexing operations, selecting the desired channel out of multiple channels [6]. As shown in Fig. 4.2.3.1(a), the three resonator structures have been taken at different values: resonator I at l1=600 nm; dielectric constant of surrounding material, e1=0.25; chemical potential of graphene, μ1=0.9, resonator II at l2=620 nm; e2=0.5; μ2=0.95, and resonator III at l3=600 nm; e3=1.0; μ3=1.0. The transmission characteristics with different chemical potentials of the CSRR and dielectric constant of the surrounding material have been obtained. the transmission spectra can be tuned to different frequencies with the variation in index of the material and electronic properties of graphene that can be tuned with the help of applied voltage or chemical doping, as shown in Fig. 4.2.3.1(b). The resonator I can be tuned to frequency 6.9 THz, resonator II at frequency 6.6 THz and resonator III at frequency 7.6 THz in the frequency band 6 to 8 THz. Likewise, the demultiplexer can be utilized for selecting appropriate channel among the transmitted ones.

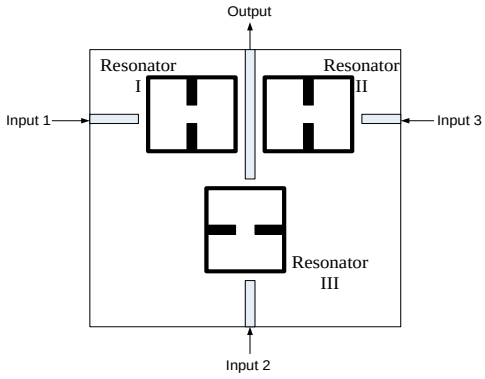

(a)

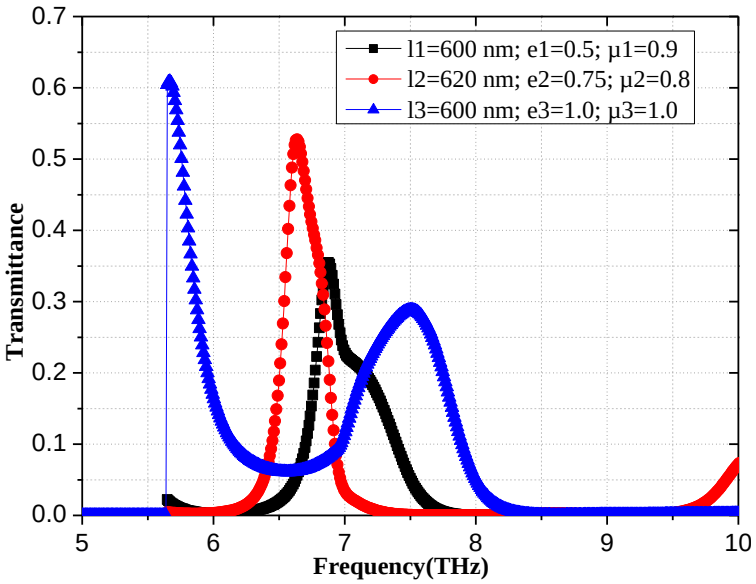

Fig. 4.2.3.1 Graphene based CSRR WDM and their transmission spectra with wavelength for different resonators.

Thus, the graphene based plasmonic CSRR structure coupled with graphene input and output nanostrip waveguides, GPNSWs has been utilized for wavelength demultiplexing of different channels. The simulations of transmission characteristics have been performed using CST microwave studio. The positions of the transmission peaks vary linearly with the change in chemical potential and thus, applied voltage bias of graphene. The transmission spectrum also varies with the change in structural parameters resulting in tuning of the transmission peaks at desired frequencies or wavelengths, increasing the radius of the ring resonator or decreasing the widths of the input and output waveguides, simultaneously suffering with the increase in transmission loss. The device possesses small size with high sensitivity. The device can be used as a tunable band pass filter in the THz frequency regime.

4.3 GPPW for sensing operation

Pristine graphene material withstands excellent characteristics in the optical and THz frequency range [9-12]. The graphene based plasmonic parallel plate waveguides have been a matter of interest for researchers due to their distinguishably extraordinary features [13-18]. Various graphene-based devices like tunable filter [2], low-pass filters [19], band-pass filters [20], directional coupler [21], oscillators [22], nano-patch antenna [23], cloaks [24], phase-shifters [25], coplanar waveguides and their discontinuities [8] and millimeter wave microstrip mixers [26] have been studied till date. Wang et. al. have proposed a surface plasmon polaritons (SPPs) based refractive index sensor consisting of ring resonator interconnected with two metal-insulator-metal (MIM) waveguides [9]. The transmission spectrum has been analyzed to obtain the sensing characteristics. We can increase the tuning range of SRR by optimizing the SRR modal characteristics [1]. Also, graphene based SRRs have been studied

[27-28], which can be used for sensing [29] and hybrid tunable meta-materials [30], etc. Here, we have utilized the graphene based suspended waveguide structures for the realization of millimeter wave/THz frequency circuits like Diplexer, sensors, etc., providing the features of tunability, high conductivity, high flexibility and low-cost alternative to inert metal such as silver and gold nano-circuitry.

In the following section, we have analyzed a suspended nanostrip waveguide using full wave e.m. solver to determine its transmission line characteristics such as propagation constant, and characteristic impedance. Closed form expressions for the determination of the propagation constant and characteristic impedance are also presented. This transmission line structure has been used to design a filter based Diplexer operating at THz frequencies. Moreover, a sensor structure with two graphene based suspended nanostrip lines coupled to each other by a modified ring resonator have been proposed. The chemical potential variation in graphene owes to the tuning capability of the graphene nano-device. The transmission peaks of SRR structures vary with the change in the dielectric constant of the material under sensing. The transmission spectrum at the output port provides the information about sensing characteristics of the graphene based structure.

4.3.1 Transmission characteristics of Graphene based suspended nanostrip waveguide

The proposed graphene based suspended nanostrip line has been shown in Fig. 2.2.2.1(a) having the substrate comprised of a silicon-dioxide layer (ε_r = 3.9) over a silicon wafer (ε_r = 11.9, σ = 0.00025 S/m).

4.3.2 Characteristics of graphene plasmonic diplexer using coupled line resonators

In the coupled line resonator design as shown in Fig. 4.3.2.1(a), two SIRs have been coupled and connected to input and output GPNSWs. The substrate for the above design is SiO_2 with lossy silicon at the bottom. The dimensions of the substrate are considered to be 480 nm x 2500 nm x 90 nm. The material parameters for graphene layer have been chosen to be the same. The thickness of the graphene layer is assumed to be 0.5 nm. Here, graphene material also provides tunability feature as compared to its conventional metal counterparts. Its simulated results have been shown in Fig. 4.3.2.1(b), which depict the region of pass-band from 4.3 to 4.9 THz.

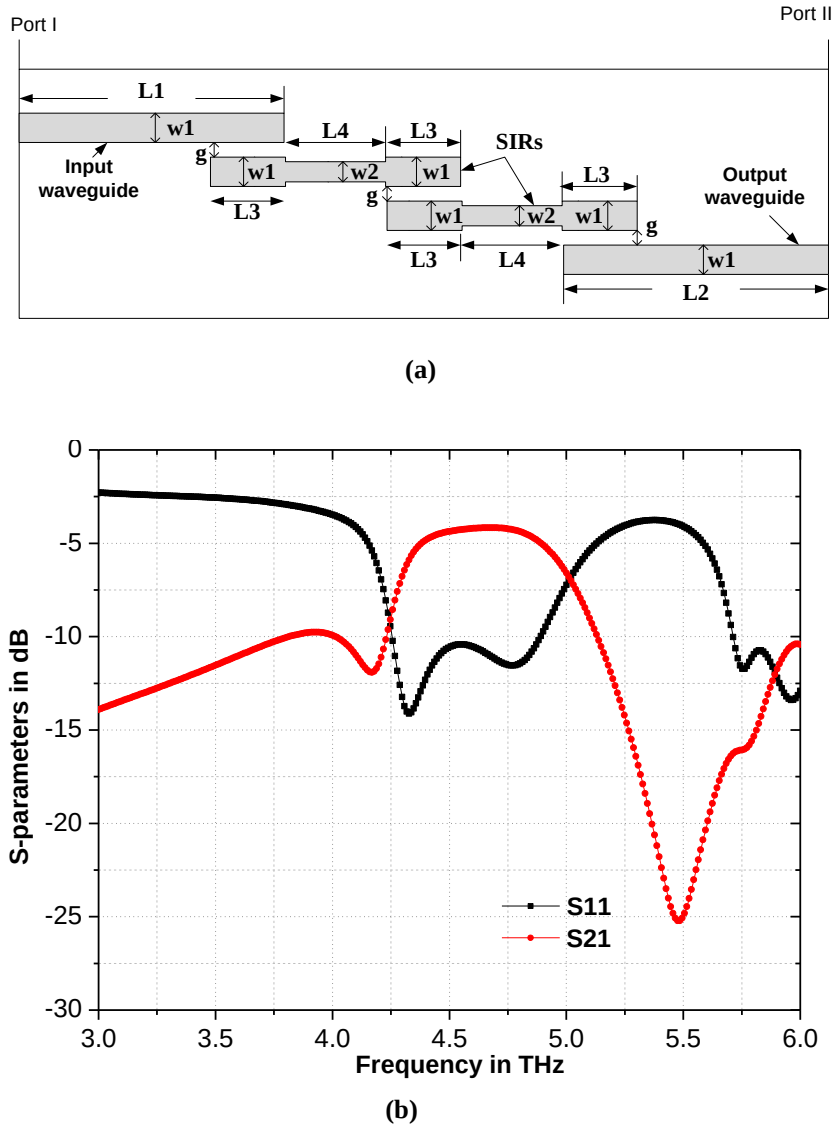

Fig. 4.3.2.1 (a) Schematic 2D diagram of wide-band graphene based band-pass filter, where *L1*=1300 nm, *L2*=1500 nm, *L3*=200 nm, *L4*=200 nm, *w1*=50 nm, *w2*=40 nm and *g*=40 nm. **(b)** Transmission and reflection coefficients of designed band-pass filter.

The coupled line resonator can be utilized to design a graphene plasmonic Diplexer, whose geometry is shown in Fig. 4.3.2.2 (a). It comprises of a 45° chamfered power divider circuit to divide the signal at port 1 into two parts which are passed through a band pass filter inserted in each of the output arms. The dimensions of this diplexer are: L_1 = 1000 nm, L_2 = 200 nm, L_3 = 200 nm, L_4 = 1000 nm, W_1 = 400 nm, W_2 = 200 nm, W_3 = 50 nm, W_4 = 50nm, W_5 = 40 nm. Here, the chemical potential of graphene in the upper arm is 0.3 eV and in the lower arm, 0.25 eV with other parameters chosen to be the same. Also, the simulated return loss, insertion loss and isolation characteristics of diplexer are shown in Fig. 4.3.2.2. The isolation between two output ports are more than 20 dB in the desired operating range as shown in Fig. 4.3.2.2 (b). The schematic diagram of the circuit is as follows:

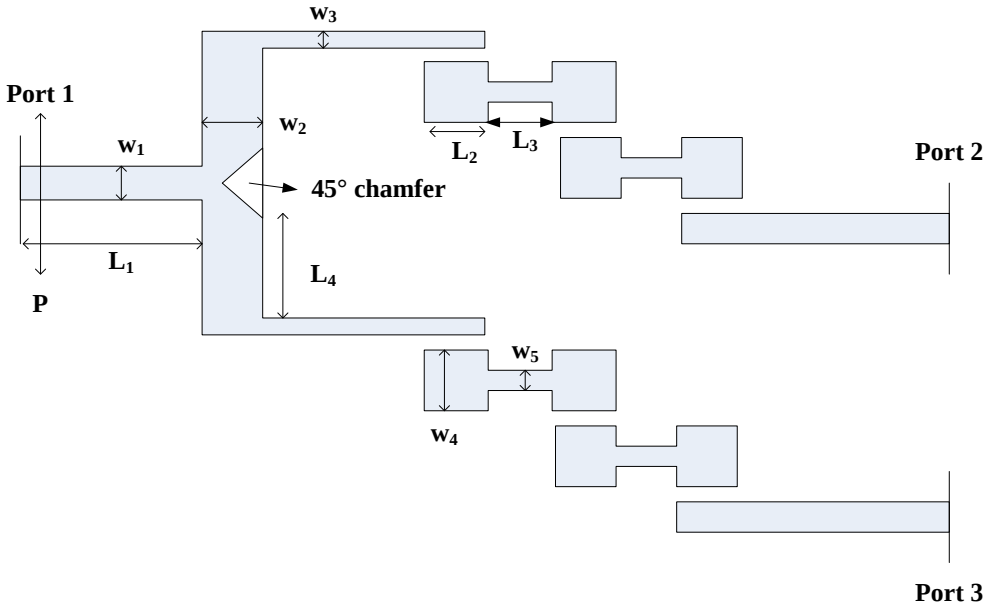

Fig. 4.3.2.2 Schematic diagram of Graphene based diplexer.

The GPNSW structure has been shown in Fig. 2.2.1.1. Based on this structure, a graphene plasmonic power splitter [31-33] has been designed as shown in Fig. 4.3.2.3, in which two graphene plasmonic waveguides have been coupled and connected to input nanostrip feed waveguide. The entire structure is designed on SiO_2 substrate with lossy silicon at the bottom. The dimensions of the substrate are taken to be 3480 nm x 4400 nm x 80 nm. The structure designed over the substrate is graphene layer with thickness 0.5 nm. The compensation has been achieved in the power splitter with the help of 45° chamfer as shown in Fig. 4.3.2.3 (a).

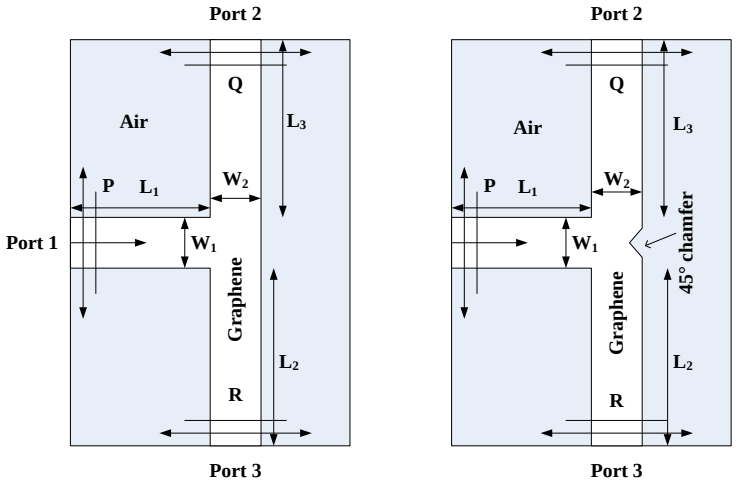

(a)

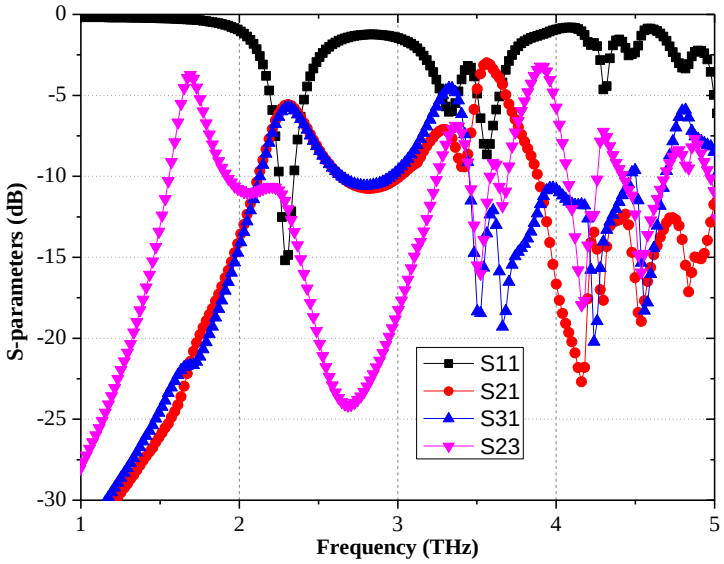

(b)

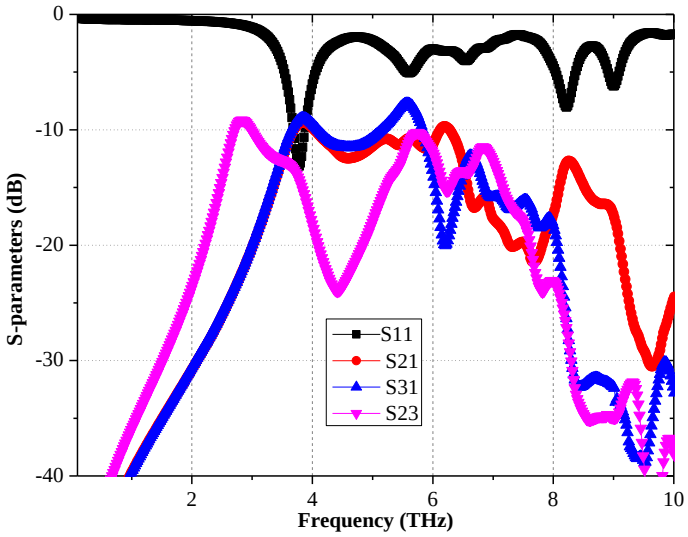

(c)

Fig. 4.3.2.3 (a) Schematic 2D diagram of graphene based power splitter. Transmission and reflection coefficients of designed power splitter **(b)** compensated **(c)** uncompensated type.

Simulation results

As shown in Fig. 4.3.2.3(b) and 4.3.2.3(c), the simulated results of the graphene based power splitter have been presented. In the plots, a single band is obtained at 3.5 THz in the uncompensated type graphene based power splitter whereas two bands at 2.4 THz and 3.4 THz have been obtained in the compensated type power splitter. The isolation loss has also been represented by S_{23}.

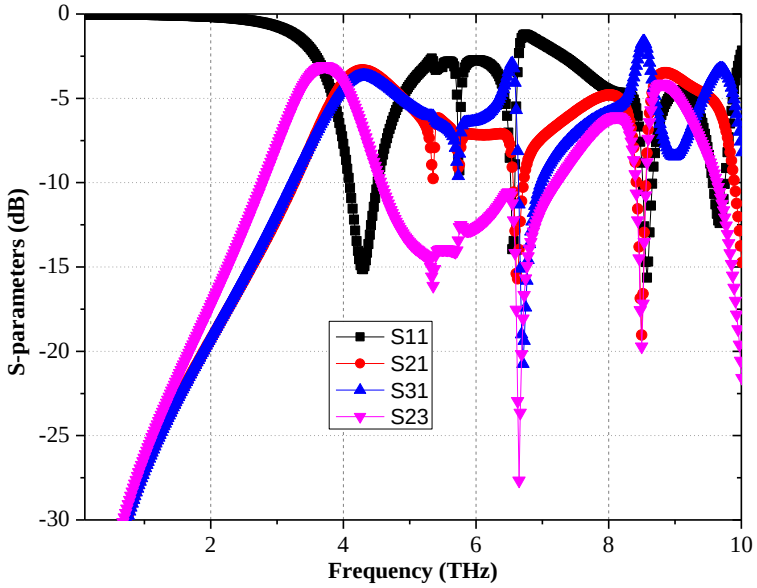

Fig. 4.3.2.4 S-parameters with frequency in THz for asymmetric power-splitter.

Next, the asymmetric power splitter simulation results have been presented in Fig. 4.3.2.4. This splitter has been obtained by increasing the width of the symmetric power splitter with w_1 varied from 200 nm to 400 nm.

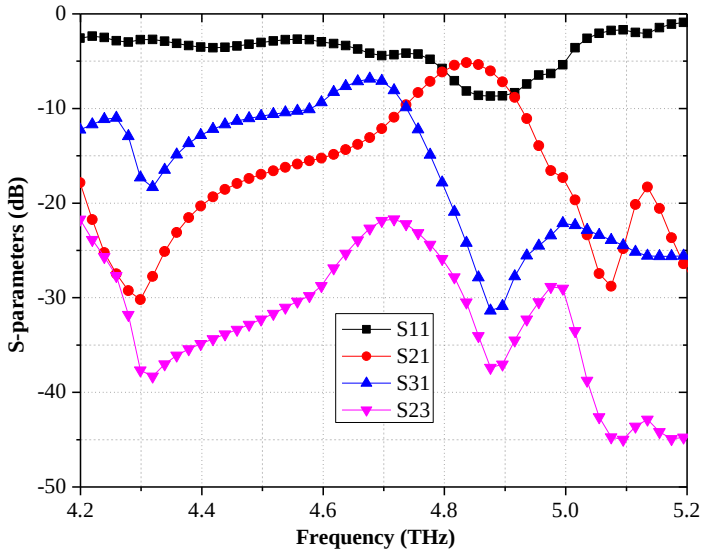

Fig. 4.3.2.5 Simulation results of graphene based diplexer.

The simulation results as shown in Fig. 4.3.2.5 depict that the Diplexer resonates at two frequencies. The first frequency band lies at 4.85 THz (resonant frequency of the upper - arm resonator) and the second one lies at 4.7 THz (resonant frequency of second resonator) with an insertion loss of around -22 dB. Therefore, the two frequency bands can be transmitted concurrently through the graphene Diplexer.

4.3.3 GPWs for sensing applications

The graphene plasmonic SRR structure has been discussed previously in Fig. 3.2.3.2. The structure is mentioned in Fig. 4.3.3.1 again for reference.

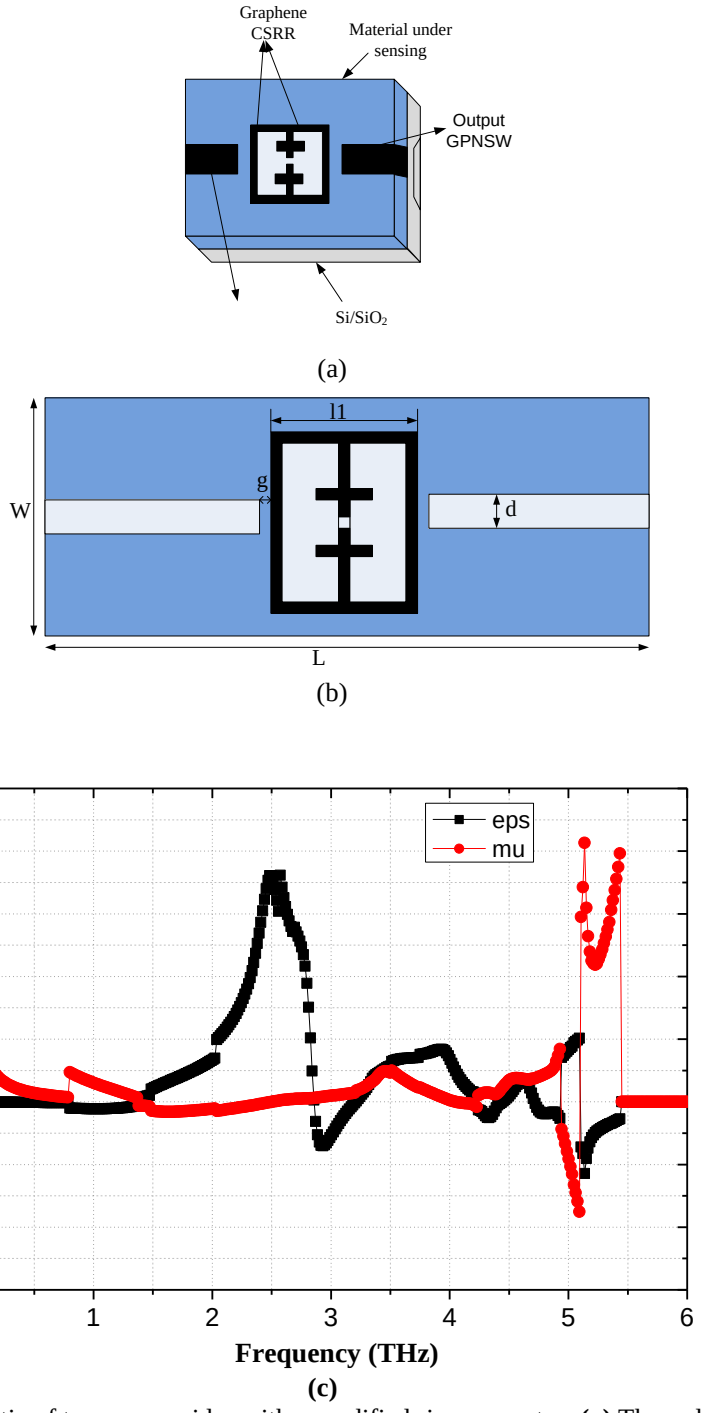

Fig. 4.3.3.1 Structure schematic of two waveguides with a modified ring resonator. **(a)** Three-dimensional view **(b)** Two-dimensional structure showing graphene based CSRR. **(c)** Dielectric permittivity and permeability of graphene based CSRR.

Fig. 4.3.3.2 shows the transmission spectrum for the above mentioned graphene based CSRR. The surface plasmonic resonances occur at some fixed frequencies in these characteristics. These transmission resonances have been shown with respect to the propagating frequencies.

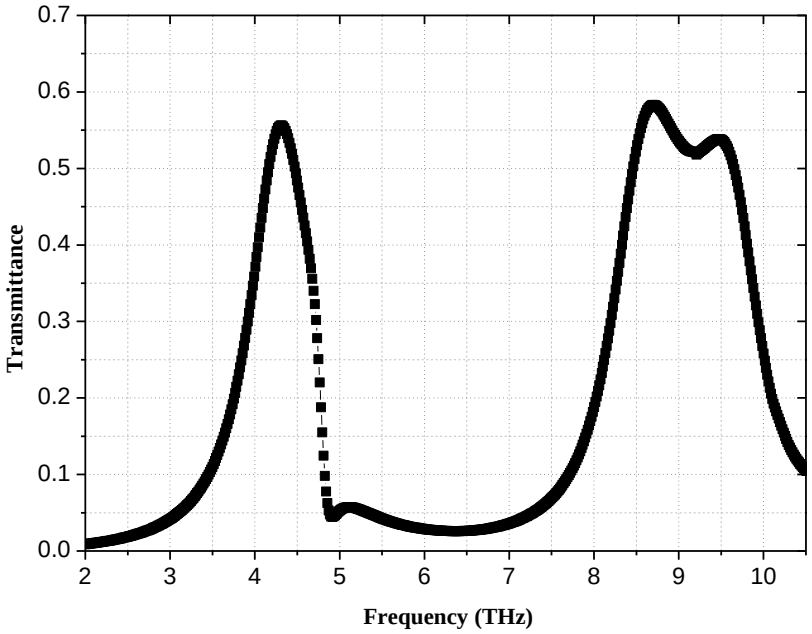

Fig. 4.3.3.2 Transmission spectrum of graphene based sensor structure.

Next, the transmission spectra of graphene based CSRR has been observed further with respect to various design parameters like chemical potential of graphene, refractive index of material, etc. Firstly, the transmission resonances have been obtained with different values of chemical potential of graphene as shown in Fig. 4.3.3.3. These resonances travel towards right with the increase in the values of applied chemical potential resulting in sufficient increase in transmission. These values of chemical potential have been varied from 0.2 to 1.0 eV. The transmission characteristics shows a linear variation with chemical potential. Next, the peaks of the transmission spectrum have been observed with frequency in Fig. 4.3.3.4 at different values of refractive index of the material under sensing, which can be used for detection of materials of different refractive index depending on its sensitivity [34-36].

As the dielectric constant, *eps* is varied from 0.2 to 0.4, the shift of the peak I equals to 6 nm. The sensitivity of the refractive index sensor can be calculated from $\frac{d\lambda}{dn}$, resulting in the refractive index sensitivity of 1341.64 nm/RIU for the peak. Here, peak positions are expressed in nm scale and RIU represents refractive index unit. There is an approximately linear relationship between the transmission resonances and dielectric constant as shown in Fig. 4.3.3.4. Thus, there is approximately linear shift in

the peaks of the transmission spectrum with the change in the values of dielectric constant and refractive index. Now, the impact of variation in values of structural parameters have been observed on the transmission characteristics of the graphene based CSRR structure.

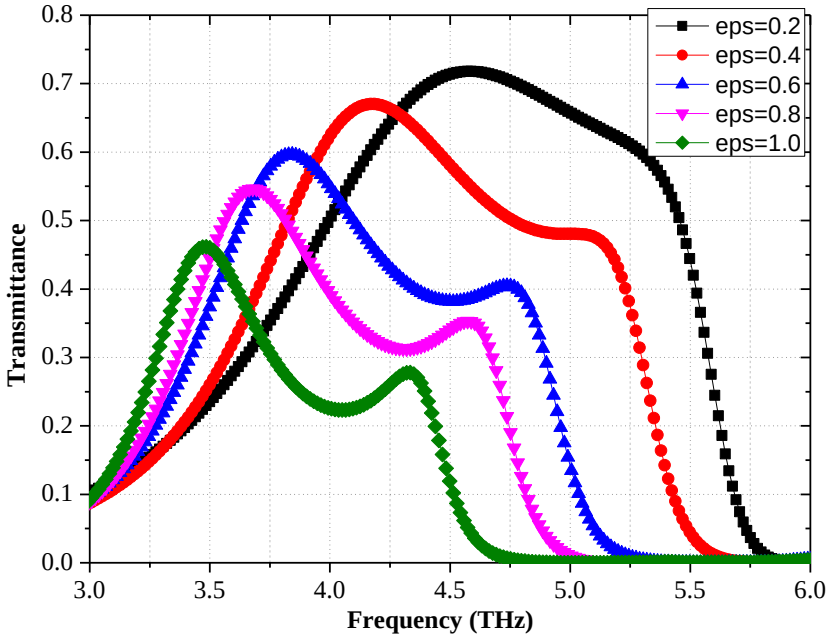

Fig. 4.3.3.3 Transmittance spectrum of graphene based sensor structure for different values of dielectric constant.

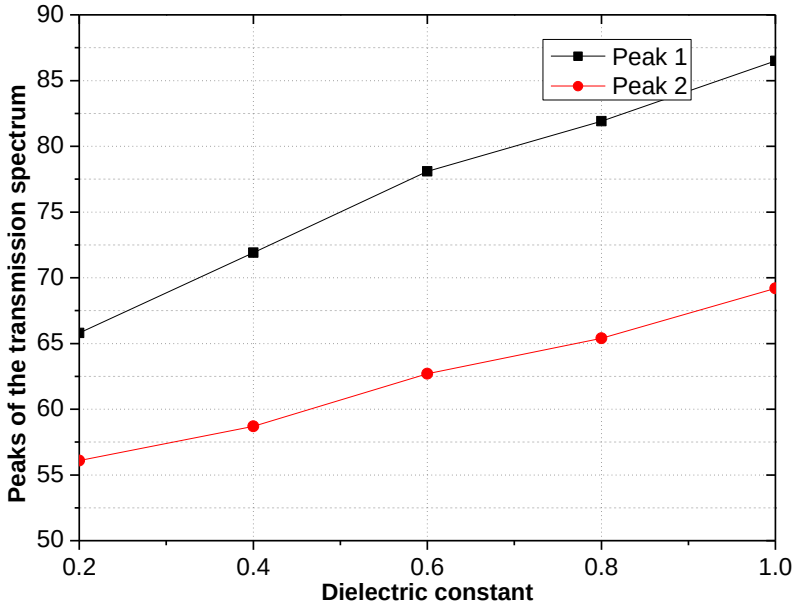

Fig. 4.3.3.4 Transmission spectrum of graphene based sensor with respect to dielectric constant showing the sensitivity to different refractive index material.

Firstly, the transmission peaks have been observed at different values of side lengths of ring resonator, l1=200 nm, 225 nm, 250 nm and 275 nm as shown in Fig. 4.3.3.5. There is a relative change in the position of the peaks of the transmission spectrum with change in the dimensions of the modified ring.

With the increase in side lengths, the transmission resonances are obtained at lower values of frequencies and consequently, higher values of wavelengths. As is clearly observed from the figure, as the transmission values decrease, the transmission loss also increases.

Fig. 4.3.3.6 gives the frequency spectra of the structure at different widths of input and output GPNSWs, considering different values of the widths to be d=10 nm, d=20 nm, d=30 nm, and d=40 nm. With the increase in widths, the transmission resonances are obtained at higher values of frequencies and consequently, lower values of wavelengths. The sensitivity of the sensor can be tuned by increasing the radius of the ring resonator or decreasing the widths of the input and output waveguides, simultaneously suffering with the increase in transmission loss.

Fig. 4.3.3.7 gives the frequency spectra of the structure for different lengths, *l1* of ring resonator. The spectra is obtained at specified values of chemical potential and widths of the input and output waveguides. Next, the sensitivity of the structure with different dielectric constant values of the material under sensing at different values of the side lengths of ring resonator, *l1* = 200 nm, 225 nm, and 250 nm and different values of the widths *d* = 80 nm, *d* = 120 nm, and *d* = 160 nm have been shown in tables 4.3.3.1 and 4.3.3.2. It can be inferred that the sensitivity and tunability of the graphene based SRR is better than other plasmonic waveguides. Also, the tables 4.3.3.1 and 4.3.3.2 depict the values of the sensitivities of the structure at different values of dielectric constant of the sensing material, *eps* with different values of side lengths of ring resonator, *l1* = 200 nm, 225 nm, and 250 nm for different widths of input and output nanostrip waveguides, *d* = 80 nm and *d* = 120 nm.

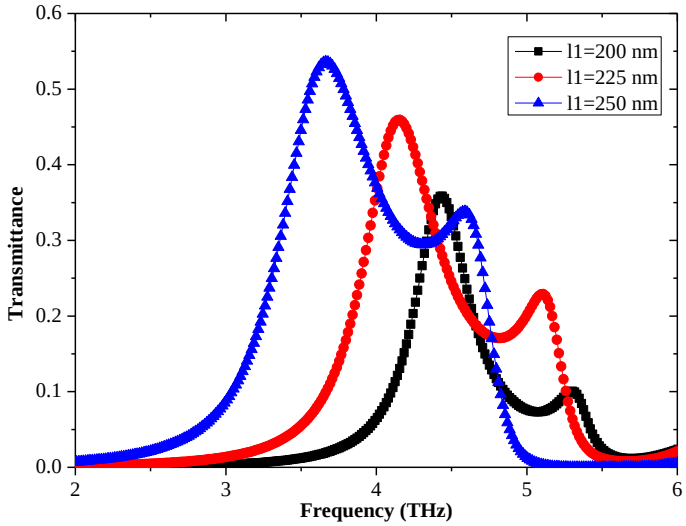

Fig. 4.3.3.5 Transmission spectrum with wavelength at different radii of ring resonator.

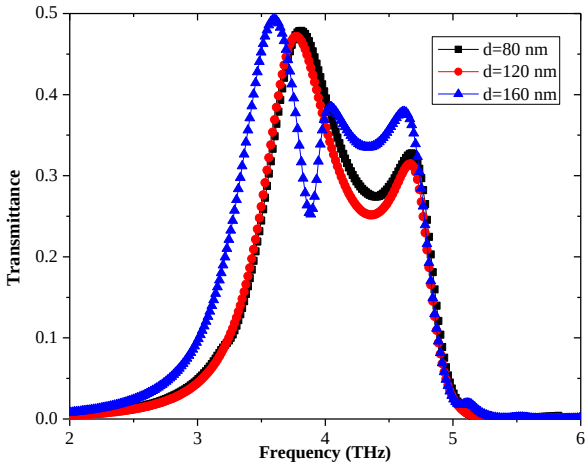

Fig. 4.3.3.6 The transmission spectrum with wavelength at different widths of input and output waveguides of graphene based split ring resonator.

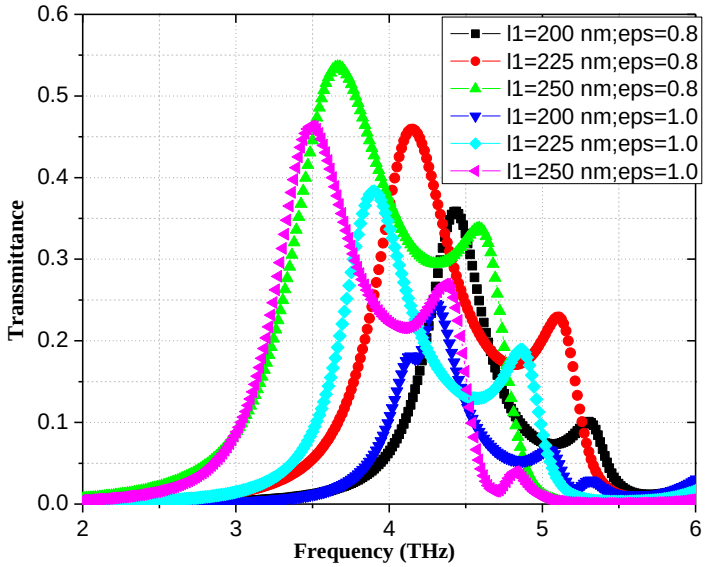

Fig. 4.3.3.7 Transmission spectrum with wavelength for different values of side-lengths of modified ring resonator at specified values of chemical potential and widths.

Table 4.3.3.1 Sensitivities of the structure at different values of dielectric constant of the sensing material, eps with different values of side lengths of ring resonator, l1=200nm, 225 nm, and 250 nm at d=80 nm.

***l1*=200 nm**	**λ(*eps*=0.2)**	**λ(*eps*=0.4)**	**Sensitivity(nm/RIU)**
Peak 1	53880	60284	14319.7793
Peak 2	43248	51710	18921.6072
	λ(*eps*=0.8)	**λ(*eps*=1.0)**	
Peak 1	67015	71003	8917.439
Peak 2	63090	65694	5822.721
***l1*=225 nm**	**λ(*eps*=0.2)**	**λ(*eps*=0.4)**	**Sensitivity(nm/RIU)**
Peak 1	58886	63983	11397.24
Peak 2	48236	52889	10404.42
	λ(*eps*=0.8)	**λ(*eps*=1.0)**	
Peak 1	78870	83594	10563.19
Peak 2	64175	66089	4279.834
***l1*=250 nm**	**λ(*eps*=0.2)**	**λ(*eps*=0.4)**	**Sensitivity(nm/RIU)**

Peak 1	61648	69748	18112.15
Peak 2	43248	51649	18785.21
	λ(*eps*=0.8)	**λ(*eps*=1.0)**	
Peak 1	78870	83594	10563.19
Peak 2	64175	66089	4279.834

Table 4.3.3.2 Sensitivities of the structure at different values of dielectric constant of the sensing material, *eps* with different values of side lengths of ring resonator, *l1*=200 nm, 225 nm, and 250 nm at d=120 nm.

***l1*=200 nm**	**λ(*eps*=0.2)**	**λ(*eps*=0.4)**	**Sensitivity(nm/RIU)**
Peak 1	61648	69748	18112.1506
Peak 2	43248	51649	18785.2071
	λ(*eps*=0.8)	**λ(*eps*=1.0)**	
Peak 1	78870	83594	10563.1851
Peak 2	64175	66089	4279.8341
***l1*=225 nm**	**λ(*eps*=0.2)**	**λ(*eps*=0.4)**	**Sensitivity(nm/RIU)**
Peak 1	62489	70183	17204.31
Peak 2	79250	83329	9120.921
	λ(*eps*=0.8)	**λ(*eps*=1.0)**	
Peak 1	43392	44236	1887.241
Peak 2	64891	66236	3007.511
***l1*=250 nm**	**λ(*eps*=0.2)**	**λ(*eps*=0.4)**	**Sensitivity(nm/RIU)**
Peak 1	64647	71810	16016.95
Peak 2	55237	61044	12984.85
	λ(*eps*=0.8)	**λ(*eps*=1.0)**	
Peak 1	81413	85196	8459.045
Peak 2	64930	66048	2499.924

4.4 Directional coupler

Coupled-mode theory has been studied in plasmonic waveguides [37]. The unique properties of optical waveguides electrically controlled by means of graphene layers are investigated [38]. Non-linear graphene based couplers have been studied between two closely spaced graphene layers [39].The tuning of SPPs in graphene directional couplers for switching has been studied [40]. The double-layer graphene sheets and three-layer graphene sheets based coupler has been designed [41]. An asymmetric directional coupler has been designed using silicon waveguide (SW) and a graphene multilayer embedded silicon waveguide (GMESW) [42]. Graphene based tunable plasmonic directional coupler has also been studied in the THz frequency regime [43]. Coupled-mode theory (CMT) has been used to analyze the coupling between three graphene sheets with curved configuration [44]. A compact directional coupler with high-index dielectric ridges for planar integration has been studied [45].

A graphene plasmonic directional coupler has been designed as shown in Fig. 4.4.1(a). In this structure, two GPCPWs have been combined using a 90° bend to form the edge coupled directional coupler. The elliptical corrugations and stubs have been provided on both sides to enhance the

transmission characteristics. The coupler has the following parameters: length, L = 580 nm, gap, g = 150 nm, length of stub, l = 300 nm, width, w = 20 nm, length of substrate = 2000 nm, width of substrate = 3000 nm, with corrugation dimensions: x = 60 nm, x_1 = 150 nm, x_2 = 100 nm and x_3 = 150 nm. The rest of the parameters are same as in case of GPCPW mentioned earlier in chapter 2. Its ports have been shown in Fig. 4.4.1 (a). Its simulated results have been shown in Fig. 4.4.1(b).

The S-matrix for the directional coupler is given by:

$$S = \begin{bmatrix} S_{11} & S_{12} & S_{13} & S_{14} \\ S_{21} & S_{22} & S_{23} & S_{24} \\ S_{31} & S_{32} & S_{33} & S_{34} \\ S_{41} & S_{42} & S_{43} & S_{44} \end{bmatrix} \qquad \text{.....(4.4.1)}$$

with power at the input port as P_1 and power at the output ports, P_i for the i^{th} port. Here, coupling is defined by:

$$C = -10\log\frac{P_3}{P_1} = -20\log|S_{31}| \quad \text{(dB)} \qquad \text{....(4.4.2)}$$

The isolation is given by

$$I = -10\log\frac{P_4}{P_1} = -20\log|S_{41}| \quad \text{(dB)} \qquad \text{....(4.4.3)}$$

The direct transmission is given by:

$$T = -10\log\frac{P_2}{P_1} = -20\log|S_{21}| \quad \text{(dB)} \qquad \text{....(4.4.4)}$$

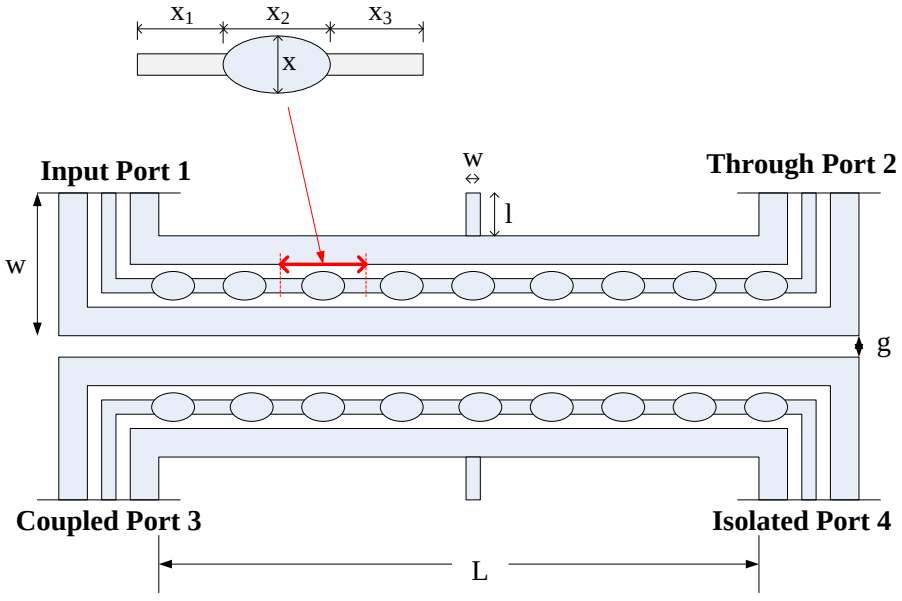

Fig. 4.4.1 (a) Schematic diagram of graphene plasmonic directional coupler.

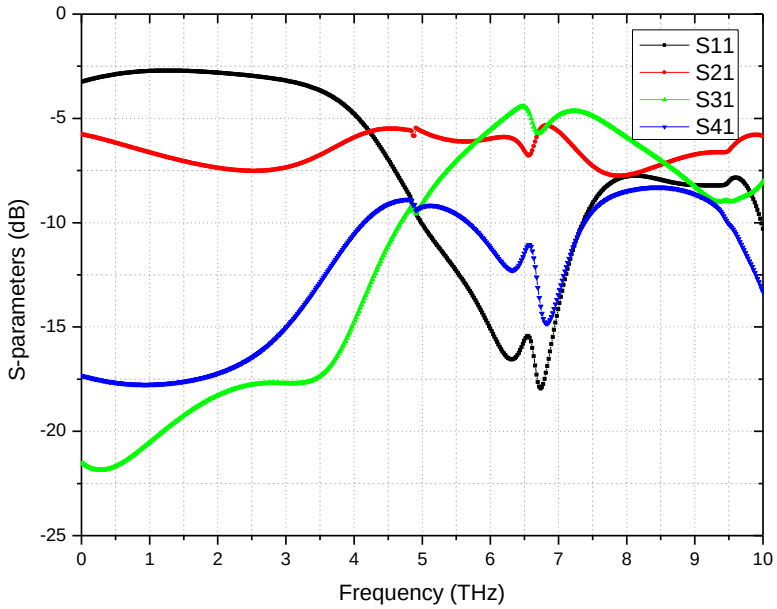

Fig. 4.4.1 (b) Transmission characteristics of graphene coupler.

The directivity is the power out the isolated port relative to the coupled power and is defined by:

$$D = I - C = -10\log\frac{P_4}{P_3} = -20\log\left|\frac{S_{41}}{S_{31}}\right| \quad \text{(dB)} \quad \ldots.(4.4.5)$$

In our case, the coupling is 5 dB. The isolation is 15 dB and the directivity is 10 dB. Therefore, low amount of power is delivered to the isolated port. The high insertion loss may be due to the mismatching and reflection losses.

4.5. CONCLUSION

In this chapter, we have studied the use of GPWs for the operation of demultiplexing using wavelength-division-demultiplexer. Further, a diplexer has been designed using GPSNSW and then, a directional coupler has been designed using GPCPW.

REFERENCES:

[1] T. Wu, Y. Liu, Z. Yu, Y. Peng, C. Shu, and H. He, "The sensing characteristics of plasmonic waveguide with a ring resonator", *Opt. Commun.*, vol. 22, no. 7, pp. 7669-7677, Mar. 2014.

[2] Y. Gao, G. Ren, B. Zhu, L. Huang, H. Li, B. Yin, and S. Jian, "Tunable Plasmonic Filter Based on Graphene Split-Ring", *Plasmonics*, vol. 11, no. 1, pp. 291–296, Aug. 2015.

[3] P. Q. Liu, I. J. Luxmoore, S. A. Mikhailov, N. A. Savostianova, F. Valmorra, J. Faist, and G. R. Nash, "Highly tunable hybrid metamaterials employing split-ring resonators strongly coupled to graphene surface plasmons", *Nat. Commun.*, vol. 6, pp. 8969 1-7, Nov. 2015.

[4] Y. P. Chen, W. E. I. Sha, L. Jiang, and J. Hu, "Graphene plasmonics for tuning photon decay rate near metallic split-ring resonator in a multilayered substrate", *Opt. Express.*, vol. 23, no. 3, pp. 2798-2807, Jan. 2015.

[5] C. Zhao and J. Zhang, "Plasmonic Demultiplexer and guiding", *ACS*, vol. 4, no. 11, pp. 6433-6438, Oct. 2010.

[6] G. Wang, H. Lu, X. Liu, D. Mao, and L. Duan, "Tunable multi-channel wavelength demultiplexer based on MIM plasmonic nanodisk resonators at telecommunication regime", *Opt. Express*, vol. 19, no. 4, pp. 3513-3518, Feb. 2011.

[7] N. Joshi and N. P. Pathak, "Graphene-backed graphene plasmonic coplanar waveguide (GB-GPCPW) for terahertz integrated circuit applications", *IEEE Proceedings of AEMC*, no. 103, Dec. 2015.

[8] N. Joshi and N. P. Pathak, "Modeling of graphene coplanar waveguide and its discontinuities for THz integrated circuit applications", *Plasmonics*, vol. 2017, no. 12, pp. 1545-1554, Jan. 2016.

[9] B. Wang and G. P. Wang, "Plasmonic waveguide ring resonator at terahertz frequencies", *Appl. Phys. Lett.*, vol. 89, no. 13, pp. 1–4, Aug. 2006.

[10] X. Gu, I. T. Lin, and J. M. Liu, "Extremely confined terahertz surface plasmon-polaritons in graphene-metal structures", *Appl. Phys. Lett.*, vol. 103, (2013) 071103 1-4.

[11] T. Low and P. Avouris, “Graphene Plasmonics for Terahertz to Mid-Infrared Applications”, *ACS*, vol. 8, no. 2, pp. 1086-1101, Jan. 2014.

[12] J. S. Gómez-Díaz and J. Perruisseau-Carrier, “Microwave to THz properties of graphene and potential antenna applications”, *Proceedings of ISAP2012, Nagoya, Japan*, pp. 239-242, 2012.

[13] A. N. Grigorenko, M. Polini, and K. S. Novoselov, “Graphene plasmonics – optics in flatland”, *Nat. photon.*, 6, pp. 749-758, 2012.

[14] D. Correas-Serrano, J. S. Gomez-Diaz, J. Perruisseau-Carrier and A. Álvarez-Melcón, “Spatially dispersive graphene single and parallel plate waveguides: Analysis and circuit model,” *IEEE Trans. Microw. Theory Tech.*, vol. 61, no. 12, pp. 4333–4344, Dec. 2013.

[15] A. Malekabadi, S. A. Charlebois and D. Deslandes, “Parallel plate waveguide with anisotropic graphene plates: Effect of electric and magnetic biases,” *J. Appl. Phys.*, vol. 113, pp. 113708 1-9, March 2013.

[16] J. S. Gomez-Diaz, J. R. Mosig and J. Perruisseau-Carrier, “Effect of Spatial Dispersion on Surface Waves Propagating Along Graphene Sheets,” *IEEE Trans. Antennas Propag.*, vol. 61, no. 7, pp. 3589-3596, July 2013.

[17] H. Hajian, A. Soltani-Vala and M. Kalafi, “Optimizing terahertz surface plasmons of a monolayer graphene and a graphene parallel plate waveguide using one-dimensional photonic crystal,” *J. Appl. Phys.*, vol. 114, no. 2013, pp. 0331021-8, July 2013.

[18] G. W. Hanson, “Quasi-transverse electromagnetic modes supported by a graphene parallel-plate waveguide,” *J. Appl. Phys.*, vol. 104, pp. 1–5, Oct. 2008.

[19] D. Correas Serrano, J. S. Gomez-Diaz, J. Perruissea-Carrier, Alvarez-Melcon, “A Graphene-based plasmonic tunable low-pass filters in the THz band,” *IEEE T. nano.*, vol. 13, no. 6, pp. 1145-1153, Nov. 2014.

[20] H. Deng, Y. Yan, and Y. Xu, “ Tunable flat-top bandpass filter based on coupled resonators on a graphene sheet ,” *IEEE Photonic. Techn. L.*, vol. 27, no. 11, pp. 1161-1164, June 2015.

[21] M. D. He, K. J. Wang, L. Wang, J. B. Li, J. Q. Liu, Z. R. Huang, L. Wang, L. Wang, W. D. Hu, and X. Chen, “Graphene based terahertz tunable plasmonic directional coupler,” *Appl.*

Phys. Lett., vol. 105, no. 081903, pp. 1-5, Aug. 2014.

[22] F. Rana, "Graphene terahertz plasmon oscillators," *IEEE T. Nano.*, vol. 7, no. 1, pp. 91-99, Jan. 2008.

[23] I. Llaster, C. Kremers, A. C. Aparicio, J. M. Jornet, E. Alarcon, and D. N. Chigrin, "Graphene based nano patch antenna for terahertz radiation, " *Elsevier*, June 2012.

[24] P. Y. Chen and A. Alù, "Atomically thin surface cloak using graphene monolayers," *ACS Nano*, vol. 5, pp. 5855–5863, June 2011.

[25] P. Y. Chen, C. Argyropoulos and A. Alu, "Terahertz antenna phase shifters using integrally-gated graphene transmission-lines," *IEEE Trans. Antennas Propag.*, vol. 61, no. 4, pp. 1528–1537, April 2013.

[26] G. Hotopan, S. Ver Hoeye, C. Vazquez, R. Camblor, M. Fernandez, F. Las Heras, P. Alvarez, and R. Menendez, "Millimeter wave microstrip mixer based on graphene," *Progress in Electromagnetics Research*, vol. 118, pp. 57-69, Jan. 2011.

[27] J. Wang, W. B. Lu, X. B. Li, X. F. Gu, and Z. G. Dong, "Plasmonic metamaterial based on the complementary split ring resonators using graphene," *J. Phys. D. Appl. Phys.*, vol. 47, no. 32, p. 325102, July 2014.

[28] S. Cakmakyapan, H. Caglayan, and E. Ozbay, "Coupling enhancement of split ring resonators on graphene," *Carbon*, vol. 80, no. 1, pp. 351–355, Aug. 2014.

[29] H. J. Chen and K. Di Zhu, "Graphene-based nanoresonator with applications in optical transistor and mass sensing," *Sensors (Switzerland)*, vol. 14, no. 9, pp. 16740–16753, Sept. 2014.

[30] P. Q. Liu, I. J. Luxmoore, S. A. Mikhailov, N. A. Savostianova, F. Valmorra, J. Faist, and G. R. Nash, "Highly tunable hybrid metamaterials employing split-ring resonators strongly coupled to graphene surface plasmons," *Nat. Commun.*, vol. 6, pp. 89691-7, Nov. 2015.

[31] A. Jain, A. K. Gupta, D. K. Sharma, P. R. Hannurkar, and S. K. Pathak, "Design and analysis of a high-power radial multi-way combiner," *International Journal of Microwave and Wireless Technologies*, vol. 6, no. 1, pp. 83-91, Feb 2014.

[32] A. Jain, D. K. Sharma, A. K. Gupta, and P. R. Hannurkar, "High power solid state RF amplifier for proton accelerator," *Review of Scientific Instruments*, vol. 79, no. 1, pp. 014702 1-7, Jan 2008.

[33] A. Jain, P. R. Hannurkar, S. K. Pathak, A. Biswas, and M. Srivastva, "Improved performance of two-way power divider using dielectric resonator," *Microwave and Optical Technology Letters*, vol. 56, no. 4, pp. 858-861, April 2014.

[34] A. K. Jha, M. J. Akhtar, "Design of Multilayered Epsilon-Near-Zero Microwave Planar Sensor for Testing of Dispersive Materials," *IEEE Transactions on Microwave Theory and Techniques*, vol. 63, no.8, pp. 2418-2426, Aug. 2015.

[35] A. K. Jha, M. J. Akhtar, "Elevated and tapered microstrip coupled ENZ SIW sensor for microwave testing of radome and building materials in 3G and ISM bands," *URSI Asia-Pacific Radio Science Conference (URSI AP-RASC)*, pp. 1761-1764, Aug. 2016.

[36] K. T. M. Shafi, A. K. Jha, M. J. Akhtar, "Improved Planar Resonant RF Sensor for Retrieval of Permittivity and Permeability of Materials," *Sensors Journal IEEE*, vol. 17, no. 17, pp. 5479-5486, July 2017.

[37] Ma, Y. Li, and X. Zhang, "Coupled Mode Theory for Surface Plasmon Polariton Waveguides," *Plasmonics*, vol. 8, no. 2, pp. 769-777, Dec. 2012.

[38] A. Locatelli, A. D. Capobianco, M. Midrio, S. Boscolo and C. D. Angelis, "Graphene-assisted control of coupling between optical waveguides," *Opt. Exp.*, vol. 20, no. 27, pp. 28479-28484, Dec. 2012.

[39] D. A. Smirnova, A. V. Gorbach, I. V. Iorsh, I. V. Shadrivov and Y. S. Kivshar, "Nonlinear switching with a graphene coupler," *Phys. Rev. B*, vol. 88, no. 4-15, July 2013.

[40] A. Auditore, C. D. Angelis, A. Locatelli and A. B. Aceves, "Tuning of surface plasmon polaritons beat length in graphene directional couplers," *Opt. Lett.*, vol. 38, no. 20, Oct. 2013.

[41] H. Li, L. Wang, Z. Huang, B. Sun, X. Zhai and X. Li, "Mid-infrared, plasmonic switches and directional couplers induced by graphene sheets coupling system," *Europhysics Letters*, vol. 104, no. 3, Nov. 2013.

[42] T. Zhang, X. Yin, L. Chen and X. Li, "Ultra-compact polarization beam splitter utilizing a graphene-based asymmetrical directional coupler," *Opt. Lett.*, vol. 41, no. 2, Jan. 2016.

[43] He MD, Wang KJ, Wang L., Li JB, Liu JQ, Huang ZR, Wang L., Wang L, Hu WD, Chen X, "Graphene based terahertz tunable plasmonic directional coupler," *Appl. Phys. Lett.*, vol. 105, no. 081903, pp. 1-5, Aug. 2014.

[44] W. Huang, S. J. Liang, E. Kyoseva and L. K. Ang, "Adiabatic control of surface-plasmon-polaritons in a 3-layers graphene curved configuration," *Carbon,* Nov. 2017.

[45] F. Xu, H. Zhang and Y. Sun, "Compact graphene directional couplers based on dielectric ridges for planar integration," *Optik,* vol. 131, pp. 588-591, Feb. 2017.

Chapter 5

Design and Simulation of Graphene Plasmonic Waveguide Based Antenna

5.1 Introduction

The terahertz technology has become an interesting talk of the town in the last few decades. The one-atom thick material, Graphene has witnessed an increasing research interest enchanting a wide and unlimited number of researchers and scientists all over the world. In conjunction with the terahertz technology view, the graphene surface plasmon polaritons (SPPs) have numerous advantages over the SPPs of inert gases like gold, silver, etc showing the features of higher field confinement, lower losses and longer propagation lengths leaving an everlasting impact on the field of nanotechnology in the terahertz frequency regime. It has developed a significant niche in the field of plasmonics with the ongoing research in the development of graphene based plasmonic devices like phase shifters, waveguides, filters, etc. The terahertz frequency range has been explored widely as well as tried to be confined in a subwavelength scale using graphene plasmonics. The performance of bends and splitters in graphene nano-ribbon waveguides have been presented by Zhu et. Al [1]. Fractal antennas have also been studied [2-4]. Graphene material has been used as spin and valley beam splitter through Goos-Hanchen effect in which two stripes placed on monolayer graphene serve the purpose [5-7]. Graphene loaded plasmonic antennas have also been used for broad-band electrical tuning [8]. Tunable antennas with graphene based artificial-magnetic conductor have also been demonstrated to provide gains higher than 9 dB with bandwidths of 47% [9]. Reconfigurable THz reflectarrays have also been designed using graphene electric field effect [10]. Recently, graphene based optically transparent dipole antennas have also been studied [11]. The nano-patch antenna [12-16] arrays can be designed with the help of the power-splitter. The graphene based nano-patch antenna provide a promising performance with excellent radiation characteristics [17-18]. THz antennas have been studied, yet need to be explored further [19-21]. The graphene based-power-splitter and nano-dipatch antenna have been designed. The graphene based dipatch antenna in nanoscale dimensions has not been so far reported in open literature for nanoscale terahertz communications.

Here, a nanostrip waveguide has been used to design a power splitter operating at THz frequencies. The simulation results of symmetric and asymmetric T-junction models have been presented succeeding the discussion of nano-patch antenna with two graphene patches coupled to each other by the power splitter. The chemical potential variation in graphene facilitates the tuning capability of the graphene nanodevice. The graphene full wave dipatch antenna provides 2.1 dB gain, bandwidth 100 GHz and around 50% efficiency. The patch antenna arrays can be designed for further enhancement of antenna radiation characteristics.

5.2 GRAPHENE NANO-DIPATCH ANTENNA

A graphene plasmonic based di-patch antenna has been designed with the help of compensated power splitter. Firstly, the nanostrip patch antenna utilized in the modeling of di-patch antenna has been discussed. The nano-antenna consists of a conducting patch made of a very thin layer of graphene and SiO_2/Si substrate with dielectric constant of 11.9. The graphene based patch antenna is shown in Fig. 5.2.1 and its dimensions are shown in Table 5.2.1.

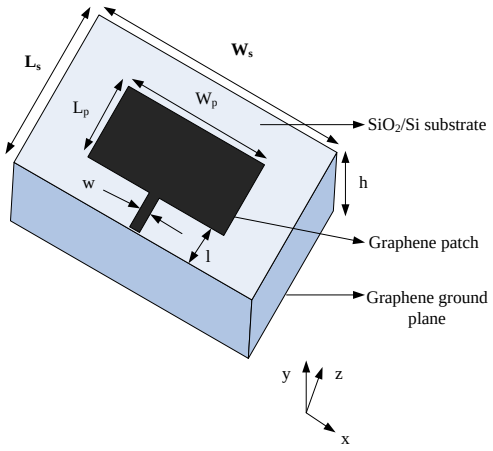

Fig. 5.2.1 Schematic diagram of graphene patch antenna.

Table 5.2.1 Dimensions of graphene patch antenna.

Dimensions of the graphene patch antenna	
Parameters	Dimensions (nm)
Patch length (L_p)	5000
Patch width (W_p)	3325
Substrate length (L)	20000
Substrate width (W)	12000
Substrate height (h)	120
Nanostrip feed length (l)	5000
Nanostrip feed width (w)	100

Its return loss characteristics have been shown in Fig. 5.2.2(a). The radiation characteristics like VSWR, radiation patterns have been analyzed next.

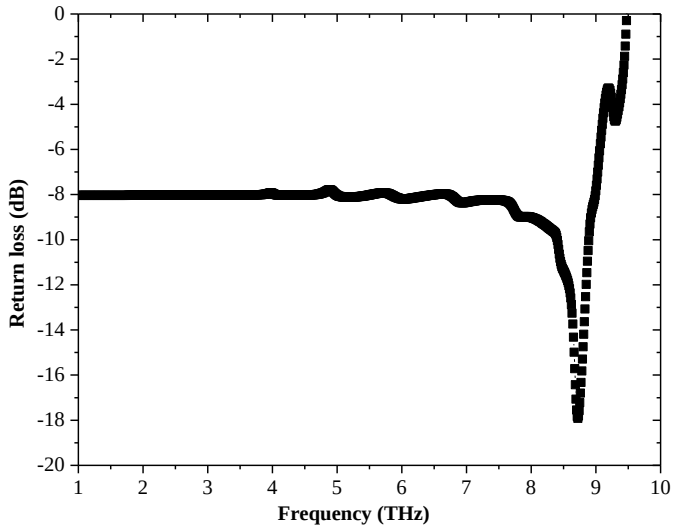

Fig. 5.2.2. (a) Return loss for graphene patch antenna.

The graphene plasmonic patch antenna resonates in the THz frequency band, allowing the surface-plasmon-polariton resonances in the structure [22]. The analysis has been performed in the frequency range 0.1 to 10 THz. It can be inferred from the reflection coefficient plots that the antenna resonates at the frequency 8.8 THz with the return loss of -18.5 dB. The VSWR of the patch antenna has been shown in Fig. 5.2.2(b). Fig. 5.2.2(c) depicts the 3D radiation pattern, E-plane and H-plane patterns for the THz operation.

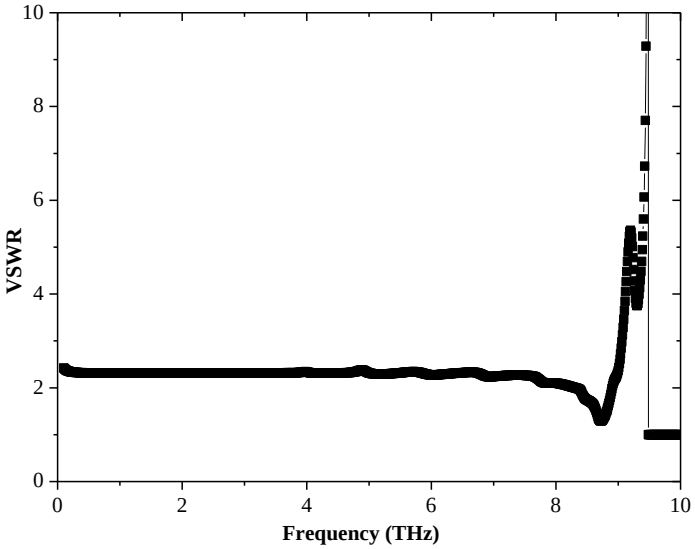

Fig. 5.2.2 (b) VSWR for graphene patch antenna.

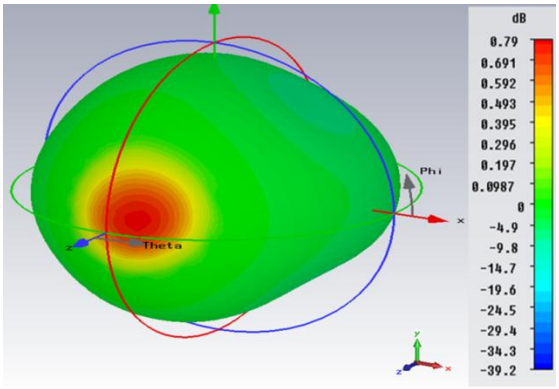

(c)

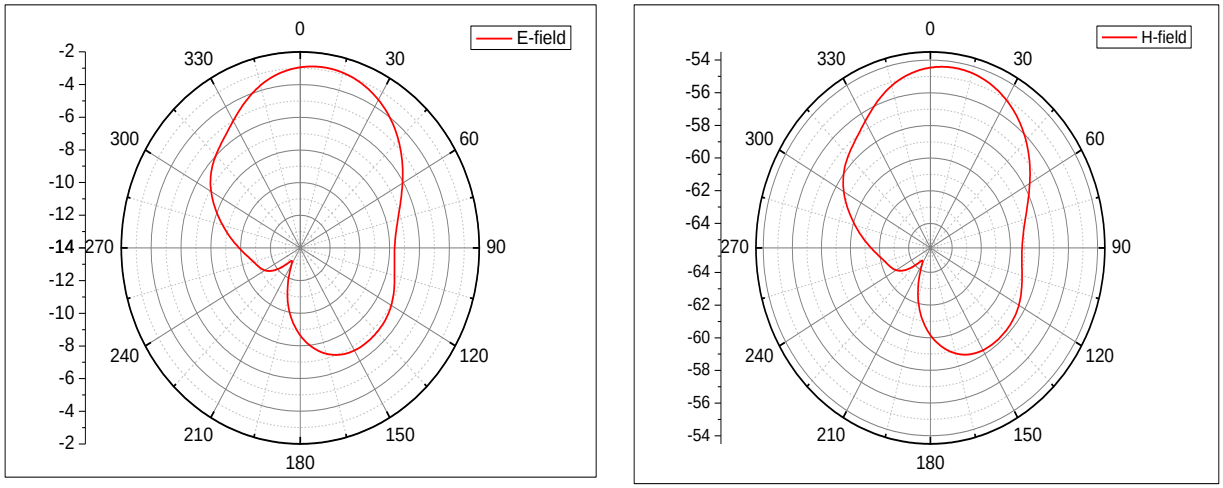

(d)

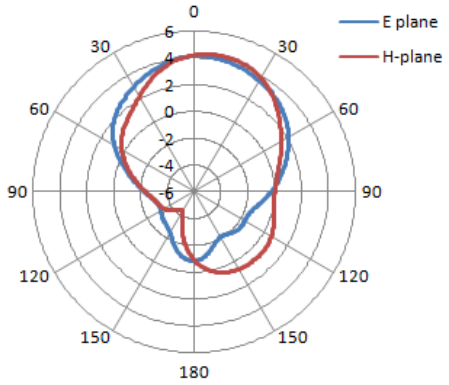

(e)

Fig. 5.2.2 (c) 3D radiation pattern at 8.8 THz. **(d)** Co and cross-polarized patterns at 8.8 THz. **(e)** Far-field E-plane and H-plane plots.

Then, the graphene based dipatch antenna has been shown in Fig. 5.2.3 and its radiation characteristics have been analyzed further. The antenna parameters have been compared in Table 5.2.2. The return loss and far-field antenna properties have been shown in Fig. 5.2.4. The graphene dipatch antenna shows higher gain and efficiency as compared to patch antenna and can be useful in the design of parallel patch antenna arrays to obtain higher gain and efficiencies.

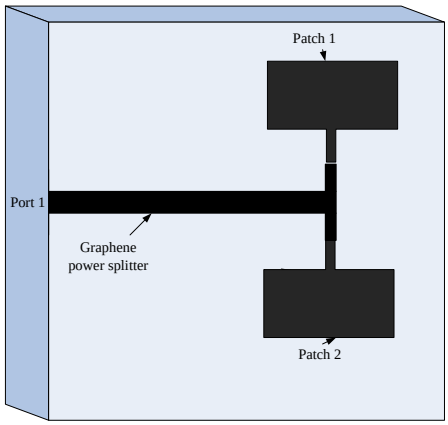

Fig. 5.2.3 Schematic diagram of graphene dipatch antenna.

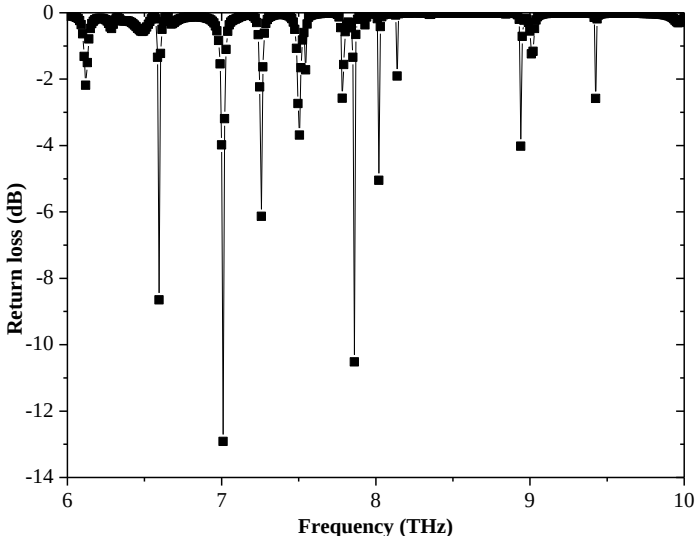

Fig. 5.2.4 (a) Return loss for graphene dipatch antenna.

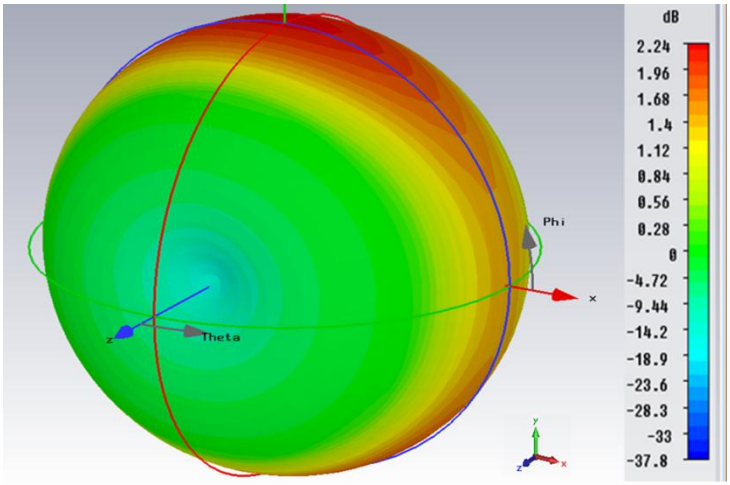

(b)

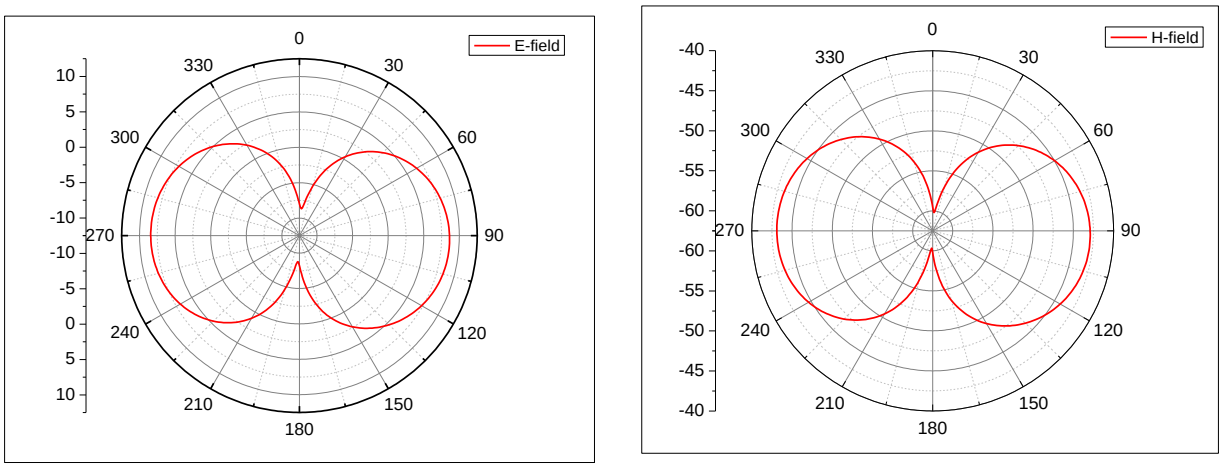

(c)

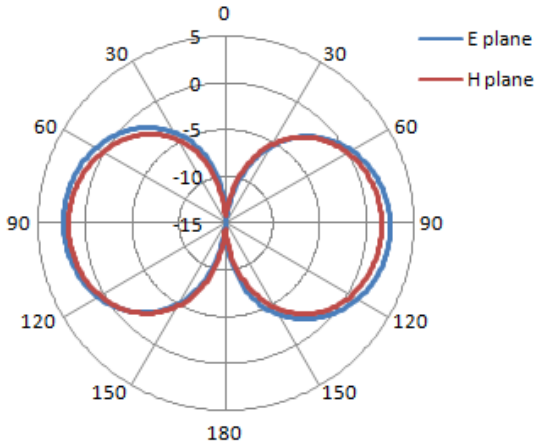

(d)

Fig. 5.2.4 (b) 3D radiation pattern at 7.8 THz. **(c)** Co- and cross-polarized patterns at 7.8 THz. (d) Far-field E-plane and H-plane plots.

Table 5.2.2. Comparison of graphene patch and dipatch antennas

Comparison of the antenna parameters for the graphene patch and dipatch antenna						
Type	Resonant frequency (THz)	Return loss (dB)	Gain (dB)	Directivity (dBi)	Efficiency (%)	Band-width (GHz)
Patch antenna	8.8	-18.5	0.789	4.542	42	100
Dipatch antenna	7.8	-11	2.239	2.55	93.2	120

5.3 Graphene patch antenna as array

Next, we have studied graphene patch antenna array in series and parallel configurations. Firstly, a patch antenna has been designed with the following characteristics.

Table 5.3.1 Dimensions of graphene patch antenna.

Dimensions of the graphene patch antenna	
Parameters	**Dimensions (μm)**
Patch length (L_p)	38.54
Patch width (W_p)	48.66
Substrate length (L)	80
Substrate width (W)	80
Substrate height (h)	1.5
Nanostrip feed length (l)	20.73
Nanostrip feed width (w)	0.028414

Its return loss characteristics have been shown in Fig. 5.3.1(a). The radiation characteristics like VSWR, radiation patterns have been analyzed next. It can be inferred from the reflection coefficient plots that the antenna resonates at the frequency 6 THz with the return loss of -13.8 dB. The VSWR of the patch antenna has been shown in Fig. 5.3.1(b). Fig. 5.3.2(a-c) depicts the 3D radiation pattern, E-plane and H-plane patterns for the THz operation.

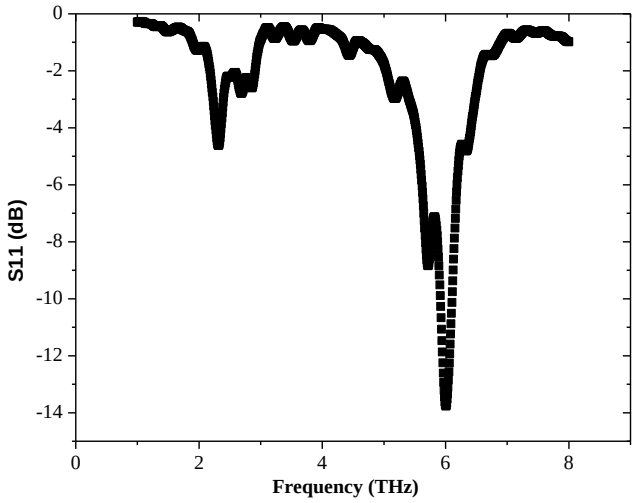

Fig. 5.3.1. (a) Return loss for graphene patch antenna.

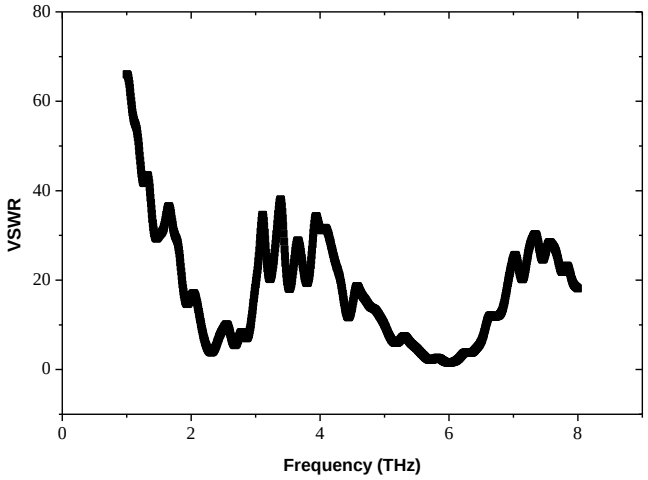

Fig. 5.3.1 (b) VSWR for graphene patch antenna.

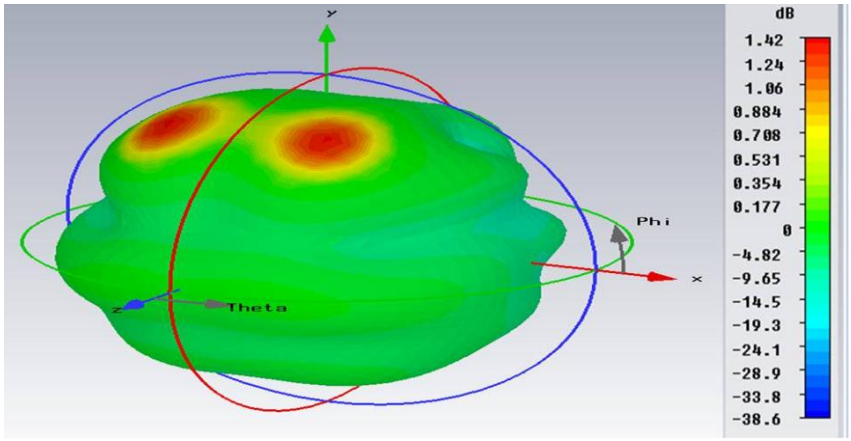

(a)

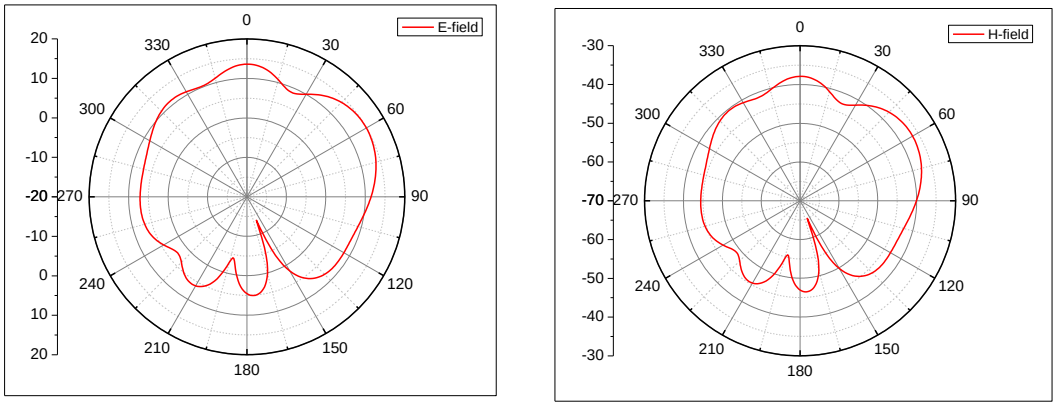

(b)

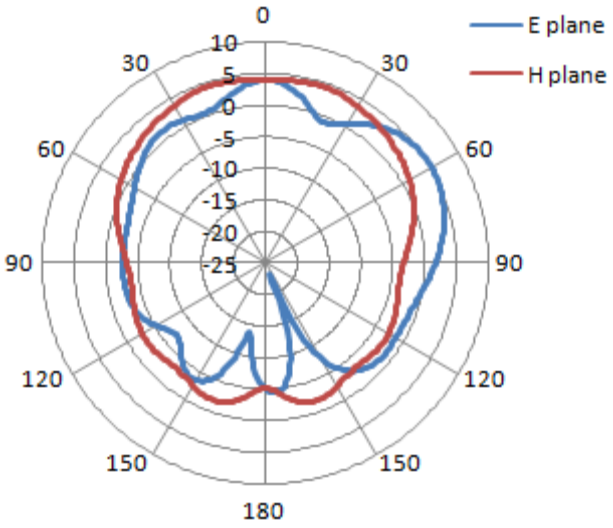

(c)

Fig. 5.3.2 (a) 3D radiation pattern at 6THz. **(b)** Co and cross-polarized pattern at 6 THz. **(c)** Far-field E-plane and H-plane plots.

The graphene patch antenna array can be designed in parallel fashion to obtain better gain and return loss characteristics.

Its return loss characteristics have been shown in Fig. 5.3.4(a). The radiation characteristics like VSWR, radiation patterns have been analyzed next. It can be inferred from the reflection coefficient plots that the antenna resonates at the frequency 7.25 THz with the return loss of -13.8 dB. The VSWR of the patch antenna has been shown in Fig. 5.3.4(b). Fig. 5.3.5(a-c) depicts the 3D radiation pattern, E-plane and H-plane patterns for the THz operation. These curves have been obtained from the directivity plots of the antenna keeping phi=0 and phi=90 degrees.

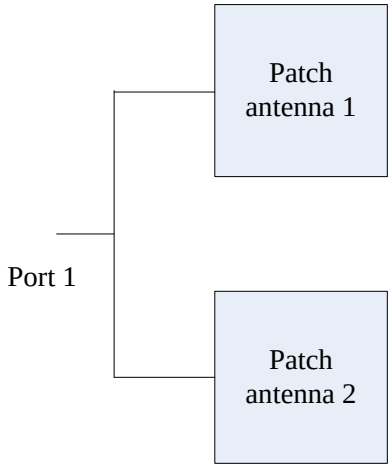

Fig. 5.3.3 Schematic diagram of graphene parallel-patch antenna.

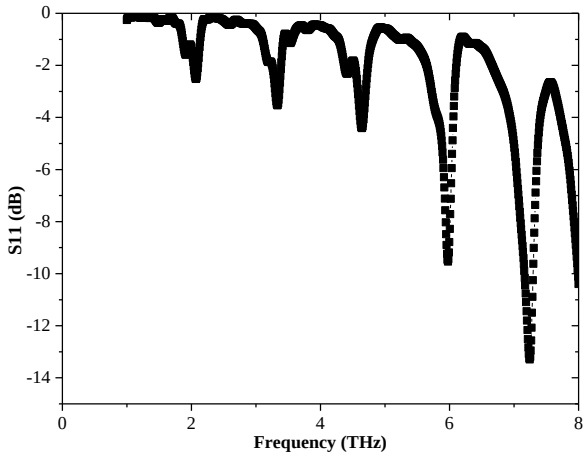

Fig. 5.3.4. (a) Return loss for graphene parallel-patch antenna.

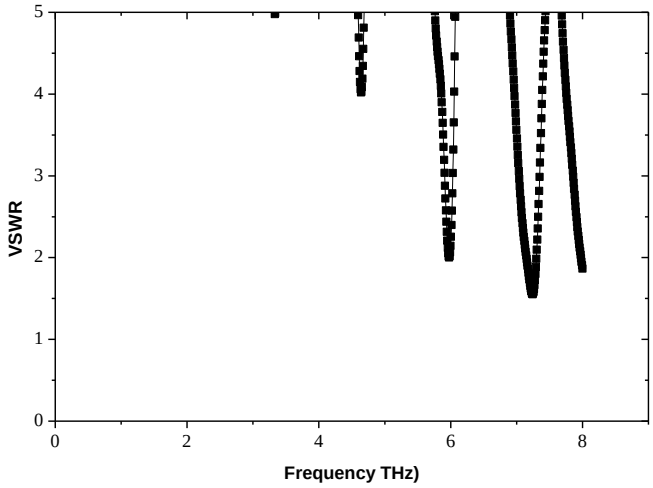

Fig. 5.3.4 (b) VSWR for graphene parallel-patch antenna.

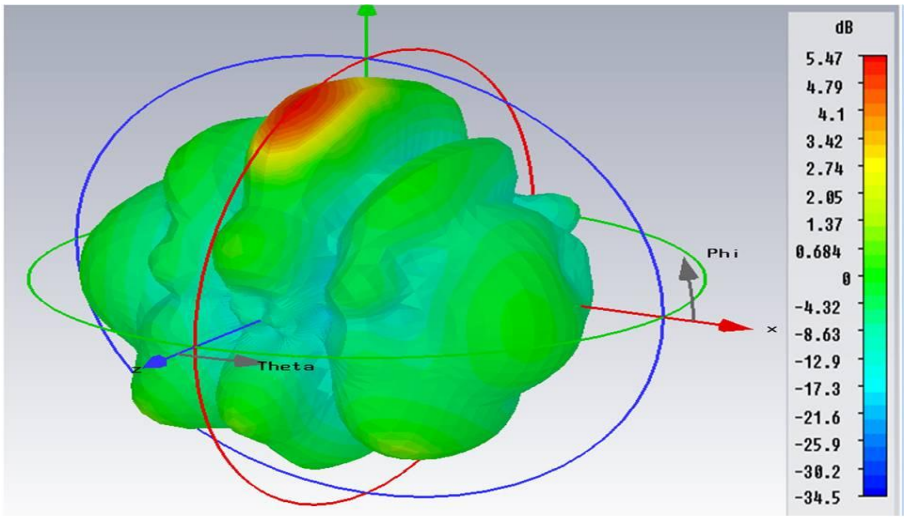

(a)

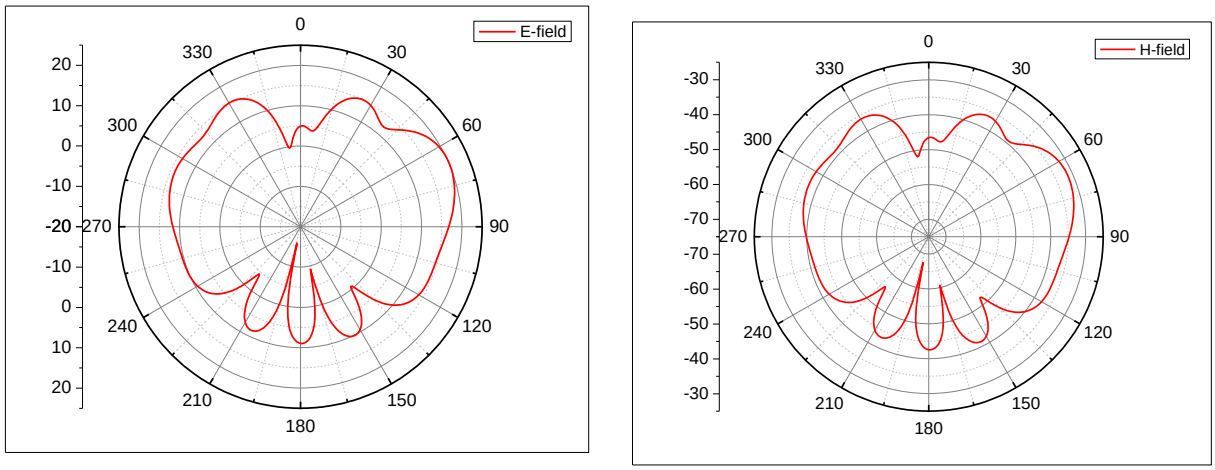

(b)

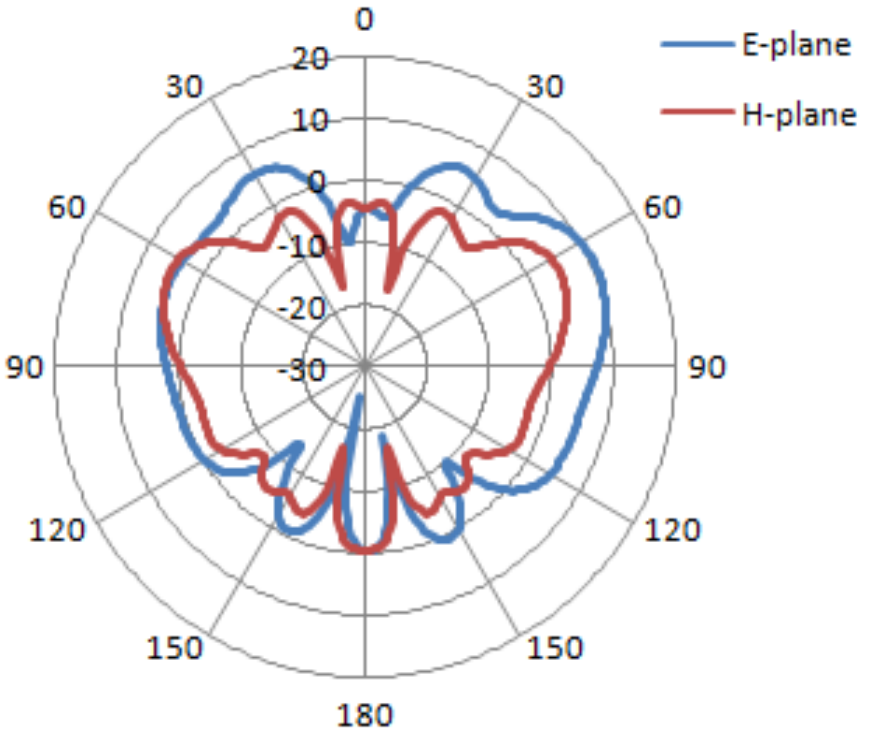

(c)

Fig. 5.3.5 (a) 3D radiation pattern at 7.25 THz. **(b)** Co and cross-polarized pattern at 7.25 THz. (c) Far-field E-plane and H-plane plots

The graphene patch antenna array can be designed in serial fashion to obtain better gain and return loss characteristics.

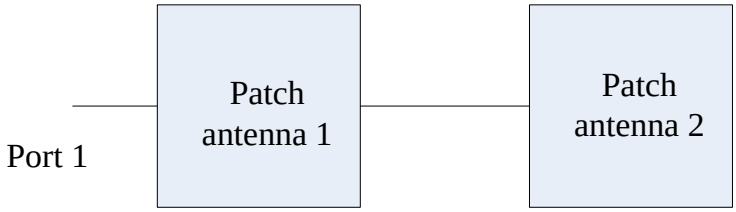

Fig. 5.3.6 Schematic diagram of graphene serial-patch antenna.

Its return loss characteristics have been shown in Fig. 5.3.7(a). The radiation characteristics like VSWR, radiation patterns have been analyzed next. It can be inferred from the reflection coefficient plots that the antenna resonates at the frequency 6 THz with the return loss of -14 dB. The VSWR of the patch antenna has been shown in Fig. 5.3.7(b). Fig. 5.3.8(a-c) depicts the 3D radiation pattern, E-plane and H-plane patterns for the THz operation.

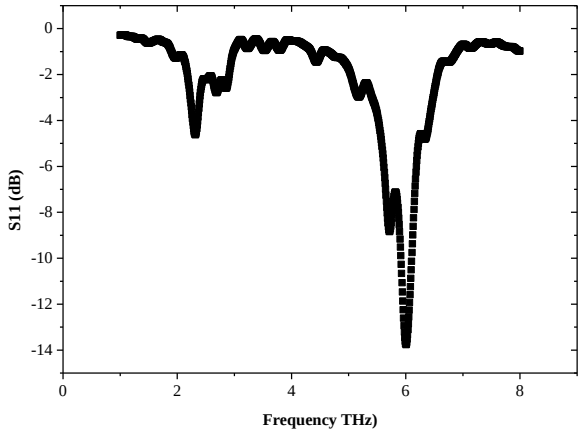

Fig. 5.3.7. (a) Return loss for graphene serial-patch antenna.

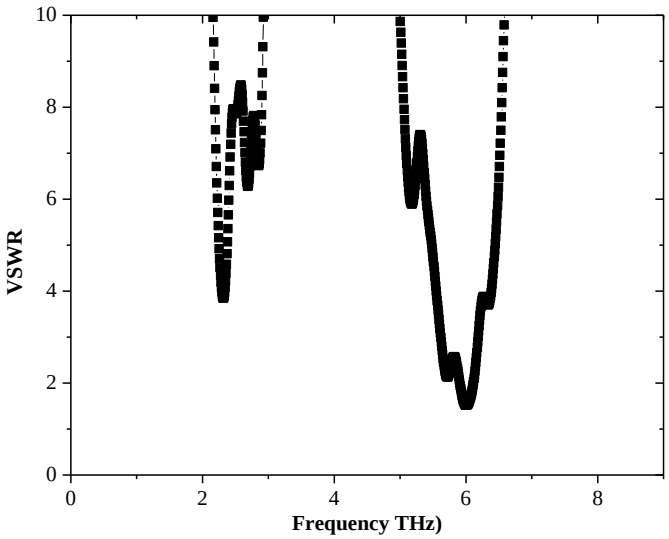

Fig. 5.3.7(b) VSWR for graphene serial-patch antenna.

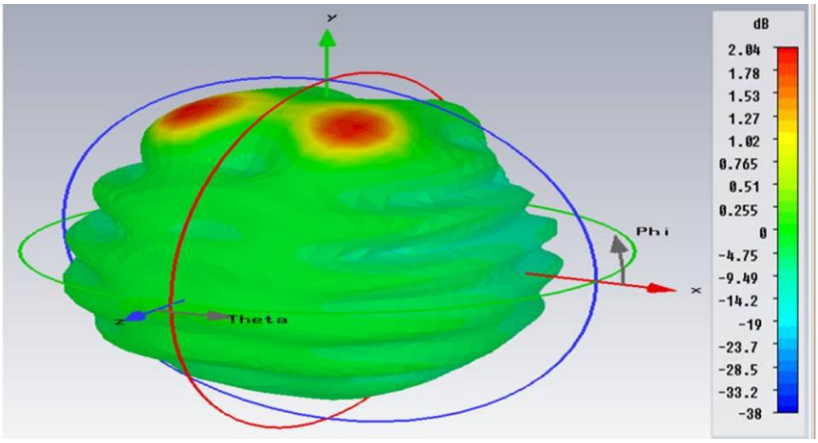

(a)

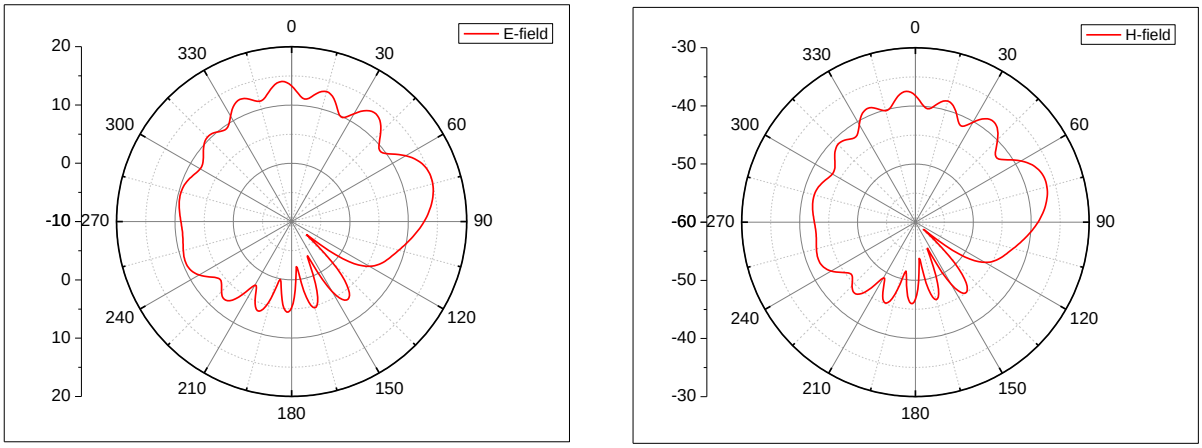

(b)

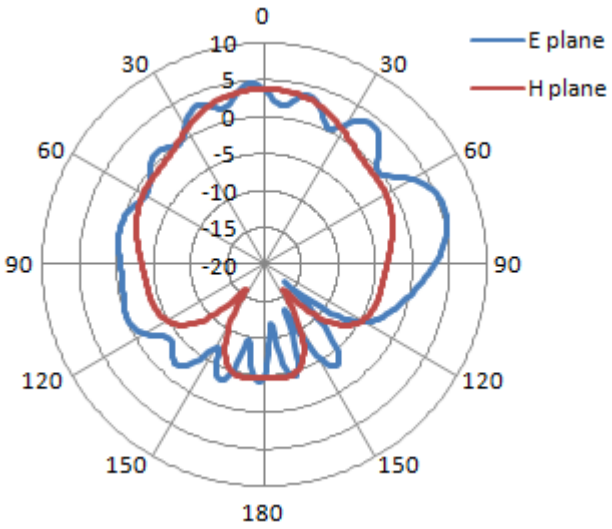

(c)

Fig. 5.3.8 (a) 3D radiation pattern at 6 THz. **(b)** Co- and cross-polarized patterns **(c)** Far-field E-plane and H-plane plots at 6 THz.

Table 5.3.2 Comparison of graphene patch and dipatch antennas

Comparison of the antenna parameters for the graphene patch and dipatch antenna						
Type	Resonant frequency (THz)	Return loss (dB)	Gain (dB)	Directivity (dBi)	Efficiency (%)	Band-width (GHz)
Patch antenna	6	-14	1.415	6.256	32.8	100
Serial-patch antenna	6	-14	2.039	6.982	32	120
Parallel-patch antenna	7.25	-14	5.471	10.62	30	120

5.4 CONCLUSION

In this chapter, a graphene based nanostrip transmission line has been designed and analyzed with the study of characteristics of the transmission line like normalized phase constant, attenuation constant. Based on the nanostrip line, the symmetric and asymmetric power splitters have been designed and simulated. Then, a nano-dipatch antenna has been analyzed. Further, this antenna prototype has been used to design patch antenna arrays for terahertz communications.

REFERENCES

[1] X. Zhu, W. Yan, N. A. Mortensen and S. Xiao, "Bends and splitters in graphene nano-ribbon waveguides," *Opt. Exp.*, vol. 21, no. 3, pp. 3486-3491, Feb. 2013.

[2] K. J. Vinoy, J. K. Abraham, V. K. Varadan, "Fractal dimension and frequency response of fractal shaped antennas," *IEEE 4th International Symposium on Antennas and Propagation*, pp. 222-225, June 2003.

[3] K. J. Vinoy, J. K. Abraham, V. K. Varadan, "On the relationship between fractal dimension and the performance of multi-resonant dipole antennas using Koch curves," *IEEE Trans. Ant. Prop.*, vol. 51, no. 9, pp. 2296-2303, Sept 2003.

[4] K. J. Vinoy, K. A. Jose, V. K. Varadan, V. V. Varadan, "Hilbert curve fractal antenna: A small resonant antenna for VHF/UHF applications," *MOTL*, vol. 29, no. 4, pp. 215-219, May 2001.

[5] T. Holmgaard, Z. Chen, S. I. Bozhevolnyi, L. Markey, A. Dereux, A. V. Krasavin and A. V. Zayats, "Bend and splitting loss of dielectric loaded surface plasmon polariton waveguides," *Opt. Exp.*, vol. 16, no. 18, pp. 13585-13592, Aug. 2008.

[6] N. Joshi and N. P. Pathak, "Graphene-backed graphene plasmonic coplanar waveguide (GB-GPCPW) for terahertz integrated circuit applications," *IEEE Proceedings of AEMC 2015*, no. 103, Dec 2015.

[7] N. Joshi and N. P. Pathak, "Modeling of graphene coplanar waveguide and its discontinuities for THz integrated circuit applications," *Plasmonics*, 1-10, 2016.

[8] Y Yao, Kats MA, Genevet P, Yu N, Song Y, Kong J and Capasso F. (2013) Broad electrical tuning of Graphene Loaded Plasmonic Antennas. Nano Letters 13(3): 1257-1264.

[9] Wang XC, Zhao WS, Hu J and Zhang T. (2013) A Novel Tunable antenna at THz frequencies using Graphene-based Artificial Magnetic Conductor (AMC). Progress in Electromagnetic Research Letters 41: 29-38.

[10] Carrasco E and Carrier JP. (2013) Reflectarray antenna at THz using Graphene. IEEE Antennas and Wireless Propagation Letters 12: 253-256.

[11] Kosuga S, Suga R, Hashimoto O and Koh S. (2017) Graphene-based optically transparent dipole antenna. Applied Physics Letters 110, 233102: 1-3.

[12] Y. Wang, X. R. Hong, T. Sang and G. F. Yang, "Tunable 1x2 plasmonic splitter of dielectric-loaded graphene waveguide based on multimode interference," *Appl. Phys. Exp.*, vol. 9, no. 12, pp. 125102 1-3, Nov. 2016.

[13] P. Qiu, W. Qiu, Z. Lin, H. Chen, Y. Tang, J. Wang, Q. Kan and J. Pan, "Ultra-compact tunable graphene-based plasmonic multimode interference power splitter in mid-infrared frequencies," *China Inf Sci 2017*, vol. 60, no. 8, pp. 082402 1-6, Aug. 2017.

[14] J. N. George and M. G. Madhan, "Analysis of single band and dual band graphene based patch antenna for terahertz region," *Physica E.: Low-Dimensional systems and nanostructures*, vol. 94, pp. 126-131, Oct. 2017.

[15] M. Bozzi, L. Pierantoni and S. Bellucci, "Applications of Graphene at microwave frequencies," *Radioengineering*, vol. 24, no. 3, Sept. 2015.

[16] R. Bala, A. Marwaha and S. Marwaha, "Comparative analysis of zigzag and armchair structures for graphene patch antenna in THz band," *J. Mater. Sci.: Mater. Electron.*, vol. 27, no. 5, pp. 5064-5069, Jan. 2016.

[17] I. Llaster, C. Kremers, A. C. Aparicio, J. M. Jornet, E. Alarcon and D. N. Chigrin, "Graphene-based nano-patch antenna for terahertz radiation," *Photonics and Nanostructures-Fundamentals and Applications*, vol. 10, no. 4, pp. 353-358, Oct. 2012.

[18] J. Jornet and I. F. Akyildiz, "Graphene-based plasmonic nano-antenna for terahertz band communication in nanonetworks," *IEEE J. Sel. Areas Commun.*, vol. 32, no. 12, pp. 685-694, Dec. 2013.

[19] G. Chattopadhyay, "Technology, capabilities, and performance of low power terahertz sources," *IEEE T. Terahz Sci. Techn.*, vol. 1, no. 1, pp. 33-53, Sept. 2011.

[20] G. Chattopadhyay, "Terahertz antennas and related optical components," *2015 International Workshop on Antenna Technology (iWAT)*, pp. 75-76, March 2015.

[21] G. Chattopadhyay, "Terahertz circuits, systems, and imaging instruments," *2014 39th international conference on Infrared, Millimeter, and Terahertz waves (IRMMW-THz)*, Sept. 2014.

[22] J. S. Gómez-Díaz, J. Perruisseau-Carrier, P. Sarma and A. Ionescu, "Non-contact Characterization of Graphene Surface Impedance at Micro and Millimeter Waves", *J. Appl. Phys.*, vol. 111, pp. 114908 1-7, June 2012.

Chapter 6

Conclusions and Future Scope

6.1 Conclusions

We have studied the state-of-the-art in wireless communication links in chapter 1. The wireless communications demand ultra-high bandwidth at high data rates in the order of Tbps. The optical communications allow transmission of high bandwidths, but wireless communication technology is not advanced enough to provide transmitter and receiver integrated circuits in THz regime. The transmission of data rates upto 100 Gbps has been achieved till now. But, in order to achieve higher data rates with ultrafast communication speeds, we require high-speed communication links. Therefore, we move forward to the graphene based terahertz integrated circuits, which provide high data rates with additional features of compactness, tunability and easy-to-synthesize methods. This will accomplish the need of miniaturized transmitter and receivers working at the nanoscale. These graphene based plasmonic structures provide high stability, low cost, less power utilization, better impedance matching and high radiation efficiency with the potential for large-scale integration and lower losses. Firstly, the graphene based waveguides have been studied. Then, various THz integrated circuits have been designed, which provide single-band or multi-band operations sustaining the increased demand of multiple functions using the same system. Multi-band systems can be implemented by parallel, switchable or concurrent configurations. The concurrent multiband front end provides different standard compatibility with a single circuitry only; hence reduce the circuit size and the power consumption. An attempt is made to an extent to implement this concept in photonic integrated circuits. Probably due to the fact that most of the photonic integrated circuits are developed by using optical waveguides. These optical waveguides operate in TE or TM modes and have a limited single mode operational bandwidth. In order to obtain multiband operation, we require large single mode operational bandwidth of the waveguide so that no higher order mode can start propagating in the desired two or more than two frequency bands. This can easily be achieved, if waveguide operates in TEM or Quasi TEM mode. Here, quasi-TEM nature of modes is supported by the graphene based plasmonic waveguides. This waveguide can be modelled with the help of a two-wire transmission line operating in quasi TEM mode. The course of this research work covers the various topics like graphene plasmonic

waveguide based filters, diplexers, couplers and antenna. The graphene based plasmonic resonators have been studied, which provide lower attenuation values (0.3 dB) as compared to metallic resonators (0.43-0.6 dB) [56]. The graphene based nano-patch antenna provide a promising performance with smaller size and excellent radiation characteristics as compared to its metallic counterparts [80]. The various research objectives have been attained except the fabrication part, which is missing from the target set. The organization of the thesis was as follows

Chapter 1 deals with the motivation for carrying out this research work along with detailed literature review for identifying research gaps. On the basis of identified research gaps, the research problem to be solved during the course of PhD dissertation has been defined.

Chapter 2 of this thesis is devoted for the electromagnetic analysis of graphene plasmonic waveguide and its variants. The transmission line characteristics such as characteristic impedance, propagation constant, effective dielectric constant, etc. have been obtained using full wave electromagnetic simulation tool CST microwave studio 2012 version. In all simulations, graphene has been modeled using its surface impedance model with the help of Kubo's formula.

Chapter 3 of this dissertation describes the graphene plasmonic waveguide based resonators such as ring resonator, and modified complementary split ring resonators. Further, dual pass band photonic circuits have been designed using band pass filters. The full wave simulations have been carried out using commercial software tool CST microwave studio.

Chapter 4 of this thesis deals with the design and analysis of filter based diplexer and directional coupler. The diplexer design involves two band-pass filters (BPFs) designed using graphene plasmonic SWR and a broadband chamfered T-junction. This diplexer can simultaneously multiplex two signals at different wavelengths or one can treat it as a multiplexer where signals at different bands can be multiplexed.

Chapter 5 explains the design and analysis of an antenna at terahertz frequencies. The antenna is designed with two graphene plasmonic stepped width resonator (GPSWR) connected with a gap. The simulated return loss and radiation pattern of the antenna is also provided in the chapter.

6.2 Future Scope

Connection between earlier studies and contributions with this research work has verified the potential future of nano-photonics and more and more expansion with their applications in THz frequency range. Even though existence of specific assumptions and restrictions in just about any study will probably limit the outcome of their contribution, it will be useful to extend the work presented in this thesis further. Consequently, much more work can be carried out for the following areas:

- Design of graphene based active devices operating at terahertz frequencies
- Design of graphene based multiband radiating elements using graphene based parallel plate hybrid waveguide.
- Design of series and parallel patch multiband radiating elements.
- Design of graphene based devices in microwave frequency region for industrial scale implementation.

Modeling of Graphene CST microwave studio

- Graphene behaves like a very thin anisotropic dielectric with thickness about 0.35 nm.
- Such small dimensions cause challenges in simulation, adversely affecting the performance.
- The CST introduces two approximate models for graphene first as a thin metal like with a derived surface conductivity of σ_s, secondly graphene has been modeled as a Drude-like material with Re[ε_r] and Im[ε_r], which are shown as Graphene and Graphene_Eps, respectively.
- The surface conductivity, σ_s of a planar graphene sheet in free space is given by:

$$\sigma_s = j\frac{q_e^2(\omega - j\tau^{-1})}{\pi\hbar^2}\left[\frac{1}{\omega - j\tau^{-1}}\int_0^\infty \partial\epsilon\ \epsilon\left(\frac{\partial f(\epsilon)}{\partial\epsilon} - \frac{\partial f(-\epsilon)}{\partial\epsilon}\right) - \int_0^\infty \partial\epsilon\ \frac{f(-\epsilon) - f(\epsilon)}{(\omega - j\tau^{-1})^2 - 4\left(\frac{\epsilon}{\hbar}\right)^2}\right]$$

with Fermi-Dirac distribution: $f(\epsilon) = \left[exp\left(\frac{\epsilon - \mu_c}{T}\right) + 1\right]^{-1}$

assuming low a.c. field intensity, vanishing d.c. magnetic field and $v_f \approx 10^6 \frac{m}{s} \ll \frac{\omega}{k}\sqrt{1 + (\omega\tau)^{-2}}$

where $\tau \approx 10^{-13}\ s$ and v_p the phase velocity of "light" interacting with graphene sheet.

$$\sigma = \sigma^{intra} + \sigma^{inter}$$

- Intraband contribution:

$$\sigma^{intra}(\omega) = \frac{2q_e^2 T}{\pi\hbar^2}\ln\left[2\cosh\left(\frac{\mu_c}{2T}\right)\right]\frac{i}{\omega + i\tau^{-1}}$$

- Interband contribution:

$$\sigma^{inter}(\omega) = \frac{q_e^2}{4\hbar}\left[G(\omega/2) - \frac{4\omega}{i\pi}\int_0^\infty \partial\epsilon\frac{G(\epsilon) - G\left(\omega/2\right)}{\omega^2 - 4\epsilon^2}\right]$$

$$\text{with } G(\epsilon) = \frac{\sinh\left(\frac{\epsilon}{T}\right)}{\cosh\left(\frac{\mu_c}{T}\right)+\cosh\left(\frac{\epsilon}{T}\right)}$$

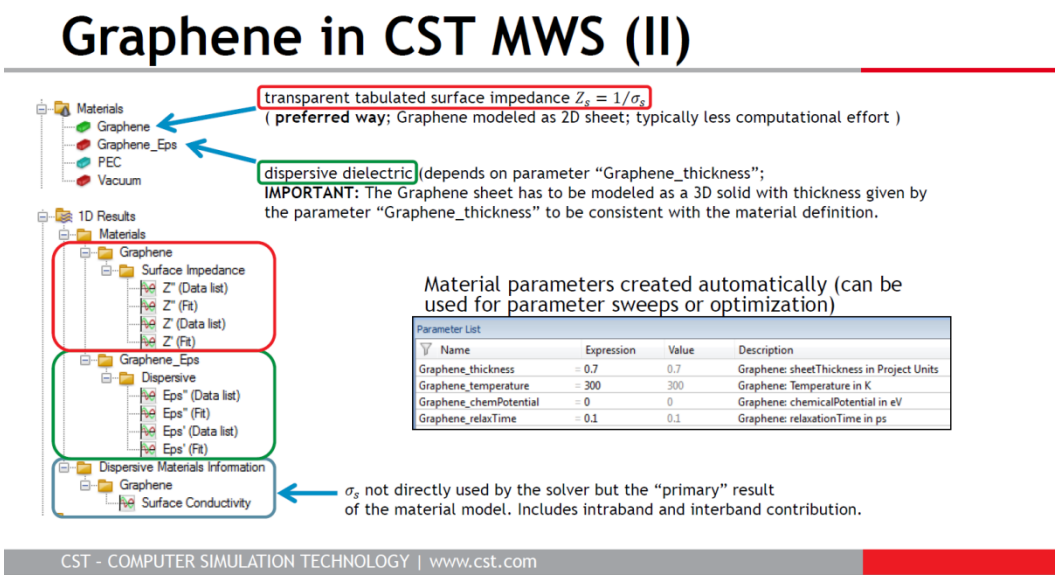

- The macro will generate surface impedance and permittivity values at the specified frequency samples.

Graphene parameters: The synthesis of graphene is aimed to obtain high carrier mobility and low density of defects [1]. The graphene mobility is dependent on substrate. Its mobility and conductivity are listed in table below for various synthesis methods.

Mobility (μ) and minimum conductivity (σ_{min}) of graphene synthesized using various techniques and deposited on different substrates.

Substrate	Production technique	$\mu(x10^3\ cm^2V^{-1}s^{-1})$	$\sigma_{min}(e^2/h)$	Ref.
SiO_2/Si	Exfoliation	10-15	4	[2]
Boron nitride	Exfoliation	25-140	6	[3]
Suspended	Exfoliation	120-200	$1.7/\pi$	[4]
SiC	Thermal-SiC	1-5	--	[5]
SiO_2/Si	Ni-CVD	2-5	--	[6]
SiO_2/Si	Cu-CVD	1-16	--	[7]

REFERENCES:

[1] D. R. Cooper, B.D. Anjou, N. Ghattamaneni et. al., "Experimental Review of Graphene," ISRN Condensed Matter Physics, vol. 2012, pp. 1-56, Nov. 2011.

[2] K. S. Novoselov, A. K. Geim, S. V. Morozov et al., “Electric field in atomically thin carbon films,” Science, vol. 306, no. 5696, pp. 666–669, 2004.

[3] C. R. Dean, A. F. Young, I. Meric et al., “Boron nitride substrates for high-quality graphene electronics,” Nature Nanotechnology, vol. 5, no. 10, pp. 722–726, 2010.

[4] K. I. Bolotin, K. J. Sikes, Z. Jiang et al., “Ultrahigh electron mobility in suspended graphene,” Solid State Communications, vol. 146, no. 9-10, pp. 351–355, 2008.

[5] K. V. Emtsev, A. Bostwick, K. Horn et al., “Towards wafersize graphene layers by atmospheric pressure graphitization of silicon carbide,” Nature Materials, vol. 8, no. 3, pp. 203– 207, 2009.

[6] K. S. Kim, Y. Zhao, H. Jangetal.,“Large-scale pattern growth of graphene films for stretchable transparent electrodes,” Nature, vol. 457, no. 7230, pp. 706–710, 2009.

Appendix II

The data in form of tables 2.3.3.1 to 2.3.3.22 have been presented in appendix for the GCPW structure, which shows the change in values of characteristic impedance, Z_0 with frequency (f) in THz relative to the aspect ratio (AR) at different values of strip width, s for odd and even modes.

Table 2.3.3.1. Change in values of Z_0 with f in THz relative to the AR at s = 1 nm for odd mode.

f(THz) / AR	0.1	0.3	0.5	0.7	0.9	1.2	1.4	1.6	1.8	2
0.1	1255.606	979.618	953.16	933.02	933.02	925.97	925.97	925.97	925.97	922.76
0.2	1054.868	905.58	799.94	791.79	785.17	781.37	781.37	776.76	776.76	775.8656
0.3	860.3714	693.0307	659.37	649.54	639.82	636.74	636.74	633.6	630.35	630.35
0.4	782.9181	645.64	584.88	584.88	584.88	584.88	576.93	575.9245	575.3664	574.2217
0.5	677.2491	528.1255	508.4578	500.88	500.88	499.6828	498.5474	497.5721	496.7991	495.8044
0.6	550.89	490.88	430.87	410.87	410.87	410.87	406.87	406.87	406.27	406.27
0.7	457.89	363.24	346.03	346.03	346.03	346.03	346.03	341.27	341.27	341.27
0.8	335.71	268.97	257.85	252.29	252.29	252.29	252.29	246.73	61759	56267
0.9	244.31	197.06	187.61	187.61	187.61	187.61	39396	35885	33901	32947
1.0	2.317e-05	5.7432e-05	9.5501e-05	0.00013357	0.00016783	0.00022493	0.000263	0.00030253	0.00033976	0.00037748 5

Table 2.3.3.2. Change in values of Z_0 with f in THz relative to the AR at s = 1 nm for even mode.

f(THz) / AR	0.1	0.3	0.5	0.7	0.9	1.2	1.4	1.6	1.8	2
0.1	1778.731	1384.4	1334.8	1305	1305	1305	1302.5	1301.2	1299.9	1298.7
0.2	1340.3	1142.3	1006.9	1006.9	996.45	986.03	986.03	986.03	986.03	986.03
0.3	996.5736	792.13	770.67	748.47	734.41	731.45	729.97	2.0617e+06	1.54425+06	1.1904e+06
0.4	875.3177	712.95	656.75	651.17	645.6	642.0339	1.93E+06	1.22E+06	1.01E+06	7.22E+05
0.5	725.4358	563.2989	541.7748	538.29	534.3488	1.36E+06	8.97E+05	6.42E+05	5.09E+05	3.94E+05
0.6	569.59	505.87	443.27	423.15	1.2178e+06	6.3061e+05	4.1809e+05	3.0808e+05	2.4058e+05	2.0057e+05
0.7	463.14	368.85	354.34	1.134e+06	6.0358e+05	3.0318e+05	2.2104e+05	1.7176e+05	1.389e+05	1.1778e+05
0.8	334.46	263.45	7.9946e+05	3.4391e+05	1.9197e+05	1.0822e+05	84185	70049	248.79	247.73
0.9	247.73	192.77	2.2904e+05	1.0936e+05	68732	46278	180.57	177.95	177.95	175.33
1.0	0.000243	0.000399	0.0006 9383	0.0009 4413	0.0011 944	0.0015 644	0.0018 147	0.0020 541	0.0023 153	0.0025656

Table 2.3.3.3. Change in values of Z_0 with f in THz relative to the AR at s = 4 nm for odd mode.

f(THz) / AR	0.1	0.3	0.5	0.7	0.9	1.2	1.4	1.6	1.8	2
0.1	1824.69	1637.6	1450.9	1368	1361	1354.1	1354.1	1354.1	1354.1	1354.1
0.2	1496.936	1312.6	1139.8	1126	1119.1	1112.1	1105.2	1105.2	1105.2	1105.2
0.3	1284.723	1022.3	980.78	953.12	953.12	953.12	946.21	946.21	946.21	946.21
0.4	1189.2	1113.2	1023.3	940.31	885	885	885	878.08	878.08	878.08
0.5	1079.831	1022.3	966.95	911.64	856.32	801.01	801.01	801.01	801.01	801.01
0.6	878.8739	773.36	662.73	655.82	655.82	648.9	648.9	648.9	648.9	648.9
0.7	797.4937	635.08	621.25	600.51	593.59	593.59	593.59	586.68	586.68	586.68
0.8	687.8206	542.9247	521.182	510.62	510.62	510.62	510.62	510.62	510.62	503.71
0.9	476.05	372.34	358.51	358.51	351.6	351.6	351.6	351.6	344.69	344.69
1.0	2.39E-05	5.31E-05	5.9577e-05	9.6037e-05	0.0001325	0.00017	0.00022417	0.00029917	0.00033667	0.000383

Table 2.3.3.4. Change in values of Z_0 with f in THz relative to the AR at s = 4 nm for even mode.

f(THz) / AR	0.1	0.3	0.5	0.7	0.9	1.2	1.4	1.6	1.8	2
0.1	2577.344	2300.2	2033.4	1912.1	1904	1889.167	1889.167	1889.167	1889.167	1884.006
0.2	1994.929	1750.3	1491.297	1483.4	1475.4	1467.3	1459.2	1459.2	1459.2	1459.2
0.3	1578.864	1217.713	1192.3	1160	1160	1160	1151.9	1151.9	1151.9	1151.9
0.4	1399.4	1309.6	1204.8	1107.6	1040.2	1040.2	1032.7	1032.7	1032.7	1032.7
0.5	1211.033	1143.8	1079.1	1014.4	957.78	884.99	884.99	884.99	884.99	884.99
0.6	908.5882	796.04	674.73	674.73	666.64	666.64	666.64	2.1204e+06	1.5698e+06	1.2185e+06
0.7	801.6053	632.53	616.99	601.46	585.92	585.92	1.8416e+06	1.3493e+06	9.8929e+05	7.7722e+05
0.8	668.8501	521.15	499.43	493.5	491.53	1.3929e+06	9.4905e+05	6.8054e+05	5.1633e+05	6.7794e+05
0.9	437.13	342.3	329.6	329.66	5.9571e+05	3.0138e+05	2.1837e+05	1.6743e+05	1.3724e+05	1.1649e+05
1.0	0.000238	0.000395	0.00067851	0.00091378	0.0011574	0.0015272	0.0017708	0.0020145	0.0022666	0.002568

Table 2.3.3.5. Change in values of Z_0 with *f* in THz relative to the AR at s = 6 nm for odd mode.

f(THz) / AR	0.1	0.3	0.5	0.7	0.9	1.2	1.4	1.6	1.8	2
0.1	2022.132	1805.4	1601.9	1515.2	1510.9	1497.9	1493.6	1493.6	1493.6	1493.6
0.2	1583.083	1419.7	1267.7	1181.1	1176.7	1172.4	1168	1168	1168	1168
0.3	1511.707	1315.5	1142	1129	1124.6	1115.9	1111.6	1111.6	1111.6	1111.6
0.4	1298.431	1189.8	1094.2	989.96	959.55	959.55	955.21	955.21	955.21	955.21
0.5	1211.9	1077.2	942.56	903.47	899.13	894.78	890.44	890.44	890.44	890.44
0.6	1091.076	994.3	911.77	816.21	807.53	807.53	807.53	807.53	807.53	798.84
0.7	885.3526	725	672.88	668.53	659.84	651.16	651.16	651.16	646.81	646.81
0.8	802.6023	629.44	599.03	594.69	594.69	590.35	590.35	590.35	586	586
0.9	691.4569	538.22	516.51	512.16	507.82	507.82	507.82	507.82	503.48	503.48
1.0	2.37E-05	5.5242e-05	9.5501e-05	0.00013	0.00016	0.000222	0.0002623	0.00029681	0.00033707	0.00037158

Table 2.3.3.6. Change in values of Z_0 with f in THz relative to the AR at s = 6 nm for even mode.

f(THz) / AR	0.1	0.3	0.5	0.7	0.9	1.2	1.4	1.6	1.8	2
0.1	2668.987	2369.2	2080.7	1982.4	1969.3	1956.2	1949.6	1949.6	1949.6	1949.6
0.2	2002.84	1792.3	1589	1484.1	1477.6	1471	1464.5	1464.5	1464.5	1464.5
0.3	1874.589	1641.5	1405.5	1385.8	1379.2	1372.7	1372.7	1372.7	1372.7	1372.7
0.4	1489.126	1366.1	1248.1	1130.1	1090.8	1090.8	1090.8	1084.2	1084.2	1084.2
0.5	1352.9	1196.8	1040.7	988.64	978.23	978.23	978.23	978.23	978.23	978.23
0.6	1149.855	1051.5	953.11	854.78	841.66	841.66	841.66	841.66	841.66	841.66
0.7	866.4193	710.54	658.1	651.54	644.99	638.43	631.87	2.102e+06	1.59e+06	1.2071e+06
0.8	765.8793	601.01	572.06	565.63	565.63	562.41	1.8234e+06	1.3017e+06	9.7845e+05	7.64e+05
0.9	640.77	501.12	478.51	473.99	473.99	1.3637e+06	9.3102e+05	6.659e+05	5.1125e+05	4.052e+05
1.0	0.000235	0.00039965	0.00062753	0.00087987	0.0010691	0.0014476	0.0017	0.0019523	0.0022046	0.002457

Table 2.3.3.7. Change in values of Z_0 with *f* in THz relative to the AR at s = 8 nm for odd mode.

f(THz) / AR	0.1	0.3	0.5	0.7	0.9	1.2	1.4	1.6	1.8	2
0.1	2186.79	1950.2	1703.3	1642.7	1638.4	1625.4	1621	1621	1621	1621
0.2	1850.419	1655.7	1460.8	1387.2	1382.9	1374.2	1369.9	1369.9	1365.5	1365.5
0.3	1523.426	1365.5	1227	1136	1131.7	1127.4	1123	1123	1123	1123
0.4	1429	1281.4	1142.4	1068.5	1064.2	1059.8	1055.5	1055.5	1055.5	1055.5
0.5	1309.808	1201.2	1097	1001.7	971.34	971.34	967	967	967	967
0.6	1216.2	1003.4	959.94	920.84	907.81	903.47	899.12	899.12	899.12	899.12
0.7	1099.204	1040.5	984.37	923.56	867.09	810.63	810.63	810.63	810.63	810.63
0.8	890.5223	780.22	667.29	662.95	662.95	658.6	658.6	658.6	654.26	6
0.9	694.1045	554.36	532.64	519.61	515.26	515.26	510.92	510.92	510.92	510.92
1.0	2.36E-05	5.38E-05	9.6256e-05	0.00013104	0.00016954	0.00022171	0.00025773	0.000295	0.00033102	0.00036828

Table 2.3.3.8. Change in values of Z_0 with f in THz relative to the AR at s = 8 nm for even mode.

f(THz) / AR	0.1	0.3	0.5	0.7	0.9	1.2	1.4	1.6	1.8	2
0.1	2689.7	2371.5	2067.8	1988.3	1981.1	1966.6	1966.6	1966.6	1966.6	1966.6
0.2	2292	2038.9	1800.3	1699.1	1691.8	1677.4	1677.4	1677.4	1677.4	1677.4
0.3	1771.4	1597.8	1417	1308.6	1308.6	1301.3	1294.1	1294.1	1294.1	1294.1
0.4	1619.5	1454	1288.4	1202	1194.8	1187.6	1184	1184	1184	1184
0.5	1416.667	1583.4	1417	1308.6	1308.6	1301.3	1294.1	1294.1	1294.1	1294.1
0.6	1277.6	1040.1	989.7	946.52	939.32	935.72	932.12	932.12	932.12	932.12
0.7	1098.9	1033.8	975.95	918.1	853.03	802.41	802.41	802.41	802.41	802.41
0.8	838.56	722.87	614.4	614.4	607.17	607.17	607.17	2.0733e+06	1.5435e+06	1.1914e+06
0.9	620.46	491.09	468.91	457.82	457.82	1.3392e+06	9.0762e+05	6.5553e+05	4.992e+05	3.9758e+05
1.0	0.00023021	0.00041098	0.00065202	0.00088757	0.0011341	0.0014792	0.0017202	0.0019667	0.002201	0.0024366

Table 2.3.3.9. Change in values of Z_0 with *f* in THz relative to the AR at s = 10 nm for odd mode.

f(THz) / AR	0.1	0.3	0.5	0.7	0.9	1.2	1.4	1.6	1.8	2
0.1	2337.7	2072.8	1820.8	1764.4	1755.7	1742.6	1738.3	1738.3	1734	1734
0.2	1859.9	1660.1	1469	1395.2	1390.8	1382.1	1377.8	1377.8	1373.4	1373.4
0.3	1608	1442.9	1286.6	1204	1199.7	1191	1186.7	1186.7	1186.7	1186.7
0.4	1438.6	1290.9	1138.9	1082.4	1078.1	1069.4	1065	1065	1065	1065
0.5	1312.6	1208.4	1095.4	988.6	979.91	975.57	975.57	975.57	975.57	975.57
0.6	1233.6	1003.4	933.88	920.85	912.16	907.81	903.47	903.47	903.47	903.47
0.7	1099.8	1043.3	988.6	923.44	866.98	819.2	819.2	814.85	814.85	814.85
0.8	895.64	719.3	680.2	667.17	662.83	662.83	662.83	658.48	658.48	658.48
0.9	697.58	545.55	523.83	519.49	515.15	515.15	515.15	510.8	510.8	510.8
1.0	3.8268e-05	5.0505e-05	7.4979e-05	0.00012393	0.00016064	0.00020958	0.00024629	0.00028301	0.00031972	0.00035643

Table 2.3.3.10. Change in values of Z_0 with *f* in THz relative to the AR at s = 10 nm for even mode.

f(THz) / AR	0.1	0.3	0.5	0.7	0.9	1.2	1.4	1.6	1.8	2
0.1	2695.4	2376.3	2064.5	2001	1994.7	1976	1976	1976	1976	1976
0.2	2189.6	1944.7	1713.2	1619.4	1613.1	1606.8	1600.6	1600.6	1600.6	1600.6
0.3	1694.4	1519.3	1350.4	1250.3	1250.3	1244	1237.7	1237.7	1237.7	1237.7
0.4	1545.2	1381.6	1219	1150.2	1143.9	1137.6	1137.6	1137.6	1137.6	1137.6
0.5	1363.8	1244.9	1125.1	1012.5	1000	993.76	993.76	993.76	993.76	993.76
0.6	1223.5	989.92	923.18	906.5	895.37	895.37	895.37	895.37	895.37	895.37
0.7	1056.3	993.76	937.46	874.9	818.59	774.8	774.8	774.8	774.8	774.8
0.8	812.34	637.17	605.89	593.38	593.38	587.12	587.12	587.12	1.5139e+06	1.1735e+06
0.9	594.64	466.72	446.42	442.35	440.32	3.7801e+05	8.9355e+05	6.4096e+05	4.8774e+05	3.8629e+05
1.0	0.00021673	0.000414	0.00064416	0.00088254	0.0011127	0.0014579	0.0016963	0.0019347	0.0021731	0.0024032

Table 2.3.3.11. Change in values of Z_0 with *f* in THz relative to the AR at s = 20 nm for odd mode.

f(THz) / AR	0.1	0.3	0.5	0.7	0.9	1.2	1.4	1.6	1.8	2
0.1	3877.2	3173.3	2954	2925.2	2890.6	2867.5	2861.7	2855.9	2850.2	2844.4
0.2	3165.9	2648.3	2403.9	2384.7	2360.7	2336.8	2336.8	2332	2327.2	2327.2
0.3	2696.2	2270.4	2040.3	2025.9	2011.5	1992.4	1982.8	1982.8	1978	1978
0.4	2539.4	2193.3	1910.5	1899	1881.7	1864.4	1864.4	1864.4	1858.6	1858.6
0.5	2332	2107.4	1891.7	1733.6	1728.8	1724	1719.2	1714.4	1709.6	1709.6
0.6	2093	1652.1	1585	1556.2	1546.6	1541.8	1537	1537	1537	1532.2
0.7	1906.1	1489.1	1436.4	1422	1412.4	1407.6	1402.8	1402.8	1398	1398
0.8	1593.3	1398	1202.8	1182.3	1172	1172	1172	1172	1172	1161.7
0.9	1274.8	1069.3	956.26	956.26	945.98	945.98	935.71	935.71	935.71	935.71
1.0	0.12496	0.33724	0.54408	0.76724	0.97408	1.2843	1.4966	1.7089	1.9266	2.1405

Table 2.3.3.12. Change in values of Z_0 with *f* in THz relative to the AR at s = 20 nm for even mode.

f(THz) / AR	0.1	0.3	0.5	0.7	0.9	1.2	1.4	1.6	1.8	2
0.1	3499.3	2846.9	2651.8	2624.9	2591.3	2571.1	2571.1	2564.4	2564.4	2564.4
0.2	3020.8	2521.2	2280.2	2257.6	2235	2213.7	2213.7	2203	2203	2203
0.3	2565.8	2149.6	1936.2	1925.6	1904.2	1882.9	1882.9	1882.9	1872.2	1872.2
0.4	2382.8	2066.7	1785.1	1771.7	1765	1744.8	1744.8	1744.8	1744.8	1744.8
0.5	2139	1925.6	1712.2	1573.4	1573.4	1562.8	1562.8	1562.8	1562.8	1562.8
0.6	1829.5	1434.7	1381.4	1360	1349.4	1349.4	1349.4	1349.4	1349.4	1.1019e+07
0.7	1622.9	1261.6	1217	1203.6	1194.7	1190.3	1190.3	9.3833e+06	7.1569e+06	5.7292e+06
0.8	1278.8	1118.4	961.08	945.33	939.6	935.31	935.31	3.1291e+06	2.4448e+06	1.9969e+06
0.9	977.43	817.49	729.98	720.92	717.9	1.9481e+06	1.4057e+06	1.095e+06	8.8591e+05	7.7291e+05
1.0	1.5797	3.0671	4.7138	6.4136	8.1666	10.77	12.469	14.169	15.975	17.622

Table 2.3.3.13. Change in values of Z_0 with *f* in THz relative to the AR at s = 30 nm for odd mode.

f(THz) / AR	0.1	0.3	0.5	0.7	0.9	1.2	1.4	1.6	1.8	2
0.1	3292.4	2874.1	2540.6	2522.4	2504.2	2486.1	2480	2480	2473.9	2473.9
0.2	2558.8	2255.7	1958.6	1928.3	1922.2	1904	1898	1898	1898	1898
0.3	2128.4	1891.9	1667.6	1600.9	1594.8	1582.7	1576.6	1576.6	1576.6	1576.6
0.4	1952.5	1740.3	1540.3	1461.5	1455.4	1443.3	1443.3	1443.3	1443.3	1443.3
0.5	1818.2	1629.7	1447.3	1374.3	1368.2	1356.1	1356.1	1356.1	1356.1	1356.1
0.6	1685.8	1497.8	1334.1	1255.3	1255.3	1249.3	1243.2	1243.2	1243.2	1243.2
0.7	1497.8	1334.1	1167.2	1130.9	1124.8	1118.7	1118.7	1118.7	1118.7	1118.7
0.8	1376.6	1291.7	1212.9	1143	1064.2	1021.7	1021.7	1015.7	1015.7	1015.7
0.9	1128	991.42	864.11	864.11	858.04	845.92	845.92	845.92	845.92	845.92
1.0	2.2414e-05	5.4214e-05	8.8905e-05	0.00012215	0.00015684	0.00020888	0.00024357	0.00027681	0.00031151	0.00034764

Table 2.3.3.14. Change in values of Z_0 with *f* in THz relative to the AR at s = 30 nm for even mode.

f(THz) / AR	0.1	0.3	0.5	0.7	0.9	1.2	1.4	1.6	1.8	2
0.1	2468.3	2106.9	1845.2	1832.7	1826.5	1807.8	1801.6	1801.6	1801.6	1801.6
0.2	2050.8	1782.9	1524.7	1518.4	1506	1499.8	1493.5	1493.5	1493.5	1493.5
0.3	1733	1537.1	1350.2	1294.1	1287.9	1281.7	1275.4	1275.4	1275.4	1275.4
0.4	1580.8	1406.3	1231.8	1175.7	1169.5	1163.3	1163.3	1163.3	1163.3	1163.3
0.5	1473	1314.2	1163.5	1093.8	1089.3	1082.5	1080.3	1080.3	1080.3	1080.3
0.6	1319.5	1182	1038.3	975.76	975.76	969.51	969.51	969.51	969.51	969.51
0.7	1138.3	1007	875.76	850.76	844.51	838.26	838.26	838.26	838.26	838.26
0.8	1013.3	950.76	894.51	832.01	775.76	744.51	744.51	744.51	744.51	744.51
0.9	807.01	694.51	600.76	600.76	594.51	588.26	588.26	588.26	588.26	588.26
1.0	0.000 19612	0.000 35372	0.000 55881	0.000 76836	0.000 96984	0.001 268	0.001 4695	0.0016 791	0.0018 806	0.0020 821

Table 2.3.3.15. Change in values of Z_0 with *f* in THz relative to the AR at s = 40 nm for odd mode.

f(THz) / AR	0.1	0.3	0.5	0.7	0.9	1.2	1.4	1.6	1.8	2
0.1	4673.7	3987.4	3674.7	3648.6	3622.6	3596.5	3596.5	3587.8	3579.1	3579.1
0.2	3500.9	3040.5	2701.7	2693	2675.7	2658.3	2649.6	2649.6	1.6088	1.6088
0.3	2318.8	2062.5	1758.5	1754.1	1745.4	1732.4	1728.1	1728.1	1728.1	1728.1
0.4	2175.5	1936.6	1702	1632.5	1628.2	1615.1	1610.8	1610.8	1610.8	1610.8
0.5	1975.7	1767.2	1567.4	1493.5	1484.8	1476.1	1471.8	1471.8	1467.5	1467.5
0.6	1859.1	1659.3	1476.8	1390	1381.3	1372.6	1372.6	1372.6	1372.6	1372.6
0.7	1623.8	1467.5	1311.1	1224.2	1219.9	1211.2	1206.8	1206.8	1206.8	1206.8
0.8	1393.6	1302.4	1219.9	1128.7	1046.1	1033.1	1033.1	1028.7	1028.7	1028.7
0.9	1150.4	907.13	881.07	863.69	859.35	855.01	855.01	855.01	855.01	855.01
1.0	2.0348e-05	5.2485e-05	8.5342e-05	0.0001196	0.0001535	0.0002039	0.0002705	0.00030145	0.00030307	0.00033557

Table 2.3.3.16. Change in values of Z_0 with f in THz relative to the AR at s = 40 nm for even mode.

f(THz) / AR	0.1	0.3	0.5	0.7	0.9	1.2	1.4	1.6	1.8	2
0.1	2940.6	2445.4	2222.6	2206.1	2189.6	2164.8	2164.8	2156.6	2156.6	2156.6
0.2	2313.4	1991.5	1752.2	1744	1735.7	1719.2	1710.9	1710.9	1710.9	1710.9
0.3	1674	1476.7	1289.6	1249.2	1244.1	1234	1228.9	1228.9	1228.9	1228.9
0.4	1572.8	1390.8	1213.7	1168.2	1163.2	1153.1	1153.1	1153.1	1153.1	1153.1
0.5	1426.2	1269.4	1117.7	1057	1051.9	1046.9	1046.9	1046.9	1046.9	1046.9
0.6	1331.3	1182.8	1042.5	984.69	984.69	976.44	976.44	976.44	976.44	976.44
0.7	1127.8	1006.4	900.2	834.45	834.45	829.4	824.34	824.34	824.34	824.34
0.8	920.43	864.8	799.05	743.42	682.73	677.68	677.68	677.68	677.68	677.68
0.9	743.42	576.53	556.3	546.19	541.13	541.13	541.13	541.13	541.13	541.13
1.0	0.0002091 7	0.0003500 3	0.0005261	0.0007139 1	0.0009134 6	0.0011952	0.001383	0.0015708	0.0017704	0.0019464

Table 2.3.3.17. Change in values of Z_0 with *f* in THz relative to the AR at s = 50 nm for odd mode.

f(THz) / AR	0.1	0.3	0.5	0.7	0.9	1.2	1.4	1.6	1.8	2
0.1	3952.8	3424.6	3084.1	3063.3	3042.4	3014.6	3014.6	3007.7	3000.7	3000.7
0.2	3070.2	2674.1	2347.4	2333.5	2319.6	2305.7	2298.8	2298.8	2298.8	2298.8
0.3	2500.3	2208.4	1923.5	1888.7	1881.8	1867.9	1860.9	1860.9	1860.9	1860.9
0.4	2354.4	2083.3	1833.1	1784.5	1777.6	1763.7	1756.7	1756.7	1756.7	1756.7
0.5	2208.4	1958.2	1722	1659.4	1652.5	1638.6	1638.6	1638.6	1638.6	1638.6
0.6	2006.9	1791.4	1583	1513.5	1506.5	1499.6	1492.6	1492.6	1492.6	1492.6
0.7	1735.9	1555.2	1381.4	1291.9	1291.9	1284.9	1278	1278	1278	1278
0.8	1638.6	1478.7	1325.8	1229.3	1229.3	1222.4	1215.4	1215.4	1215.4	1215.4
0.9	1159.8	993.02	867.93	867.93	860.98	854.03	854.03	854.03	854.03	854.03
1.0	1.9836e-05	4.6502e-05	7.9833e-05	0.0001131 6	0.0001465	0.0001964 9	0.0002298 2	0.00025982	0.00029315	0.00032649

Table 2.3.3.18. Change in values of Z_0 with *f* in THz relative to the AR at s = 50 nm for even mode.

f(THz) / AR	0.1	0.3	0.5	0.7	0.9	1.2	1.4	1.6	1.8	2
0.1	2343.1	1999.9	1776	1761.1	1761.1	1731.2	1731.2	1731.2	1731.2	1731.2
0.2	1910.3	1656.6	1432.7	1432.7	1417.8	1417.8	1402.9	1402.9	1402.9	1402.9
0.3	1626.8	1417.8	1223.8	1194	1194	1194	1194	1194	1194	1194
0.4	1522.3	1358.1	1179	1134.3	1134.3	1134.3	1134.3	1134.3	1134.3	1134.3
0.5	1462.6	1283.5	1104.4	1059.6	1059.6	1059.6	1059.6	1059.6	1059.6	1059.6
0.6	1283.5	1149.2	1014.9	955.16	955.16	955.16	955.16	955.16	955.16	955.16
0.7	1089.5	985.01	850.69	805.92	805.92	805.92	805.92	805.92	805.92	805.92
0.8	1059.6	925.31	820.84	761.15	761.15	761.15	761.15	761.15	761.15	761.15
0.9	671.6	582.05	507.43	507.43	507.43	507.43	507.43	507.43	507.43	507.43
1.0	0.0001787 8	0.0003105 2	0.0004861 7	0.0006778	0.0008494 6	0.0011169	0.0013006	0.0014842	0.0016599	0.0018355

Table 2.3.3.19. Change in values of Z_0 with *f* in THz relative to the AR at s = 60 nm for odd mode.

f(THz) / AR	0.1	0.3	0.5	0.7	0.9	1.2	1.4	1.6	1.8	2
0.4	2377.8	2112.8	1858.2	1801	1795.8	1780.2	1775	1775	1775	1775
0.5	2221.9	1977.7	1743.8	1676.3	1671.1	1660.7	1655.5	1655.5	1655.5	1655.5
0.6	2029.6	1624.3	1541.2	1536	1525.6	1515.2	1510	1510	1510	1510
0.7	1738.6	1567.1	1395.7	1312.5	1307.3	1302.1	1296.9	1296.9	1296.9	1296.9
0.8	1556.7	1380.1	1208.6	1177.4	1167	1161.8	1156.6	1156.6	1156.6	1156.6
0.9	1167	948.75	881.19	875.99	870.8	870.8	865.6	865.6	865.6	865.6
1.0	1.9417e-05	4.9551e-05	8.1457e-05	0.0001127	0.0001452	0.0001919	0.0002238	0.0002553	0.0002872	0.0003197

Table 2.3.3.20. Change in values of Z_0 with *f* in THz relative to the AR at s = 60 nm for even mode.

f(THz) / AR	0.1	0.3	0.5	0.7	0.9	1.2	1.4	1.6	1.8	2
0.4	1434.8	1263.9	1101	1073.1	1069.2	1061.2	1057.2	1057.2	1057.2	1057.2
0.5	1343.4	1192.4	1041.3	1001.6	997.63	989.68	989.68	989.68	989.68	989.68
0.6	1228.2	969.81	918.14	914.16	910.19	902.24	898.26	898.26	898.26	898.26
0.7	1045.3	930.06	818.77	767.1	763.13	759.15	759.15	759.15	759.15	759.15
0.8	902.24	794.92	687.61	675.68	671.71	667.74	663.76	663.76	663.76	663.76
0.9	663.76	524.65	484.9	480.93	476.95	476.95	476.95	476.95	476.95	476.95
1.0	0.0001621 1	0.0002963 9	0.0004664 7	0.0006365 6	0.0007976 9	0.0010483	0.0012214	0.0013385	0.0015586	0.0017273

Table 2.3.3.21. Change in values of Z_0 with *f* in THz relative to the AR at s = 70 nm for odd mode.

f(THz) / AR	0.1	0.3	0.5	0.7	0.9	1.2	1.4	1.6	1.8	2
0.1	4742.1	4049.2	3737.5	3711.5	3676.8	3650.8	3650.8	3642.2	3633.5	3633.5
0.2	3616.2	3113.9	2767.4	2750.1	2732.8	2715.5	2706.8	2706.8	2698.1	2698.1
0.3	2888.7	2524.9	2213.1	2204.5	2195.8	2187.1	2178.5	2178.5	2169.8	2169.8
0.4	2542.2	2247.8	1961.9	1936	1918.6	1910	1901.3	1901.3	1901.3	1901.3
0.5	2230.4	1996.6	1754.1	1702.1	1693.5	1676.1	1676.1	1676.1	1676.1	1676.1
0.6	2039.9	1823.4	1613.2	1543.9	1535.3	1526.6	1526.6	1526.6	1526.6	1526.6
0.7	1902.5	1711.4	1528.9	1442.1	1442.1	1433.4	1424.7	1424.7	1424.7	1424.7
0.8	1682.5	1492	1344.7	1258.1	1258.1	1249.5	1249.5	1249.5	1249.5	1249.5
0.9	1169.2	1099.9	1030.7	952.71	883.42	866.1	866.1	866.1	866.1	866.1
1.0	1.9028e-05	4.9089e-05	8.0239e-05	0.0001109 8	0.0001422	0.0001881 9	0.0002503 8	0.00022002	0.00028221	0.00031286

Table 2.3.3.22. Change in values of Z_0 with f in THz relative to the AR at s = 70 nm for even mode.

f(THz) / AR	0.1	0.3	0.5	0.7	0.9	1.2	1.4	1.6	1.8	2
0.1	2444.2	2040.6	1867.1	1848.2	1829.3	1814.2	1814.2	1810.5	1806.7	1806.7
0.2	1923.6	1646.6	1446.7	1439.2	1427.9	1416.6	1412.8	1412.8	1412.8	1412.8
0.3	1597.6	1397.7	1205.3	1201.6	1194	1182.7	1178.9	1178.9	1178.9	1178.9
0.4	1431.6	1254.4	1084.6	1065.8	1062	1054.4	1050.7	1050.7	1050.7	1050.7
0.5	1277	1126.1	979	948.83	945.06	937.51	933.74	933.74	933.74	933.74
0.6	1160.2	1033.1	900.61	861.95	861.95	856.43	850.9	850.9	850.9	850.9
0.7	1072.3	959.28	849.85	802.44	798.79	795.14	791.49	791.49	791.49	791.49
0.8	922.7	828.81	734.93	685.23	685.23	685.23	679.7	679.7	679.7	679.7
0.9	629.3	568.81	538.57	498.24	457.92	457.92	457.92	457.92	457.92	457.92
1.0	0.0001540 9	0.0002759 1	0.0004383 3	0.0005978 6	0.0007602 8	0.0009865 2	0.0011477	0.0013044	0.0014639	0.0016234